TARGETING AMINOPHOSPHOLIPIDS EXPOSED ON TUMOR ENDOTHELIUM FOR TUMOR IMAGING

APPROVED BY SUPERVISORY COMMITTEE

_____
Phillip E. Thorpe, Ph.D.

_____
Kathlynn C. Brown, Ph.D.

_____
Rolf A. Brekken, Ph.D.

_____
Chaitanya S. Nirodi, Ph.D.

TARGETING AMINOPHOSPHOLIPIDS EXPOSED ON TUMOR ENDOTHELIUM FOR TUMOR IMAGING

by

JASON HUGH STAFFORD

DISSERTATION

Presented to the Faculty of the Graduate School of Biomedical Sciences
The University of Texas Southwestern Medical Center at Dallas
In Partial Fulfillment of the Requirements
For the Degree of

DOCTOR OF PHILISOPHY

The University of Texas Southwestern Medical Center at Dallas
Dallas, Texas
October, 2011

TARGETING AMINOPHOSPHOLIPIDS EXPOSED ON TUMOR ENDOTHELIUM FOR TUMOR IMAGING

Jason Hugh Stafford, Ph.D.

The University of Texas Southwestern Medical Center at Dallas, 2011

Mentor: Philip E. Thorpe, Ph.D.

ABSTRACT

Advances in noninvasive imaging of human cancer are crucial to improving diagnosis and therapeutic planning. My project was aimed at developing novel imaging agents that target the aminophospholipids phosphatidylserine (PS) and phosphatidylethanolamine (PE). PS and PE are normally intracellular, but become exposed on the surface of tumor endothelial cells (EC). Anti-tumor therapies promote exposure of PS and PE on tumor EC and the tumor cells as well. Therefore, I tested the hypothesis that 1N11, a PS-binding antibody, and duramycin, a PE-binding peptide, could function as tumor imaging agents.

I labeled the F(ab')$_2$ fragment of 1N11 with the near-infrared fluophore 800CW for optical imaging and the positron emitting isotope iodine-124 (^{124}I) for PET imaging. 800CW-1N11 F(ab')$_2$ clearly imaged subcutaneous and orthotopic U87 gliomas growing in mice with optimal tumor contrast obtained at 24 h post-

injection (p.i.). Uptake of 800CW-1N11 F(ab')$_2$ was approximately 2-fold higher in irradiated U87 tumors. ^{124}I-1N11 F(ab')$_2$ clearly imaged subcutaneous and orthotopic PC3 prostate carcinomas growing in mice with optimal tumor contrast obtained at 48 hr p.i. Importantly, 800CW- and ^{124}I-1N11 F(ab')$_2$ exhibited low uptake in non-target organs (i.e. liver and kidneys).

Unlike PS, PE had not been established as a specific marker of tumor vasculature in the literature. To demonstrate PE was such a marker, I biotinylated duramycin, characterized its binding properties, and used it to determine the distribution of PE on EC *in vitro* and *in vivo*. Exposure of cultured EC to hypoxia, acidity, reactive oxygen species, or irradiation resulted in the formation of membrane blebs that were intensely PE-positive. When biotinylated duramycin was intravenously injected into tumor-bearing mice it preferentially localized to the luminal surface of the vascular endothelium in multiple tumor models. PE-positive vessels were observed in and around hypoxic regions of the tumor. With the exception of intertubular vessels of the kidney, normal vessels remained unstained. I also conjugated duramycin to 800CW and used it for optical imaging of RM-9 and TRAMP prostate carcinomas. These results demonstrate that both 1N11 and duramycin can be used to image a variety of tumors and warrant further study as imaging agents.

TABLE OF CONTENTS

PAGE

PRIOR PUBLICATONS

The following publications contain work that is presented herein.

1. Stafford, J.H., and Thorpe, P.E. (2011). Increased exposure of phosphatidylethanolamine on the surface of tumor vascular endothelium. *Neoplasia* 13, 299-308.

2. Zhao, D., Stafford, J.H., Zhou H., and Thorpe, P.E. Near-infrared optical imaging of exposed phosphatidylserine in a mouse glioma model. *Translational Oncology* (in press).

LIST OF FIGURES AND TABLES

FIGURES PAGE

TABLES

LIST OF ABBREVIATIONS

1N11, PS-targeting human monoclonal IgG

1N11-LB, biotinylated 1N11

2aG4, PS-targeting mouse monoclonal IgG2A

3G4, PS-targeting mouse monoclonal IgG3

^{3}H, tritium

5-FU, 5-fluorouracil

9D2, PS-targeting rat monoclonal IgM

^{18}F, fluorine-18

^{64}Cu, copper-64

^{68}Ga, gallium-68

^{74}As, arsenic-74

^{99m}Tc, technetium-99m

^{111}In, indium-111

^{124}I, iodine-124

800CW, near-infrared fluophore (Li-COR)

ABAE, adult bovine aortic endothelial cells

ABC, ATP-binding cassette

ADCC, antibody-dependent-cell-mediated cytotoxicity

ADT, androgen deprivation therapy

APS, antiphospholipid syndrome

APLT, aminophospholipid translocase

aSMase, acid sphingomyelinase

ATP, adenosine triposphate

β2GP1, beta-2-glycoprotein 1

bEnd3, murine brain-derived endothelial cells

BLI, bioluminescence imaging

BPH, benign prostatic hyperplasia

BTAP, 4,5-bis(thioacetamido)pentanoyl

Ca^{2+}, calcium

C2, PS-binding domain of lactadherin

C2A, PS-binding domain of synaptotagmin

CB-TE2A, 4,11-bis(carboxymethyl)-1,4,7,10 tetraazabicyclo[6.6.2]hexadecane

CCD, charge-coupled device

CD31, cluster of differentiation 31

CDR, complementary determining region

CEA, carcinoembryonic antigen

CF, cystic fibrosis

CHO, Chinese hamster ovary cells

CPM, counts per minute

CR, complete response

CT, computed tomography

ctrl, (negative) control

D2TB, biotinylated duramycin dimer

DLB, duramycin biotinylated at a single residue

DLB2, duramycin biotinylated at both reactive residues

DOTA, 1,4,7,10 tetraazacyclododecane-1,4,7,10-tetraacetic acid

DUR, duramycin

EC, endothelial cell

EGF, epidermal growth factor

ELISA, enzyme linked immunosorbent assay

ER, endoplasmic reticulum

ESR, electron spin resonance

F98, rat glioma

$F(ab')_2$, immunoglobulin fragment; antigen binding dimer lacking Fc portion

FACBC, fluorocylcobutane-1-carboxylic acid

FACS, fluorescent activated cell sorter

FBS, fetal bovine serum

Fc, fragment cystallizable region

FcRn, neonatal Fc receptor (aka Brambell receptor)

FDG, fluorodeoxyglucose

FDHT, fluoro-5α-dihydrotestosterone

FPLC, fast protein liquid chromatography

FR, folate receptor

Fv, fragment variable region

GBM, glioblastoma multiforme

Gd^{3+}, gadolinium

GFP, green fluorescent protein

Gla, γ-carboxyglutamic acid

GRP, gastrin releasing peptide

GST, glutathione-S-transferase

H_2O_2, hydrogen peroxide

H460, human lung tumor

HER-2, EGF receptor

HYNIC, hydrazinonicotinamide

ICG, indocyanine green

ID, injected dose

IFN-γ, interferon gamma

IgG, immunoglobulin type G

IgM, immunoglobulin type M

IHC, immunohistochemistry

IL-1β, interleukin-1 beta

IL-10, interleukin-10

IL-12, interleukin-12

INF-γ. interferon gamma

i.p., intraperitoneal

i.v., intravenous

kDa, kilodalton

linDUR, linear duramycin (control peptide)

LOR, line of response

$MAG_{3,}$ mercapoacetyltriglycine

MATE, multidrug and toxin extrusion transporter

MBP, maltose binding protein

MDA-MB-435, human melanoma (originally thought to be a breast tumor)

MGDG, monogalactosyl diglyceride

ML-9, butyl-2-methyl-malonic acid

MRI, magnetic resonance imaging

MRP1, multidrug resistance protein 1

NSCLC, non-small cell lung cancer

NADPH, nicotinamide adenine dinucleotide phosphate

NIR, near-infrared

NMR, nuclear magnetic resonance

NOTA, 1,4,7-triazacyclononane-1,4,7-triacetate

OCT, organic cation transporter

OD, optical density

PA, phosphatidic acid

PBS, phosphate buffered saline

PC, phosphatidylcholine

PDT, photodynamic therapy

PE, phosphatidylethanolamine

PEG, polyethylene glycol

PET, positron emission tomography

PG, phophatidylglycerol

PI, phosphatidylinositol

p.i., post-injection

PIP_2, phosphatidylinositiol-4,5-bisphosphate

PKC, protein kinase C

PLC, phospholipase C

PMSA, prostate-specific membrane antigen

PS, phosphatidylserine

PSA, prostate specific antigen

PSBP-6, PS-binding peptide 6

RECIST, response evaluation criteria in solid tumors

RGD, arginine-glycine-aspartate

RIF-1, rat fibrosarcoma

ROS, reactive oxygen species

SATA, N-Succinimidyl-S-acetylthioacetate

ScFv, short chain variable fragment

SPECT, single photon emission tomography

SM, sphingomyelin

SMase, sphingomyelinase

SOD1, super oxide dismutase 1

SPIO, with supramagnetic iron oxide particles

SPR, surface plasmon resonance

TF-Ag, Thomsen-Friedenreich antigen

TGFβ, transforming growth factor beta

TIM-1 and -4, phosphatidylserine receptors

TNR, tumor-to-normal ratio

TRAMP, transgenic adenocarcinoma of the mouse prostate

TUNEL, terminal deoxynucleotidyl transferase dUTP nick end labeling

VEGF, vascular endothelial growth factor

V_H, variable region light chain

V_L, variable region heavy chain

Zn-DPA, zinc(II)-dipolyamine

CHAPTER 1

INTRODUCTION

1.1. EXPOSURE OF PS ON TUMOR VASCULATURE AND TUMOR CELLS

1.1A. Regulation of PS positioning in cell membranes

In 1924, Gorter and Grendel made the revolutionary proposal that the cell membrane was two molecules thick rather than one as proposed by Irving Langmuir in 1917. [1-2] Since then, a variety of techniques including electron microscopy, x-ray diffraction, nuclear magnetic resonance (NMR) and electron spin resonance (ESR) have been used to further characterize the cell membrane's structure. The cell membrane is now known to be a phospholipid bilayer composed of four major phospholipids that are arranged asymmetrically. Two lipids with choline head groups, phosphatidylcholine (PC) and sphingomyelin (SM), are enriched in the outer membrane leaflet whereas two lipids with amine head groups, phosphatidylserine (PS) and phosphatidylethanolamine (PE), are enriched in the inner leaflet (**Fig. 1.1**). Other less abundant phospholipids that have important roles in cell signaling pathways such as phosphatidylinositol (PI), phosphatidylinositiol-4,5-bisphosphate (PIP_2) and phosphatidic acid (PA) are also enriched in the inner membrane leaflet. Most studies on membrane asymmetry have been done in erythrocytes and it has been determined that their outer

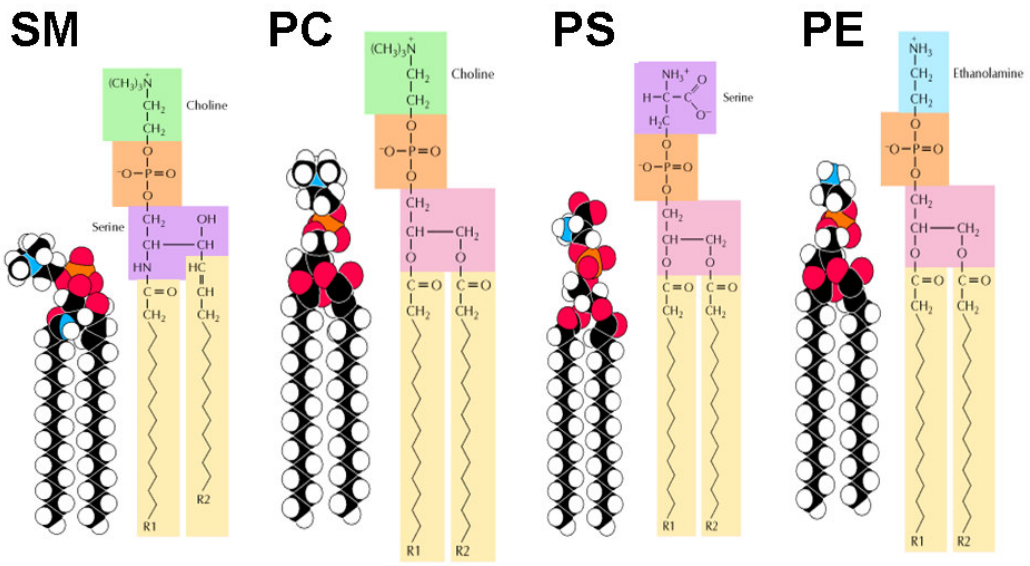

Figure 1.1 Structures of major membrane phospholipids. Sphingomyelin (SM) and phosphatidycholine (PC) are enriched in the outer membrane leaflet l whereas phosphatidylserine (PS) and phosphatidylethanolamine (PE) are enriched in the inner leaflet.(*adopted from Alberts, B. et al., 2002*) [3]

membrane leaflet is composed of 75-80% PC and SM and 20% PE, PA, PI and PIP_2.[4-6] PS is undetectable in the outer membrane leaflet.

The asymmetric distribution of membrane phospholipids begins at their synthesis. Synthesis of the major phospholipids that have a glycerol backbone (PC, PS and PE) occurs on the cytosolic side of the endoplasmic reticulum (ER). Acyl transferases successively add two fatty acids to glycerol phosphate to produce PA. Different enzymatic reactions then add the head groups to generate PC, PS or PE. The amphipathic nature of the newly synthesized phospholipids prevents them from freely moving from one side of the bilayer to the other.

Phospholipids can rapidly exchange with their neighbors in the same membrane leaflet at ~10^7 times per second translating into a lateral diffusion rate of approximately 2 microns per second. However, it can take hours or days for phospholipids to spontaneously "flip-flop" between each membrane leaflet.[3, 7] P-type ATPases known as aminophospholipid translocases (APLTs) or "flippases" remove PS and PE from the external leaflet and flip them into the cytosolic leaflet against the thermodynamic gradient.[8] PS is more tightly restricted to the cytosolic leaflet and these ATPLs have a 10-fold higher affinity for PS than PE.[9] Cytoskeletal proteins such as spectrin and band 4.1 and soluble proteins known as annexins also bind PS and help to sequester it to the inner leaflet.[10-11] SM and glycosphingolipids are synthesized within the lumen of the ER and Golgi apparatus and stay in the same leaflet in which they are made. The luminal leaflet of the ER and Golgi becomes the outer membrane leaflet when vesicles from the ER and Golgi fuse with plasma membrane.

The most pronounced consequence of a loss in membrane asymmetry is exposure of PS at the cell surface. PS is externalized during platelet activation, apoptosis, necrosis, and transformation.[12] PS externalized on the surface of platelets serves as a platform for the assembly of clotting factors. Phagocytes express the PS receptors TIM-1 and TIM-4 and PS exposed on apoptotic cells marks them for clearance from tissues and blood.[13] PS also suppresses the immune response against the apoptotic cells by stimulating the secretion of anti-

inflammatory factors such as transforming growth factor β (TGFβ) and interleukin-10 (IL-10) while inhibiting the production of pro-inflammatory factors such as nitric oxide, interleukin (IL-12), and interferon gamma (IFN-γ).[14-15]

PS externalization is stimulated by influxes of calcium from outside the cell or release of calcium from intracellular storage sites within the ER or mitochondria. High concentrations of cytosolic calcium inhibit ATPLs and activate ATP-binding cassette (ABC)-transporters know as a floppases. One floppase appears to be identical to the multidrug resistance protein 1 (MRP1) transporter encoded by the ABCC1 gene and transports all membrane phospholipids from the inner leaflet to the outer leaflet.[16-17] Another floppase ABCA1 is specific for PS and is implicated in PS externalization during apoptosis.[18-19]

Calcium influxes have also been suggested to activate a transporter known as a scramblase that can move phospholipids bidirectionally within the bilayer. Although the true identity of the transporter remains elusive, and may actually be more than one protein, scramblase activity does not seem to require ATP hydrolysis.[16] Also, the proposed mechanism for scramblase activation is controversial and may be downstream of caspase activation and independent of calcium.[20] Since the spontaneous "flip-flop" of lipids between bilayers occurs at such a slow rate, ABC-transporter and scramblase activation are perhaps more important than APTL inhibition for externalization of PS.

1.1B. PS as a marker of tumor endothelium

PS is a highly specific marker and has been found on the surface of tumor endothelial cells (EC) in all tumor models examined so far**.** Orthotopic, syngeneic, transgenic, and human tumors growing in either mice or rats have all been shown to have PS-positive vasculature. The percentage of PS-positive vessels varies between tumor type from approximately 5% to 50%. More PS-positive vessels are generally found at the tumor's center than at the periphery.[21-27] PS exposure dramatically increases when tumors are treated with chemotherapy, radiation, or androgen deprivation therapy. Following these treatments, up to 95% of the vessels can become PS-positive.[12, 23-24]
PS externalization is likely due to a number of different cellular stresses within the tumor microenvironment that injure and/or activate tumor EC (**Fig. 1.2**). Tumor angiogenesis produces tortuous and leaky blood vessels that function poorly. As a result, perfusion throughout the tumor can be inconsistent with large areas subject to hypoxia.[28] Regardless of perfusion, tumor cells can undergo high rates of glycolysis and the lactic acid generated as a byproduct of this phenomenon (known as the Warburg effect) causes the tumor microenvironment to be acidic.[29] Tumors also generate high levels of reactive oxygen species (ROS) from a number of different dysregulated metabolic processes. Abhorrent signaling from tyrosine kinase receptors can stimulate high ROS production in

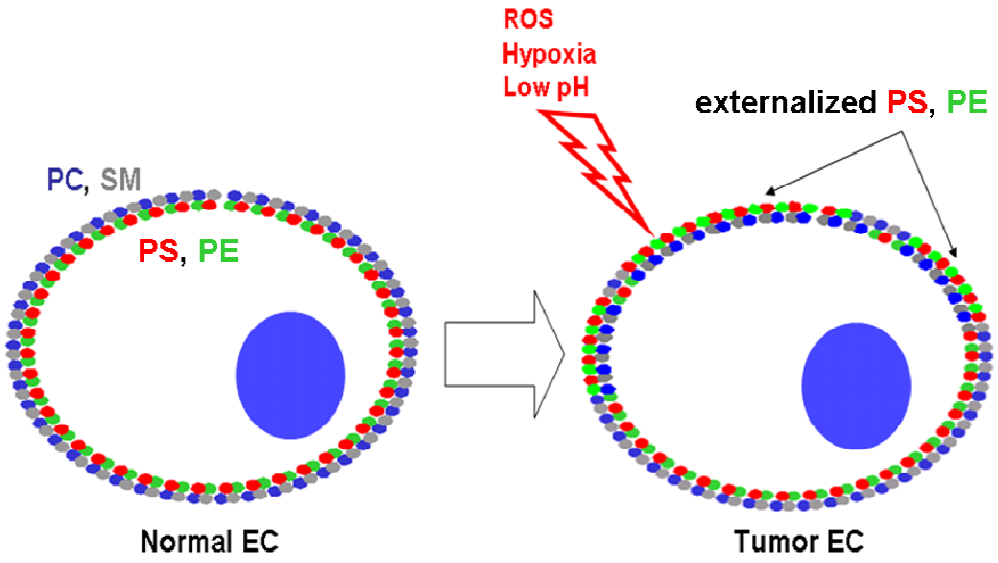

Figure 1.2. PS is externalized on tumor endothelium. The 4 major membrane phospholipids are arranged in an asymmetric bilayer. Normally, PC and SM are enriched in the outer leaflet of the bilayer and PS and PE are enriched in the inner leaflet. Oxidative stress in the form of ROS, hypoxia and low pH causes PS to flip to the outer membrane leaflet in the endothelial cells (EC) that line tumor blood vessels. A major hypothesis advanced in this thesis is that PE is also externalized on tumor EC.

mitochondria of cancer cells.[30] The ROS-producing enzyme in mitochondria, NADPH-oxidase, is often overexpressed and can also be activated by transient hypoxia.[31] Tumor-infiltrating leukocytes can discharge ROS as part of their inflammatory response.[32] Moreover, reducing enzymes that help to neutralize ROS such as catalase, superoxide dismutase, and glutathione peroxidase often show low expression and/or activity in cancer cells.[33-34] Tumor cells and tumor stromal cells secrete growth factors and cytokines that activate tumor EC.

Activated tumor EC more responsive to stress than their quiescent counterparts in normal tissues and are more likely to externalize PS in response to environmental stress and any additional stress presented by therapy.

Oxidative stress from ROS, radiation therapy, and chemotherapy can also stimulate ceramide production by the membrane protein acid sphingomyelinase (aSMase).[35-36] ASMase is related to phospholipase C (PLC) and hydrolyzes the phosphodiester bond of sphingomyelin (SM). This reaction removes the phosphorylcholine head group on SM converting it to ceramide which has a hydroxyl head group. The uncharged ceramide molecule rapidly flips between membrane bilayers and is thought to create lamella to non-lamella phase transitions that directly facilitate transbilayer movement of PS. The difference in charge destabilizes the bilayer, promotes membrane blebbing and externalization of PS.[7, 37] Ceramide also acts a pro-apoptotic signaling molecule initiating both the intrinsic and extrinsic mechanisms of cell death.[35] Ceramide-induced PS externalization may play a major role in tumor EC because EC are know to express high levels of aSMase compared to other cell types. For instance, aSMase expression has been shown to be 20-fold higher in EC than in macrophages.[38]

1.1C. PS as a marker of malignant cells

Many different types of cancer cells are also known to have PS constitutively exposed on their surface. Utsugi et al. were the first to show that tumor cells exhibit 3-7 fold more cell-surface PS than normal keratinocytes. [39] PS has since been reported to be a cell-surface marker for ovarian carcinoma, gastric carcinoma, melanoma, leukemia, prostate carcinoma, renal cell carcinoma, glioblastoma, and rhabdomyosarcoma.[40-44] The outer membrane of tumor cells can be contain as much as 9% PS and high levels of PS exposure have been correlated with progression of melanoma and poor outcome.[45] In addition, tumor cells have been shown to release PS-positive microvesicles and exosomes that can be detected in serum and ascites fluid collected from cancer patients.[46] PS is not simply a symptom of pathophysiology, but may help malignant cells escape immune surveillance by stimulating immunosuppressive cytokines (e.g. TGFβ) and, at the same time, help to recruit M2 type macrophages that secrete pro-tumorigenic growth factors (e.g. VEGF).[47]

Because exposure of PS is characteristic of many different types of cancer, lytic cationic peptides have been studied as anti-tumor drugs.[44] In one study, systemic injection of a PS-binding peptide known as D-K6L9 (MW = 1.8 kDa), composed of 6 lysines and 9 leucines in both their D and L isomeric forms, inhibited the growth 22RV1 & MDA-MB-231 tumors in mice.[48]

1.2. PS AS A TARGET FOR TUMOR IMAGING

1.2A. Introduction

Currently, the clinical evaluation of a tumor responding to therapy is based mainly on morphological and volumetric criteria. According to RECIST (Response Evaluation Criteria in Solid Tumors), a therapy-induced response is defined as a 30% decrease in the largest dimension of the tumor.[49] This could take months, during which non-responders suffer from the toxic side effects of ineffective treatment and are deprived of the appropriate treatment at the same time.[50] PS externalization, on the other hand, could potentially be detected in responding tumors as early as 24 hours after treatment. Consequently, a number of PS-targeting strategies have been studied to image tumors and their response treatment.

1.2B. Annexin V as a tumor imaging agent

The most widely studied PS-binding probe is annexin V, a 35.8 kDa protein that binds PS in a calcium-dependent manner with nanomolar affinity. The physiological function of annexin V is unknown, although some studies suggest that it may act to inhibit blood coagulation by competing with prothrombin for PS binding sites on platelets.[51]

Much research has been aimed at developing annexin V as a probe for single- photon emission computed tomography (SPECT) imaging. SPECT is less

expensive and more widely accessible than positron emission tomography (PET) which uses shorter-lived isotopes that generally necessitate an on-site cyclotron. Although SPECT is less sensitive than PET, it is significantly more sensitive than magnetic resonance imaging (MRI). Annexin V labeled with the SPECT isotope technetium-99m (^{99m}Tc) through a hydrazinonicotinamide (HYNIC) linker demonstrated a six fold increase in uptake in B-cell lymphoma treated with cyclophosphamide.[52] In another study, ^{99m}Tc-HYNIC-annexin V was injected into rats bearing hepatocellular carcinomas and images were taken at 4, 12 and 20 hours following treatment with cyclophosphamide. ^{99m}Tc-HYNIC-annexin V showed highest uptake at 20 hrs, consistent with previously established rates for PS externalization.[53] Mice bearing lymphomas or sarcomas were treated with irradiation and apoptosis and uptake of ^{99m}Tc-HYNIC-annexin V was higher in the lymphomas. In these tumors, tracer uptake showed a direct correlation with radiation dose.[54] Results from these and other preclinical studies led to phase I studies to determine the safety and biodistribution of ^{99m}Tc-HYNIC-annexin V in humans. The results of these studies showed that although >90% of blood activity cleared within 25 minutes, ^{99m}Tc-HYNIC-annexin V showed high uptake in the kidneys, liver and spleen at 25 min and 24 hrs.[55] High background signal in these organs did not prevent ^{99m}Tc-HYNIC-annexin V from effectively visualizing all of the primary head and neck tumors identified by computed tomography (CT).[56] Subsequent research has evaluated the utility of ^{99m}Tc-

HYNIC-annexin V to monitor patient response to radiation and chemotherapy. In a series of studies of lymphoma, leukemia, and non-small cell lung cancer patients treated with cisplatin and/or radiation, tumor uptake of ^{99m}Tc-HYNIC-annexin V directly correlated with clinical outcome as defined by RECIST.[57-59] Linkers other than HYNIC have been used in an effort to improve the biodistribution of ^{99m}Tc labeled annexin V. ^{99m}Tc has been conjugated to annexinV through mercapoacetyltriglycine (MAG_3)[60], ethylenedicysteine (EC)[61], 4,5-bis(thioacetamido)pentanoyl (BTAP)[62-65] and endogenous chelation sites (AGGCGH) introduced by mutation. Each of these methods showed modest improvement in renal and hepatic retention. However, disadvantages of these methods included increased uptake in other non-target organs (e.g. small intestines), decreased affinity for PS, and difficult conjugation procedures.

Annexin V has been radiolabeled with several different isotopes used for PET imaging. Annexin V reacted with N-succinimidyl-4[^{18}F]-fluorobenzoate has been shown to bind PS exposed on cancer cells treated with etoposide and the biodistribution of ^{18}F-annexin has been studied in non-tumor bearing rats.[66-67] Copper-64 (^{64}Cu)-1,4,7,10 tetraazacyclododecane-1,4,7,10-tetraacetic acid (DOTA)-streptavidin was used to visualize annexin V-biotin pre-targeted to EMT-6 mouse mammary tumors treated with photodynamic therapy (PDT).[68] Annexin V has also been labeled with iodine-124 (^{124}I) and assayed for binding to human leukemic HL60 cells treated with camptothecin. In this study, annexin V

directly iodinated using chloramine T reagent showed decreased binding compared to annexin V indirectly labeled with N-succinimidyl-3[^{124}I]-iodobenzene (the Bolton-Hunter method).[69] Collenridge et al. used ^{124}I-annexin V to image the effect of 5-fluorouracil (5-FU) treatment on RIF-1 fibrosarcomas growing in mice.[70] Dekker et al. found that an annexin V expressed as a fusion protein with maltose binding protein (MBP) was easier to purify from bacterial lysates and easier to detect by IHC than annexin V alone. Although ^{124}I-MBP-annexin V effectively detected Fas-mediated hepatic apoptosis in mice, the authors did not use the probe to image tumor apoptosis.[71]

Annexin V has also been conjugated to the near-infrared (NIR) indocyanine fluorescent dye Cy5.5 for optical imaging of PS exposed in tumors growing in mice. Cy5.5-annexin V showed colocalization with green fluorescent protein (GFP) expressing gliosarcomas and DsRed2 expressing lewis lung carcinomas and the fluorescent signal increased by 2-3 fold following cyclophosphamide treatment. Importantly, Cy5.5-annexin V was shown to bind tumor cells and tumor EC.[72] In a follow up study by the same group, Cy5.5-annexin V demonstrated higher uptake in cyclophosphamide-sensitive tumors compared to cyclophosphamide-resistant tumors following administration of the chemotherapy. The difference in tumor uptake showed good correlation with apoptosis quantified by terminal deoxynucleotidyl transferase dUTP nick end labeling (TUNEL) staining.[73-74]

Although annexin V has been examined as a potential contrast imaging agent for magnetic resonance imaging (MRI), it has not been shown to visualize tumors in this modality. Annexin V labeled with supramagnetic iron oxide (SPIO) particles demonstrated increased binding to cultured Jurkat cells treated with camptothecin and apoptotic cardiomyocytes.[75-76]

1.2C. PS-binding protein domains as tumor imaging agents

The C2A domain of synaptotagmin I binds PS and other anionic phospholipids by coordinating Ca^{2+} much like annexin V. This domain is less than half the size of annexin V having a molecular weight of 14 kDa. Zhao et al. labeled the C2A domain with SPIO particles and demonstrated that this reagent could be used for MRI detection of EL4 lymphomas treated with cyclophosphamide and etoposide.[77] The results of this study were essentially recapitulated using C2A labeled with gadolinium (Gd^{3+}) which is smaller than SPIO-C2A and gives higher signal intensities on T_1-weighted images.[78] Glutathione-S-transferase (GST) tagged C2A labeled with ^{99m}Tc has been used for SPECT imaging of mice bearing non-small cell lung tumors treated with paclitaxel.[79] This same group demonstrated PET imaging of paclitaxel-induced apoptosis in orthotopic VX2 lung tumors growing in rabbits using ^{18}F-C2A-GST.[80]

The C2 domain of lactadherin does not share homology with the C2A domain of synaptotagmin I and binds PS in a calcium-independent manner.[81] PS imaging with lactadherin has been limited to *in vitro* studies with only the biodistribution of lactadherin having been studied *in vivo*. While ^{99m}Tc-HYNIC-lactadherin exhibits lower kidney uptake than ^{99m}Tc-HYNIC-annexin V it shows much higher uptake in the liver with values greater than 50% ID/g.[82] This is most likely due to first pass clearance by the reticular endothelial system (RES) since lactadherin is known to be heavily glycosylated.

1.2D. PS-targeting peptides as tumor imaging agents

Short PS-binding peptides with molecular weights much lower than either annexin V or C2A have been used to target imaging agents to tumors. Thapa et al. identified the PS-specific peptide sequence CLSYYPSYC by screening a M13 phage display library onto PS-coated plates. This peptide preferentially bound apoptotic cells and competed with annexin V for PS-binding sites. Furthermore, they demonstrated that CLSYYPSYC labeled with fluorescein can be used for optical imaging of H460 human lung tumors growing in mice treated with camptothecin.[83] Another group screened a targeted peptide library that was designed after shared sequence homology between PS-binding domains in protein kinase C (PKC) and PS decarboxylase. This library was screened on PS-coated surface plasmon resonance (SPR) sensor chips and a PS-binding peptide with 14

residues (FNFRLKAGAKIRFG) was identified. This peptide, referred to a PSBP-6, was labeled with ^{99m}Tc and was shown to bind in melanomas treated with paclitaxel by autoradiographic analysis of tumor sections.[84] The authors did not demonstrate *in vivo* SPECT imaging of these tumors.

1.2E. PS-targeting small molecules as tumor imaging agents

Recently, several probes based on nonpeptidic small molecules have been shown to image PS in tumors. Butyl-2-methyl-malonic acid (ML-9) is an ApoSense probe that mimics γ-carboxyglutamic acid (Gla) and has a molecular weight of only 206 Da. ML-9 labeled with tritium (^{3}H-ML-9) showed a >5-fold increased uptake in CT-26 colon adenocarcinomas treated with doxorubicin or a combination of carmustine and 5-FU.[85] Another ApoSense derivative, ^{18}F-5-fluoropentyl-2-methyl-malonic acid (^{18}F-ML-10), visualized irradiated brain metastases in human patients. Uptake of this probe was found to be predictive of tumor response to treatment as indicated by MRI several months later.[86] Bradley D. Smith's group at the University of Notre Dame has shown that Zn^{2+} coordination complexes can be used for optical imaging of tumors. They have demonstrated that zinc(II)-dipolyamine (Zn-DPA) conjugated to a NIR dye specifically labeled both PAIII rat prostate tumors and EMT-9 mouse mammary tumors with low background in non-target organs.[85, 87]

1.2F. PS-targeting antibodies as tumor imaging agents

The PS-targeting antibody known as bavituximab was initially developed for the treatment of solid tumors. PS was first detected on the surface of tumor endothelium using a rat monoclonal IgM known as 9D2. 9D2 was generated by immunizing Lewis rats with murine brain-derived endothelial (bEnd3) cells treated with hydrogen peroxide (H_2O_2) to induce PS externalization. 9D2 was then identified by screening supernatants from rat splenocyte/myeloma hybridomas for PS binding activity.[21] Similarly, a mouse monoclonal IgG3 known as 3G4 was generated by immunizing BALB/c mice with H_2O_2-treated bEnd3 cells.[22] An antibody known as 2aG4 was then created by recombining the Fv region of 3G4 with a murine IgG2a heavy chain constant region.[23] IgG2a has higher affinity for FcγR receptors on mouse immune cells than IgG3 and therefore 2aG4 was designed to have a more potent immunostimulatory effect than 3G4. Preclinical studies with 2aG4 led to the development of a human-mouse chimeric antibody for clinical use known as bavituximab. To make bavituximab, the Fv regions of 3G4 were fused to a human IgG1κ constant region.[12]

None of the bavituximab family members bind PS directly, but instead recognize a PS-binding serum protein known as beta2-glycoprotein 1 (β2GP1). The antibodies crosslink two molecules of β2GP1 and the resulting complexes bind PS extremely high affinity (K_d = 0.4 nM). β2GP1 is related to complement

control proteins and consists of 5 Sushi domains. Domains I-IV are regular repeats of approximately 60 amino acids. Domain V is slightly larger having 82 amino acids, including clusters of positively charged and hydrophobic amino acids that function in binding to PS.[88-89] Bavituximab, 2aG4, and 3G4 recognize human and rat β2GP1, but not mouse β2GP1. Thus these antibodies require co-injection of human β2GP1 for studies in mouse models of cancer, which limits their use to immunodeficient animals. Nonetheless, 3G4, 2aG4, and bavituximab have been shown to inhibit tumor growth in multiple rodent models of cancer.[22-25, 90] PS-targeting antibodies may inhibit PS-mediated immunosuppression. Macrophages in these tumors are skewed to the M1 tumoricidal phenotype and show enhanced secretion of pro-inflammatory cytokines such as TNFα and IL-1β. Therefore, the anti-tumor effects of these antibodies may be attributed to destruction of tumor endothelium by antibody-dependent-cell-mediated cytotoxicity (ADCC).[12]

Although the normal physiological function of β2GP1 has not been defined, it has been shown to interact with autoantibodies responsible for antiphospholipid syndrome (APS). However, unlike APS antibodies, bavituximab antibodies do not cause coagulation disorders and thrombosis. The safety profile of bavituximab is well established having been administered to human patients in several phase I and phase II clinical trials. A phase I trial found that a dose of 3 mg/kg bavituximab was well-tolerated in patients with advanced

cancers that did not respond to conventional therapy. The antibody demonstrated a safe and favorable biodistribution with minimal side effects. In a phase II trial, 61% (28/46) of breast cancer patients given a combination of bavituximab and docetaxel achieved an objective response compared to a 41% response rate reported for breast cancer patients treated with docetaxel alone in a separate study. Bavituximab was also given to non-small cell lung cancer (NSCLC) patients in combination with carboplatin and paclitaxel. 65% (11/17) of evaluable patients achieved an objective response and the median progression-free survival for all patients (21) was 6.5 months compared to 4.2-4.5 months reported in a different trial studying NSCL patients treated with chemotherapy alone.[12]

Recently, Jennewein et al. demonstrated that bavituximab can be also used for *in vivo* imaging of tumor vasculature.[26] Bavituximab was first derivatized with N-Succinimidyl-S-acetylthioacetate (SATA) to introduce an average of 3.5 thiol groups per antibody and then labeled with the positron emitting isotope Arsenic-74 (^{74}As). ^{74}As was used because its' long half-life ($T_{1/2}$ = 17.8 days) is compatible with the long serum half life of bavituximab. Subcutaneous Dunning prostate R3227-AT1 tumors were clearly delineated in PET images of rats injected with ^{74}As-bavituximab. The tumor-to-background ratio was optimal at 72 hrs post-injection with ^{74}As-bavituximab uptake 22-fold higher in the tumor than in the liver. Autoradiographic and immunohistochemical analyses of the

tumors showed that ^{74}As-bavituximab binding was highest at the tumor periphery and was specific to tumor endothelium.[26]

1.2G. Need for new agents

Although the PS-imaging agents described in the current literature have demonstrated some prognostic value, there is still a need to develop better agents. The translation of annexin V-based probes to the clinic is limited by several issues including: 1) poor pharmacokinetics, 2) low *in vivo* stability, 3) slow on-rates, 4) high cost, 5) difficulty in production, and 6) the requirement of micromolar concentrations of Ca^{2+}.[91] Of these issues, poor pharmacokinetics may be the most problematic because high accumulation in normal tissues prevents identification of tumors throughout the abdominal region. Annexin V-based probes demonstrate less than favorable biodistributions regardless of radioisotope, conjugation method, or imaging modality (**Fig. 1.3A and 1.3B**). Probes smaller than annexin V (36 kDa) may yield better signal to background ratios due to their ability to pass through the glomerulus and clear the circulation at faster rates. Unfortunately, probes targeted by C2A domains (14 kDa) also have high background signals (**Fig. 1.3C**) and bind PS (K_d=15-40 nM) with an approximately 10-fold lower affinity than annexin V (K_d=0.1-2 nM).[92]

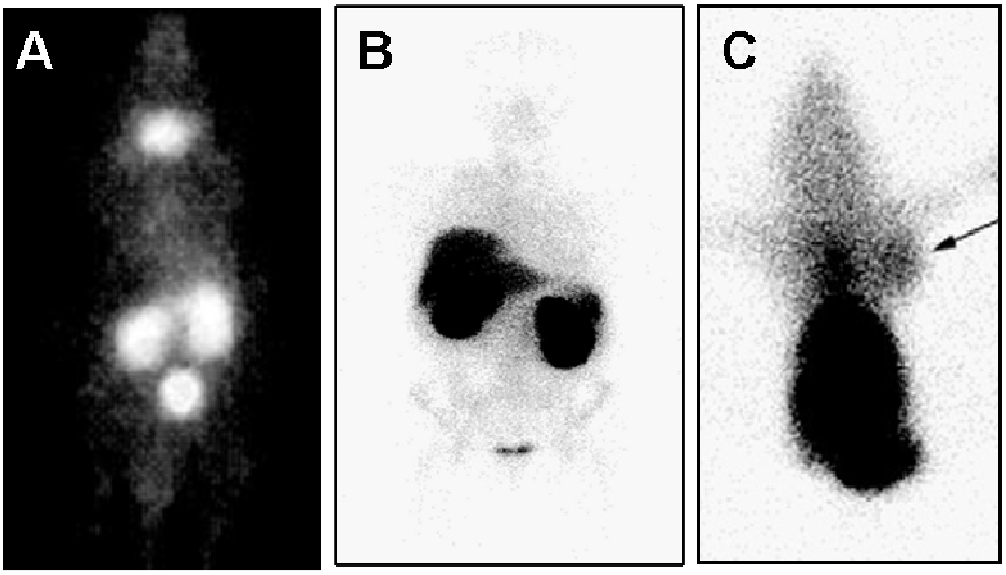

Figure 1.3. Biodistribution of PS-targeting imaging agents. A) PET image showing biodistribution of ^{124}I-annexin V in a mouse (adopted from Glaser et al., 2003) [69] B) SPECT image showing biodistribution of ^{99m}Tc-HYNIC-annexin V in a human (adopted from Dekker et al., 2011) [50], and C) SPECT image showing biodistribution of ^{99m}Tc-C2A-GST in a mouse bearing a tumor (arrow)**.** (adopted from Wang et al. 2008) [79]

The PS-binding peptide PSBP-6 is only 1.6 kDa, but binds PS with ~100-fold lower affinity than annexin V having a K_d of approximately 100 nM. It also shows high retention in the liver and kidneys despite its small size. The reported biodistribution of PSBP-6 in terms of percent injected dose per gram (%ID/g) is approximately 10% for liver, 15-20% for kidneys, and <5% for tumor.[84] The preliminary studies done on the PS-targeting small molecules Zn-DPA (1.5 kDa) and ML-9 (0.2 kDa) suggest that these agents may have more desirable biodistribution profiles. However, Zn-DPA has a K_d in the micromolar range and

no binding affinity constant was reported for ML-9. The reports for both of these compounds were relatively incomplete overall and further characterization will be required before their true potential for tumor imaging can be evaluated. Finally, the long incubation time and "exotic" isotope required for ^{74}As-bavituximab PET imaging are less than ideal for a clinical agent.

1.3. 1N11F(ab')$_2$ AS A TUMOR IMAGING AGENT

1N11 (aka PGN635) is a new, fully human anti-PS antibody that displays higher specificity than annexin V and higher affinity than most PS-targeting agents. 1N11 is the latest member of the bavituximab family of antibodies described in **Section 1.2F** and also binds PS indirectly through β2GP1. 1N11 was developed by Affitech A/S by screening a large phage library for single chain variable fragments (ScFv) that bind PS. The ScFv that were selected were affinity matured and then converted to a full length, fully human IgG. Biacore analysis of the binding properties of 1N11 revealed that it had similar affinity for β2GP1 as bavituximab with a measured K_d of 1.8 nM. Bavituximab, 3G4, 2aG4 recognize domain II of β2GP whereas 1N11 and APS autoantibodies bind domain I. β2GP1 normally exists in a closed loop conformation in serum with domain I interacting with domain V. APS autoantibodies disrupt this interaction and activate β2GP1 so that it binds to normal vasculature, probably via the Apo ER2 domain which becomes exposed in domain I. This leads to activation of the endothelium,

surface expression of leukocyte adhesion molecules and procoagulant changes.[93] 1N11 recognizes a different epitope within domain I and only causes β2GP1 to unfold when it encounters PS expressed on the surface of tumor vasculature or tumor cells (*Peregrine Pharmaceuticals, unpublished data*). 1N11 is therefore not an APS-inducing antibody.

1N11 has been shown to localize specifically to PS-positive tumor vasculature in mice (*Yi Yin, unpublished results*). It exhibits similar pharmacokinetics to bavituximab and has also demonstrated a similar safety profile in animals. Therefore, the PET imaging study done with ^{74}As-bavituximab may be considered proof-of-principle for imaging tumors with 1N11.

The high binding specificity and high affinity of 1N11 are characteristics of an ideal imaging agent. Unfortunately, the long serum half life of full-length IgG is not. Slow glomerular filtration of IgG due to its large size (180 kDA) is one kinetic factor that contributes to a long serum half life. However, size alone cannot account for the fact that some IgGs can remain in the circulation for up to 3 weeks. The Fc portion of IgG interacts with neonatal Fc receptors (FcRn; Brambell receptors) on normal vascular EC that rescue IgG from early endosomes and return them to the bloodstream. [94-96] Therefore, one strategy to increase the blood clearance rate of antibodies is to remove the Fc domain by enzymatic cleavage. Pepsin cleaves IgG at residues just above the hinge region to generating what is known as a fragment antigen-binding dimer ($F(ab')_2$) (**Fig. 1.4**). Wahl et

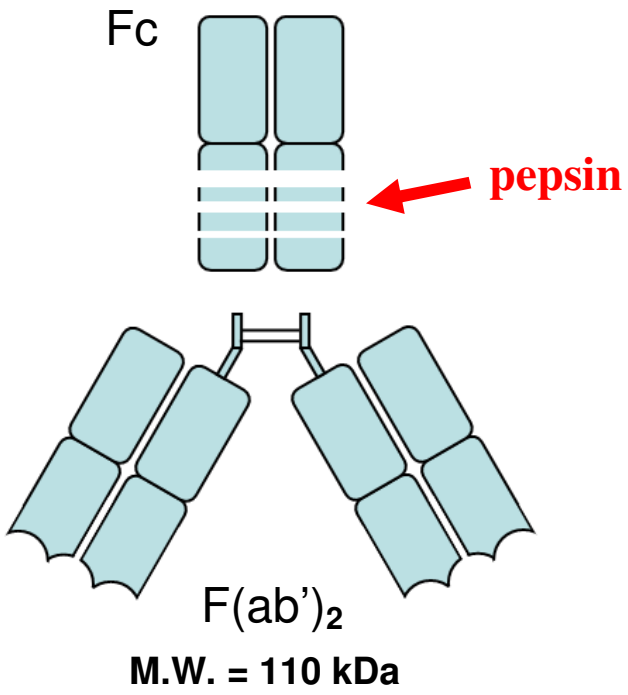

Figure 1.4. Enzymatic cleavage of IgG to F(ab')2. Pepsin cleaves full length IgG (MW = 160 kDa) just above the hinge region to generate F(ab')2 (MW = 110 kDa).

al. were the first to show that radiolabled anti-carcinoembryonic antigen (CEA) $F(ab')_2$ injected into hamsters cleared the circulation approximately 70% faster than full length anti-CEA IgG. [97] This faster clearance rate allowed the authors to efficiently image human colon carcinoma xenografts at 2 days post-injection instead of 6. Covell et al. reported a mean residence time in the body of 0.5 days for an $F(ab')_2$ with no known binding specificity.[98] The full length IgG1 version of the same antibody had a mean residence time of 8.5 days.

1N11 F(ab')$_2$ has the potential to be extremely effective for imaging PS exposed in tumors. The pharmacokinetic characteristics of 1N11 F(ab')$_2$ in terms of binding affinity, binding specificity, *in vivo* stability, and biodistribution are potentially unmatched by any of the previously described PS-targeting probes. Although ^{74}As-bavituximab's potential for tumor imaging has been demonstrated, 1N11 F(ab')$_2$ should yield the required tumor:background ratios at much faster rates. This may allow the use of shorter lived PET isotopes such as Copper-64 (^{64}Cu, $t_{1/2}$ = 12.7 hrs), Zirconium-89 (^{89}Zr, $t_{1/2}$ = 78.4 hrs) and Iodine-124 (^{124}I, $t_{1/2}$ = 100.3 hrs).

1.4. DURAMYCIN AS A TUMOR IMAGING AGENT

PS and PE are regulated by the same membrane transporters and both phospholipids become externalized in the same membrane patches and blebs on individual apoptotic or irradiated cells.[99]-[100] Therefore, it is reasonable to hypothesize that PE may also serve as a marker of tumor EC and that PE-targeting constructs may function much like those that target PS (**Fig. 1.5**). Duramycin (aka PA58009 and Moli1901) is a PE-binding peptide produced by the bacterium *Streptocercillium cinnamoneous* that has unique physiochemical properties that may make it an ideal imaging agent. It has a molecular weight of approximately 2.0 kDa and binds PE with a K_d of 4 to 6 nM.[101] Therefore, it is much smaller

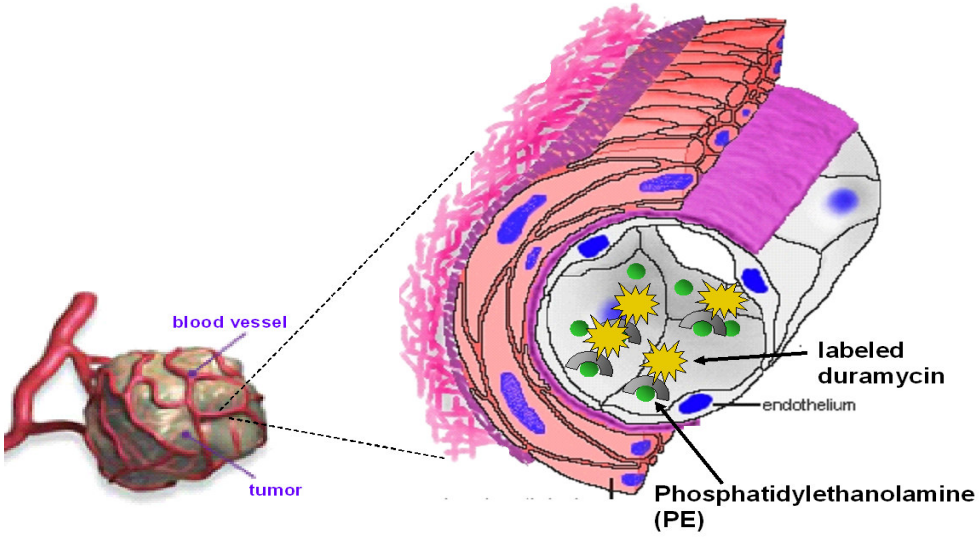

Figure 1.5. Duramycin as a potential tumor imaging agent. The PE-binding peptide duramycin may be used to target imaging agents to tumor vasculature based on its unique binding characteristics and pharmacokinetic properties.

than annexin V or C2A and binds with much higher affinity than C2A, PSPB-6, or Zn-DPA.

Duramycin is one of the smallest known polypeptides to form a three-dimensional binding pocket and binds PE in a 1:1 ratio with exclusive specificity.[101] The hydrophobic binding pocket is stabilized by four thioether linkages shared by atypical amino acids known as lanthionines (**Fig. 1.6**). The lanthionines are formed by posttranslational modification of Ser-4, Ser-6, Thr-11 and Thr-18. Both serines are dehydrated to didehydroalanine whereas the threonines are dehydrated to didehydrobutyrine. Nucleophilic addition from the side chain of cysteine residues then converts didehydroalanine to lanthionine

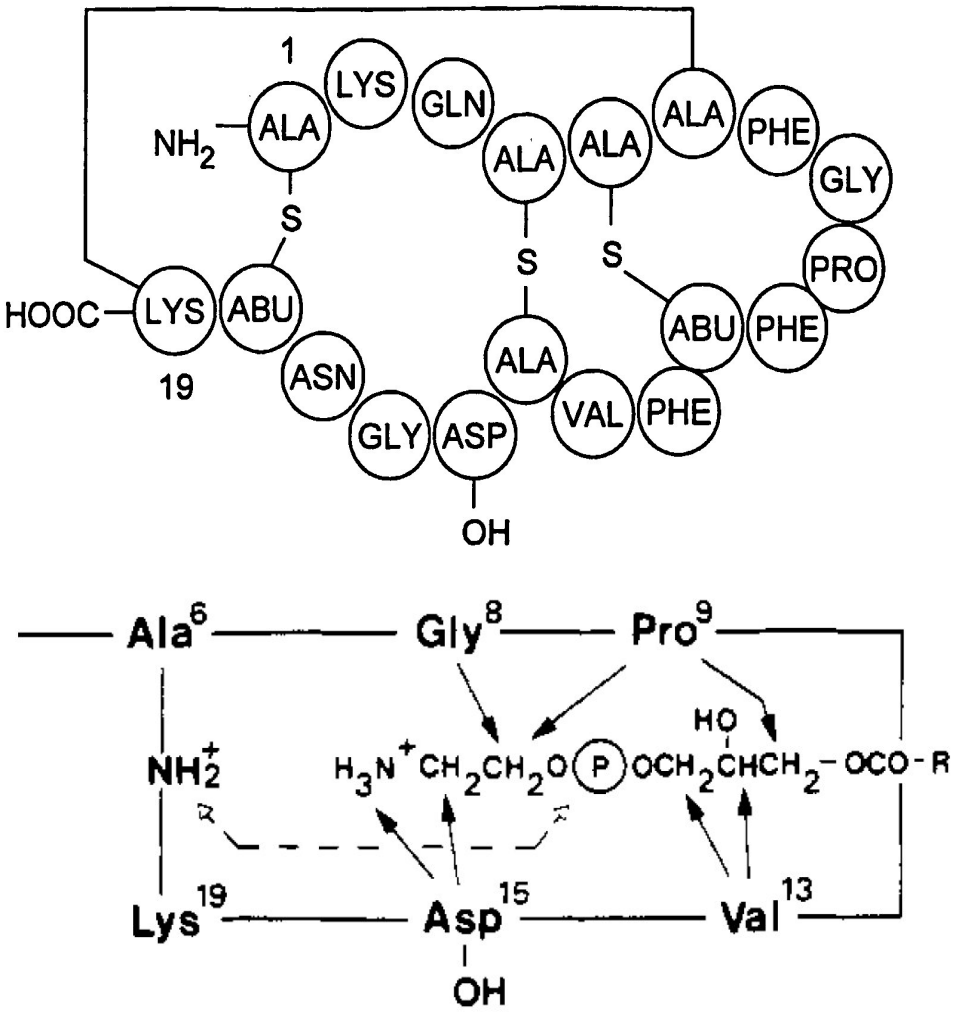

Figure 1.6. Intermolecular interactions between duramycin and PE. NMR analyses revealed a critical ionic bond between Asp-15 and the amine head group on PE. Hydrophobic interactions between Pro-9 and Val-13 and the glycerol backbone on PE help to further stabilize binding.[102]

and didehydrobutyrine to methyllanthionine. Ser-4, Thr-11, and Thr-18 react with Cys-14, Cys-5, and Cys-1 respectively. A reaction between the didehydroalanine from Ser-6 and the C-terminus forms lysoalanine.[103]

Duramycin's name is derived from its resistance to heat and proteolytic degradation that these thioether linkages confer.[104] Duramycin is closely related to another PE-binding lantibiotic peptide named cinnamycin (Ro09-0198), differing in sequence by a single amino acid. The second residue in cinnamycin is Arg instead of Lys, but the remaining 18 amino acids and thioether bonds are completely conserved.

The intermolecular interactions between PE and specific amino acids in cinnamycin have been mapped by two dimensional proton NMR analyses and are likely to be identical for duramycin. One ionic bond is formed between the negatively charged carboxylate from Asp-15 and the positively charged ammonium group of PE. Another ionic bond is formed between the phosphate on PE and the amine shared between Ser-6 and the C-terminus. These ionic bonds are stabilized by hydrophobic interactions throughout the binding pocket: Gly-8 interacts with the ethanolamine headgroup, Val-13 interacts with the glycerol backbone, and Pro-6 interacts with both (**Fig. 1.6**).[102] Duramycin preferentially binds highly curved membranes suggesting further hydrophobic interactions with the fatty acid tail of PE.[101] Importantly, duramycin's binding pocket does not accommodate any other membrane lipid. Although Navarro et al. first reported that duramycin can also recognize monogalactosyl diglyceride (MGDG)[105], Iwamoto et al. found that pre-incubation with MGDG liposomes had no effect on duramycin-induced hemolysis of rabbit erythrocytes.[101] It is

possible that, in the earlier studies, the MGDG was contaminated with traces of PE.

Duramycin possesses two primary amines at its N-terminus that can be used for covalent reactions with reporter molecules used for imaging. There is an α-amino at the N-terminus and an ε-amino presented by the side chain on Lys-2. The proton resonances of these residues are not shifted when duramycin interacts with PE, indicating that they are not directly involved in binding.[102] Duramycin conjugated to fluorescent liposomes was used to visualize PE exposed on the surface of irradiated EC.[100] Duramycin has also been derivatized with HYNIC and labeled with ^{99m}Tc for SPECT imaging. *In vitro* binding tests showed that ^{99m}Tc-duramycin preferentially bound apoptotic lymphocytes over healthy cells and that this binding could be competed specifically by PE-containing liposomes. When ^{99m}Tc-duramcyin was intravenously injected into rats with acute myocardial infarctions, it clearly labeled the infarct sites and showed low uptake in healthy tissues other than the kidneys and bladder. After 1 hr., the authors reported a 4.0 %ID/g for ^{99m}Tc-duramycin at the infarct site and a 12:1 infarct-to-muscle ratio. Uptake in normal tissues (brain, lung, liver, spleen, intestine, and bone) was less than 0.40 %ID/g; except for the kidneys which had a %ID/g of 2.32 $\pm$ 0.48.[106] Importantly, hepatic uptake of ^{99m}Tc-duramycin was much lower than reported in biodistribution studies of tritiated duramycin (^{3}H-duramcyin) injected into rats. ^{99m}Tc-duramycin activity in the liver was 0.28

%ID/g after 1 hr compared to 32.9 %ID/g for ^{3}H-duramycin after 168 hr.[107] Uptake of the positively charged ^{3}H-duramycin in the liver is likely mediated by cationic transporters, such as the organic cation transporter (OCT) and the multidrug and toxin extrusion (MATE) transporter, whereas the negatively charged ^{99m}Tc-duramycin may escape recognition by such transporters.[108]

Intranasal administration of relatively high concentrations of duramycin has been shown to stimulate chloride (Cl^-) secretion and rehydration in airway epithelium. Duramycin does this by forming channels in the epithelial cells, stimulating release of Ca^{2+} from intracellular stores, and activating protein kinase C (PKC).[109-110] The results of phase I and phase II clinical trials studying duramycin as a potential treatment for cystic fibrosis (CF) suggest that the peptide may be safely administered to humans. Daily inhalation of 2.5 mg duramycin was well tolerated in CF patients treated over a course of 25 days with no evidence of edema, erythema, ulceration, or impairment of nasal function.[111]

1.5. OPTICAL AND PET IMAGING OF TUMORS

1.5A. Introduction

Cancer imaging modalities can be divided into two basic categories: 1) morphological/anatomical imaging and 2) molecular imaging.[112] Computed tomography (CT), MRI, and ultrasound are all examples of morphological/anatomical imaging techniques. Although these modalities are

characterized by high spatial resolution they suffer from limited sensitivity. Molecular imaging techniques such as SPECT, PET, and optical imaging demonstrate much higher sensitivities. These techniques can be used for non-invasive assessment of tumor physiology at the cellular or even sub-cellular level. The major advantages and disadvantages of the various tumor imaging modalities are outlined in **Table 1**. Two molecular imaging modalities relevant to my thesis project, optical and PET imaging, will be discussed in further detail in the following sections.

Imaging Modality	Advantages	Disadvantages
PET	High sensitivity, quantitative, unlimited depth penetration, clinical translation	Cost, limited spatial resolution
SPECT	Clinical translation, unlimited depth penetration	Low spatial resolution
MRI	Clinical translation, high resolution / soft-tissue contrast	Low sensitivity, cost, imaging time
CT	Clinical translation, high resolution	No target specificity, radiation exposure, poor soft-tissue contrast
Ultrasound	Clinical translation, high spatial & temporal resolution, low cost	Variability with operator, targeted imaging limited to vasculature
Optical	High sensitivity, low cost, high-throughput screening possible	Limited clinical translation, low depth penetration

Table 1. Advantages and disadvantages of different tumor imaging modalities.

1.5B. Optical imaging

Recent improvements in optical instrumentation have lead to increased interest in the use of optical imaging for cancer diagnosis.[113] Lasers can be used to efficiently excite fluorescent probes *in vivo* and the resulting low-energy emissions can be detected with highly sensitive charge-coupled device (CCD) cameras. The development of near-infrared (NIR) probes has also made optical imaging of tumors more feasible. As the long excitation and emission wavelengths (700-1000 nm) used for NIR imaging pass through tissue, they are less subject to absorption and scattering than the shorter wavelengths used for other fluorescent probes. In addition, NIR imaging avoids autofluorescence in tissues from hemoglobin, lipids, melanin and other biomolecules that absorb light in the visible range (400-700 nm). NIR probes can be detected at tissue depths of up to several centimeters and may be used to image any tumor close to the surface of the body or to surfaces accessible by endoscope. Tumors located in the skin, breast, colon, esophagus, stomach, and bladder are among the possible candidates.[114] Guidance during surgery is another promising clinical application of optical imaging. NIR probes that specifically accumulate in malignant tissue could be used to define tumor margins and allow a more complete resection of the tumor. For example, glioblastoma multiforme (GBM) is a highly infiltrative tumor that is difficult to remove surgically without

damaging the surrounding brain tissue. Optical probes could help identify residual disease and maximize the effectiveness of surgery.

Carbocyanine dyes are the most commonly used reporters for NIR imaging. The majority of these dyes have a basic structure that consists of highly conjugated polymethine units flanked by aromatic groups (**Fig. 1.7**).[113] Indocyanine green (ICG) represents the first generation of these compounds and has been approved by the FDA for clinical use. ICG does not possess any binding specificity and only passively accumulates in tumors by extravasation through the leaky vasculature produced by pathological angiogenesis.[115-117] Additional disadvantages of ICG include high background signals, poor *in vivo* stability, and rapid photobleaching. Therefore, derivatives of ICG have been made to facilitate conjugation to targeting moieties and improve its pharmacokinetic properties. Cy5.5 (GE Healthcare), Dylight 680-800 (Thermo Fisher Scientific Inc.), Alexa Fluor 750 (Invitrogen), and IRDye 800CW (LiCOR Biosciences) are commercially available dyes that are currently being used to make a wide variety of targeted NIR optical imaging agents. Although Cy5.5 is superior to ICG, its excitation and emission maxima (675 / 694 nm) border the visible spectrum and can result in high background signals.[72, 118] The other NIR probes have

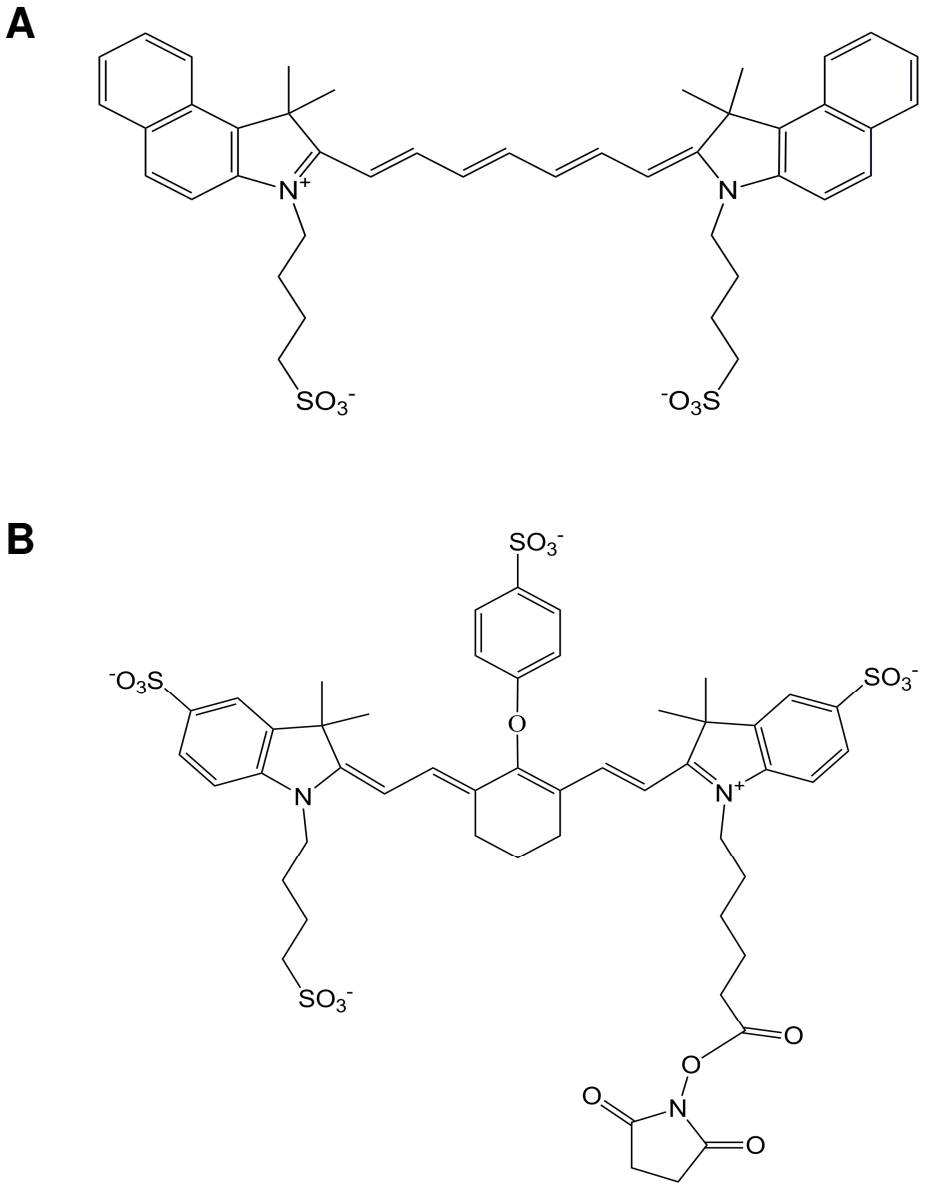

Figure 1.7. Carbocyanine dyes used for NIR imaging. A) Structure for indocyanine green (ICG, MW = 775 Da). ICG is hydrophobic and not easily conjugated to targeting moeities. ICG is also characterized by poor *in vivo* stability and rapid photobleaching. B) Structure for IRDye 800CW (MW = 1166 Da). The N-hydroxysuccinimide (NHS) ester derivative shown is easily conjugated to peptides and antibodies. IRDye 800CW also displays higher fluorescence intensity and more favorable pharmacokinetics compared to ICG.

excitation/emission further removed from the visible spectrum. IRDye 800CW, for example, emits at 789 nm and can yield an approximately 6-fold higher tumor-to-background ratio than Cy5.5.[119] IRDye 800CW also exhibits high solubility, a high molar extinction coefficient (240,000 L/mol cm), low nonspecific binding, and a more than 20-fold brighter fluorescence than ICG.

NIR dyes have been conjugated to a several different ligands that bind to molecules overexpressed on the surface of tumor cells or tumor endothelium. One of the initial studies was done by Becker et al. who showed that octreotate conjugated carbocyanine dyes specifically labeled human primary neuroendocrine tumors growing in mice that overexpress the somatostatin receptor.[120] Another study showed that epidermal growth factor linked to Cy5.5 (EGF-Cy5.5) only imaged MDA-MB-468 human breast xenografts with high epidermal growth factor receptor (EGFR) expression and did not image MDA-MB-435 tumors with low EGFR expression.[121] HER-2 specific Affibody molecules labeled with Alexa Fluor 750 have been shown to visualize HER-2-positive SKBR-3 breast tumors growing in mice. A bivalent Affibody fused to the albumin-binding domain (ABD) produced a tumor-to-background ratio of 4.5 ± 1.5, 48 hrs after injection. Although a monovalent HER-2 Affibody cleared the circulation at much faster rate and allowed imaging to be performed within 4 hr, it produced a maximum tumor-to-background ratio of only 2.5 ± 0.9.[122] Peptides containing an arginine-glycine-aspartate (RGD) motif are known to bind $\alpha_v\beta_3$ integrins

overexpressed in tumors and a number of different NIR labeled RGD constructs have been studied. Wang et al. used cyclo(Lys-Arg-Gly-Asp-Phe) [c(KRGDf)] peptide to target Cy5.5 to $\alpha_v\beta_3$ integrins in KS1767 Kaposi's human sarcomas and M21-L human melanomas growing in mice. The reported tumor-to-background ratios were 5.5 for KS1767 tumors and 2.3 for M21-L tumors.[123] Tetramerization of another RGD peptide using was shown to have improved targeting of Cy5.5 to $\alpha_v\beta_3$ integrin expressing xenografts over the RGD monomer.[124] Furthermore, an IRDye 800CW labeled RGD tetramer containing poly ethylene glycol (PEG) linkers was found to have a more favorable biodistribution that an RGD tetramer without PEG linkers.[125] Uptake of NIR-folate has been shown to be 2.4-fold higher in folate receptor (FR)-positive nasopharyngeal epidermoid carcinomas than in FR-negative HT1080 lung tumors.[126] An antibody fragment (arcitumomab Fab') directed against carcinoembryonic antigen (CEA) has been used for NIR imaging of LS-174T human colon carcinomas growing in mice.[127] Optical imaging could be also be used to compliment other tumor imaging modalities. For instance, imaging methods with greater depth penetration such as PET or MRI could be used to locate the tumor prior to surgery and the optical reporter could be used as a guide during surgery. This type of multimodality imaging was demonstrated by Moore et al. who showed that mucin I-binding peptides labeled with both Cy5.5 and

SPIO particles could be used for both optical and MRI imaging of LS174T tumors growing in mice.[128]

Molecular imaging has its roots in the nuclear imaging modalities such as PET and SPECT, but optical imaging is emerging as a safe, cost-effective alternative that is highly sensitive and quantitative. While new optical imaging agents may be particularly useful for assessing drug pharmacokinetics and pharmacodynamics in small animal models, they also have the potential to translate to the clinic.

1.5C. PET Imaging

1.5C.1. Introduction

Positron emission tomography (PET) is the most sensitive tumor imaging modality that is routinely used in the clinic today. During a PET scan, positrons emitted from nucleus of the injected PET isotope participate in an annihilation reaction with nearby electrons (generally within a radius of 1 mm) generating a pair of 511 keV gamma photons that travel in opposite directions (~180º).[129] Coincident detection of these gamma photons by a ring of detectors surrounding the patient forms a "line of response" (LOR) and multiple LORs are used to reconstruct two-dimensional or three-dimensional (3D) images. PET is several magnitudes more sensitive than MRI, requiring probe concentrations of as little as 10^{-11}-10^{-12} M.[112] Moreover, because the intensity of the signal is proportional

to probe concentration at the target site, PET imaging allows quantitative comparisons. The spatial resolution of PET is limited to approximately 4-6 mm, but is generally better than which can be achieved with SPECT. PET can also be combined with computed tomography (PET-CT) to determine the anatomical location of the probe more accurately. Using scanners capable of both modalities, a CT scan can be performed prior to the PET scan and the two 3D images can be superimposed on one-another.

Many elements have positron emitting isotopes including carbon (^{11}C), nitrogen (^{13}N), oxygen (^{15}O), and fluorine (^{18}F) could be potentially incorporated into biomolecules or drugs as a PET probe. Nonetheless, the only PET probe currently approved by the FDA for clinical use in humans is [^{18}F]fluorodeoxyglucose (^{18}F-FDG). Tumors undergo high rates of glycolysis relative to normal tissue and ^{18}F-FDG is a glucose analog that can be used for tumor imaging. Once imported into the cell, ^{18}F-FDG is phosphorylated by hexokinase to ^{18}F-FDG-6-phosphate. The negatively charged ^{18}F-FDG-6-phosphate cannot be released from the cell and also lacks the 2' hydroxyl found on glucose to be metabolized further by glycolytic enzymes. Thus, ^{18}F-FDG preferentially builds up in cells utilizing high amounts of glucose. ^{18}F-FDG has been used for imaging many cancers including lymphoma, lung cancer, colorectal cancer, and head and neck cancer.[130-131] Diminished uptake of ^{18}F-FDG by a tumor following treatment can be indicator that the tumor is responding to the

treatment. For example, Van den Abbeele et al. have shown that ^{18}F-FDG can be used to identify of colorectal tumors responding to imatinib treatment as early as 24 hr after the first treatment.[132] There are, however, many disadvantages to using ^{18}F-FDG for imaging tumors. Some normal tissues such as the brain and kidneys use high levels of glucose and therefore labeled by ^{18}F-FDG. In fact, all cells metabolize glucose to some extent and ^{18}F-FDG imaging suffers from relatively high background signals throughout the body. Also, decreased uptake of ^{18}F-FDG in tumors may not indicate tumor cell death, but could instead occur from the down-regulation of glucose transporters in viable tumor cells.

1.5C.2. PET imaging of prostate cancer

^{18}F-FDG is not effective for the imaging and diagnosis of prostate cancer.[34] Well differentiated, androgen-dependent prostate tumors do not exhibit the high rates of glucose metabolism seen in other tumor types. Although some less-differentiated, androgen-independent tumors utilize glucose, the signal can be obscured by intense background signals from accumulation of the probe in the bladder. One study found no difference in ^{18}F-FDG uptake between patients with benign prostatic hyperplasia (BPH), prostate carcinomas, local recurrence, and those with only post-operative scar tissue.[133] Therefore, much research has been devoted to the development and validation of new PET imaging probes for prostate cancer.

Prostate-specific antigen (PSA) is an androgen-regulated 33 kDa serine protease that has long been the most commonly used marker for prostate cancer. However, PSA is not efficient target for PET imaging probes due to low sensitivity and limited specificity. PSA levels are sometimes virtually undetectable in patients with advanced disease or unusually high in patients with BPH. Recent evidence suggests that prostate-specific membrane antigen (PMSA) may be a better marker. PMSA is a glycoprotein that is highly expressed in most prostate cancers and is upregulated as disease progresses towards androgen-independence and metastasis.[134-135] Protascint (capromab pentitide) is a commercially available anti-PMSA antibody labeled with Indium-111 (^{111}In) for SPECT imaging. However, Protascint is a relatively inefficient imaging agent because it recognizes an intracellular epitope on PMSA and only binds in necrotic tissue. J591 is a humanized anti-PMSA antibody that recognizes an extracellular epitope on PMSA and has been labeled with ^{64}Cu and ^{89}Zr for use as a PET probe.[136-137] ^{89}Zr –DFO-J591 labeled subcutaneous LNCaP tumors growing in mice with tumor-to-muscle ratios >20:1 between 48 and 144 hr after administration.[137] Another cell surface glycoprotein that is expressed in normal human prostate and overexpressed during malignancy is prostate stem cell antigen (PSCA). Lepin et al., successfully imaged LAPC-9 prostate tumors in mice with ^{124}I-labeled anti-PSCA minibodies.[138]

Choline and acetate have been labeled with either ^{18}F or ^{11}C and used to identify prostate tumors.[139-141] Rapidly dividing cells require high rates of membrane synthesis and both choline kinase and fatty acid synthase have been shown to be upregulated in prostate cancer. Choline kinase phosphorylates choline and fatty acid synthase metabolizes acetate and are both incorporated into the cell membrane in the form of PC. Choline uptake has been shown to be higher than acetate uptake in prostate tumor cells under aerobic conditions. Conversely, acetate uptake was shown be higher in hypoxic prostate tumor cells.[142] Increased amino acid metabolism in prostate carcinomas has also been targeted for PET imaging. ^{11}C-methionine has been used for the detection of prostate cancer in patients with high prostate serum antigen (PSA) and repeatedly negative biopsies.[143] An ^{18}F-labeled L-leucine analog, anti-amino-3-^{18}F-fluorocylcobutane-1-carboxylic acid (^{18}F-FACBC), exhibited low background signals in the bladder and was able to detect primary and recurring prostate tumors.[144] It is important to note that neither lipid or amino acid metabolism is specific for prostate cancer.

The androgen receptor (AR) plays an in important role in prostate carcinogenesis and is often mutated or overexpressed as the disease progresses to a hormone refractory state.[145] An androgen analog ^{18}F-fluoro-5α-dihydrotestosterone (^{18}F-FDHT) has been evaluated for imaging the AR in prostate tumors. In one study, ^{18}F-FDHT was shown to rapidly label tumors with

80% maximum tumor uptake observed at 10 min. and provided better imaging of certain metastatic lesions than ^{18}F-FDG.[146] In another study, 10 out of 15 patients with advanced disease displayed efficient tumor imaging with ^{18}F-FDHT. These 10 patients were treated with flutamide and the mean tumor-to-muscle ratio achieved with ^{18}F-FDHT dropped from 6.7 ± 4.1 to 3.0 ± 1.7, suggesting that the probe may be used to assess therapeutic responses.[134]

Some prostate cancers overexpress gastrin-releasing peptide (GRP) receptors and the results of several studies suggest that bombesin, a neuropeptide with high affinity for GRP receptors, labeled with ^{64}Cu or ^{18}F compares favorably to ^{18}F-FDG for imaging prostate tumors.[147-149]

1.5C.3. ImmunoPET with iodine-124

Of the various PET imaging strategies, immuno-PET (using antibody-based probes) currently offers the highest binding specificity and affinity.[150] Unfortunately, the relatively long serum-half lives of intact antibodies do not allow for rapid imaging. As mentioned previously, removal of the Fc portion of an antibody increases the rate of blood-clearance and therefore, increases the rate at which the desired signal-to-background ratios can be achieved. Several different engineered antibody fragments have been developed to improve the pharmacokinetics of immuno-PET probes. Single-chain variable fragments (ScFvs) retain the binding specificity of full-length immunoglubulins (160 kDa)

and can be used to construct much smaller minibodies (80 kDa) or diabodies (55 kDa). Unbound diabodies can clear the blood in <2 hr. as their molecular weight is just below the threshold for first-pass renal clearance (~60 kDa).[150] Nonetheless, immuno-PET generally requires the use of "unconventional" PET radionuclides in order to match the biological half-life of the antibody (or antibody fragment) with the physical half-life of the isotope.

One unconventional radionuclide that has shown some of the most promising results in pre-clinical and clinical immuno-PET studies is iodine-124 (^{124}I).[151-153] ^{124}I has a half-life of 100.2 hr and is therefore compatible with any antibody-based construct that clears the circulation within several hours to several days. ^{124}I displays a more favorable biodistribution than ^{64}Cu which is retained in the liver and kidneys by copper-binding proteins. ^{124}I also allows for a variety of labeling methods. Using the Iodogen method, the antibodies are directly iodinated on tyrosines in the presence of an oxidizing agent (1,3,4,6-tetrachloro-3α,6α-diphenyl glycoluril).[154] Using the Bolton Hunter method, the antibodies are indirectly labeled through an acylating reagent (N-succinimidyl-3[4-hydroxyphenyl]propionate) that reacts preferentially with the side-chain amino group found on lysines.[155] Antibodies that bind internalizing cell-surface receptors are shuttled to endosomes and those labeled by the Bolton Hunter method are less subject to dehalogenation in the acidic organelles than those labeled by the Iodogen method.[156-157] One of the earliest studies

evaluating an ^{124}I for tumor imaging demonstrated that a ^{124}I-labeled rat monoclonal antibody that recognizes the external domain of human c-erbB-2 could be used to image MDA-MB-361 human breast carcinomas growing in mice.[158] Collingridge et al. used an anti-VEGF antibody iodinated by the Bolton Hunter method (^{124}I-SHPP-VG76e) to image HT1080-26.6 and HT1080-1/3C human fibrosarcoma xenografts. Uptake of ^{124}I-SHPP-VG76e was found to be 1.8-fold higher in the HT1080-26.6 tumors which are known to express higher levels of VEGF than HT1080-1/3C tumors.[157] ^{124}I-labeled anti-CEA minibodies were used to visualize CEA-positive LS174T human colorectal carcinomas and demonstrated a tumor-to-background ratio of 11:1 at 18 hrs post-administration.[159] ^{124}I-C6.5, a diabody that recognizes the HER2 receptor tyrosine kinase, demonstrated clear delineation of MDA-MB-361 tumors growing in mice by 48 hrs. Biodistribution analysis showed that 1.1% of the injected dose localized to the tumor, whereas only 0.26% and 0.05% were retained in the liver and muscle respectively.[156] In a different study, an anti-HER2 affibody was labeled with ^{124}I using *p*-iodobenzoate as a linker (^{124}I-PIB-$Z_{HER2:342}$). ^{124}I-PIB-$Z_{HER2:342}$ imaged NCI-N87 human stomach carcinoma xenografts and was shown to provide better tumor contrast at a faster rate than a full-length anti-HER2 antibody (^{124}I-PIB-trastuzumab).[160] A monoclonal antibody that binds anti-Thomsen-Friedenreich antigen (TF-Ag) was labeled with ^{124}I and used to image 4T1 murine mammary tumors.[161] Tijink et al. used an iodinated a human

monoclonal antibody fragment directed against extra domain B of fibronectin (^{124}I-L19-SIP) to image FaDu hypopharyngeal carcinomas growing in mice. The authors were able to detect tumors as small as 50 mm^3 and achieved tumor-to-blood ratios as high as 46:1 by 72 hrs.[162] ^{124}I has recently become more commercially available and therefore has received renewed interest as a clinical imaging agent.[150] In one clinical study, 26 patients with renal masses were injected with an antibody specific for carbonic-anhydrase-IX (^{124}I-cG250) which is overexpressed in clear-cell renal carcinomas. The patients were imaged 1 week later and approximately 3 hr prior to surgical resection by laparatomy. ^{124}I-cG250 successfully identified 15/16 tumors using a tumor-to-healthy-kidney ratio of >3:1 as a threshold. The remaining 9 non-clear-cell renal masses were negative for the probe.[163]

There are several characteristics of ^{124}I that may impede its translation to the clinic. ^{124}I has a relatively low positron yield (23%) and suffers from low inherent resolution from the higher energy and longer range of the positrons that are emitted. In addition, quantitation of ^{124}I signals is difficult due to a complex decay scheme in which gamma rays are emitted in cascade with those generated from the annihilation of emitted positrons.[164] Some of these problems may be overcome with improved instrumentation and analytic software and the data generated to date suggest immuno-PET with ^{124}I-labeled probes warrant further study.

CHAPTER 2

NEAR-INFRARED OPITCAL IMAGING OF EXPOSED PHOSPHATIDYLSERINE IN A MOUSE GLIOMA MODEL

Introduction

Molecular imaging can provide useful information for drug development, patient stratification and assessing response to therapy [165-166]. Successful cancer imaging requires imaging probes that recognize cancer-specific markers with great specificity and sensitivity. Cell surface-exposed PS is an attractive target for molecular imaging. PS is strictly located to the inner leaflet of the plasma membrane bilayer in most normal cell types, including the vascular endothelium. Loss of PS asymmetry occurs during apoptosis and necrosis, resulting in the exposure of PS on the external surface of the cells [167-168]. Much interest has been roused in developing molecular imaging probes that bind to the exposed PS in order to noninvasively monitor the response of patients' tumors to various treatments from the induction of tumor apoptosis. Annexin V (A5) is the PS binding ligand that is most widely used for this purpose. Various radiotracers have been conjugated to annexin V for PET or SPECT imaging in preclinical tumor models and cancer patients [169-170].

It has recently been observed that PS becomes exposed on the outer surface of viable (non-apoptotic) endothelial cells in tumor blood vessels, probably in response to oxidative stresses present in the tumor microenvironment [21, 171]. Vascular

endothelium in normal tissues does not have exposed PS. Thus, in addition to imaging apoptotic tumor cells, PS binding probes also image the exposed PS on tumor vasculature. We have developed a series of monoclonal antibodies that recognize PS with higher specificity than does annexin V [88, 171]. The antibodies recognize PS complexed with the PS-binding protein, β2-glycoprotein I (β2GP1). The murine antibodies 2aG4 and 3G4 localize to PS-positive blood vessels in multiple tumor models. The antibodies then induce monocytes to bind to the tumor vasculature and destroy it by antibody-dependent cellular cytotoxicity, leading to tumor growth inhibition [22, 24]. Antitumor effects are enhanced by chemotherapy [25], radiation [23] and hormone-deprivation therapy [90], all of which increase PS exposure in the tumors, and amplify the target for attack by the antibodies. Bavituximab, a chimeric monoclonal anti-PS antibody, is in advanced clinical trials in patients with lung and breast cancer [172-173].

In the present study, we used a new, fully human PS-targeting antibody, 1N11. This antibody is similar to bavituximab in that it requires β2GP1 for binding to PS. To detect PS, we conjugated the $F(ab')_2$ fragment of 1N11 with a NIR dye, IRDye800CW, and used it together with optical imaging to study PS exposure on subcutaneous or orthotopic U87 gliomas in athymic mice. Optical imaging is an inexpensive and rapid technique that allows real-time measurements to be made of PS exposure *in vivo*. NIR dyes have advantages over visible fluorophores in that they use excitation and emission wavelengths in the NIR range. NIR light penetrates tissues more deeply than visible

light and causes minimal autofluorescence. The NIR dyes therefore allow imaging of deep-seated orthotopic gliomas in the mouse brain [174-176]. To explore whether 800CW-1N11 could be used to monitor dynamic changes in levels of PS exposure, gliomas were imaged before and after irradiation. PS exposure was elevated by irradiation, with the maximal tumor to normal tissue ratio (TNR) being obtained 24 h after irradiation. Fluorescence microscopy revealed that irradiation induces PS exposure on both the vasculature and on the tumor cells themselves. Our findings suggest that 800CW-1N11 is a useful tool with which to study PS exposure in preclinical animal tumors. These experiments lay the foundation for further development of 1N11 as an imaging agent in the clinic.

Results

PS exposure on blood vessels and tumor cells in gliomas

An average of 27 ± 10 % of blood vessels in non-irradiated tumors had exposed PS on their endothelium, as judged by coincident staining of vessels by 1N11 and anti-CD31 (**Fig. 2.1A and 2.2**). Irradiation increased PS exposure on tumor vessels to 64 ± 6 % ($P < 0.001$; **Fig. 2.1A and 2.2**). In addition, irradiation induced PS exposure on the tumor cells themselves (**Fig. 2.1A**). The localization seen with 1N11 was antigen-specific since the negative control 800CW-Aurexis produced relatively little staining (**Fig. 2.1B and 2.2**).

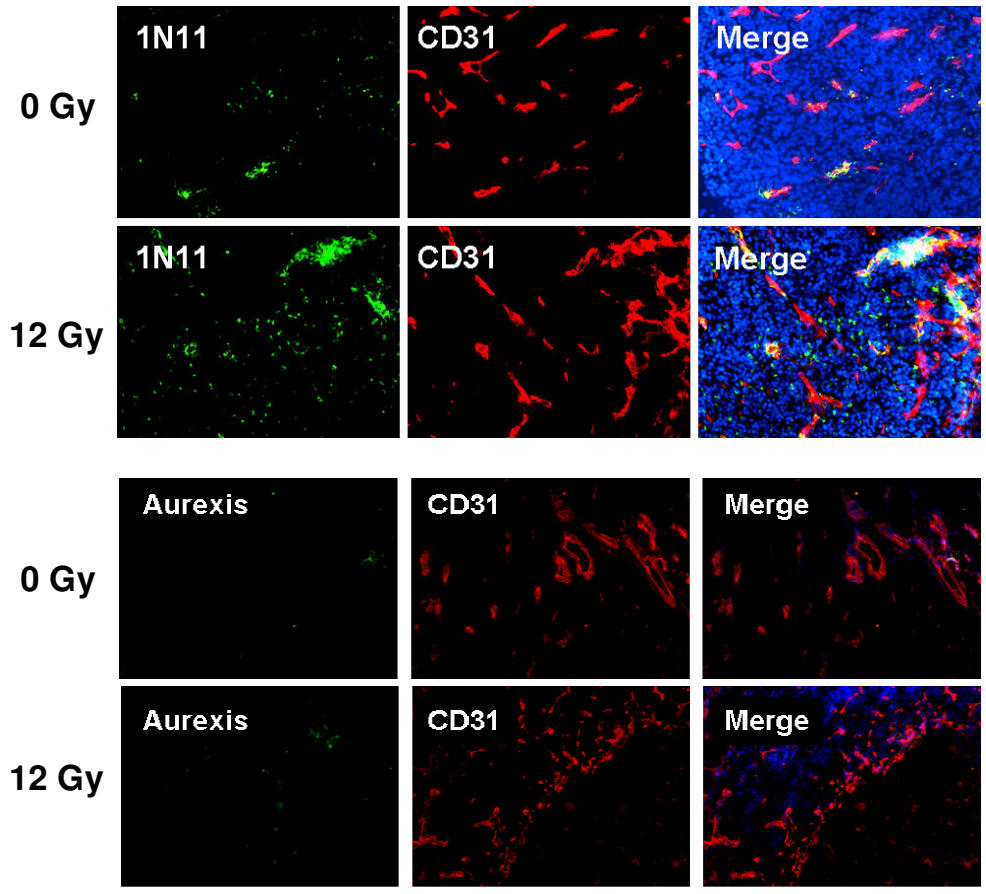

Figure 2.1 Immunohistochemical study of localization of 1N11 antibody in non-irradiated and irradiated tumors. Mice bearing a subcutaneous U87 glioma on each thigh received a single dose of 12 Gy irradiation to the left side tumor. Exposure of PS was determined 24 h later by i.v. injection of full length 1N11 or control antibody Aurexis. Animals were perfused with saline 3 h later. A) Frozen sections of both non-irradiated and irradiated tumors were analyzed for the presence of fluorescently labeled 1N11 (green). Vascular endothelial cells were counterstained with anti-CD31 (red). Merged images revealed coincidence of staining showing that 1N11 was bound to vascular endothelial cell in the non-irradiated tumor. Increased 1N11 staining was seen in the irradiated tumors and was due to increased staining of both endothelial cells and tumor cells**.** B) Tumor sections from control animals that had been injected with Aurexis were essentially unstained.

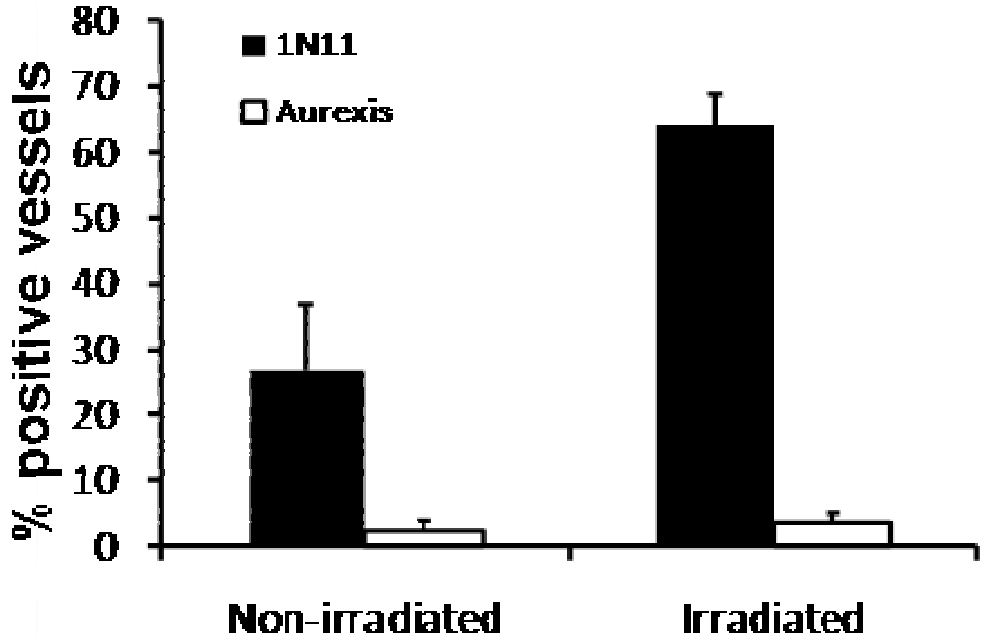

Figure 2.2. Quantification of IHC study of localization of 1N11 antibody in non-irradiated and irradiated tumors. Irradiation increased the percentage of PS-positive vessels from 27 ±10% to 64 ± 6% (P<0.001). Staining with 1N11 was antigen specific since Aurexis gave low levels of staining. (adopted from Zhao et al., 2011)

In vivo optical imaging of PS exposure in non-irradiated gliomas

800CW-1N11 localized with high selectivity to subcutaneous U87 tumors in mice. Clear contrast between the tumor and contralateral normal tissue was visible 24 h after injection and improved further by 48 h after injection (**Fig. 2.3**). Time course studies showed that the light intensity in the tumor and normal tissue was maximal 5 min after injection, and then decreased abruptly over the next 4 h. However, in contrast to

the fast wash out in normal tissues, the signal in the tumor was maintained over time. The TNR was 2.2 at 24 h and 2.5 at 48 h (**Fig. 2.4**).

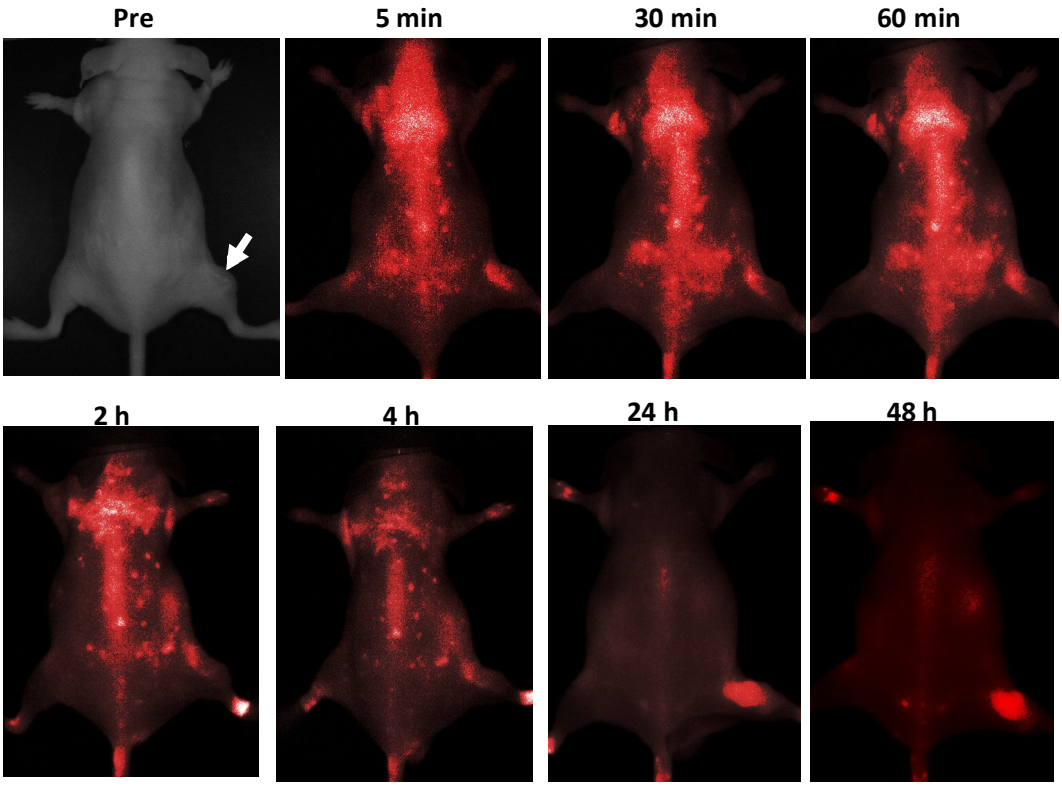

Fig. 2.3. In vivo NIR imaging of baseline level of PS in a subcutaneous glioma. A representative subcutaneous U87 glioma grown on the right thigh of a mouse (arrow). 800CW-1N11 was injected i.v. and optical imaging was performed at various time points thereafter. During the first 4 h, the images showed accumulation in the tumor area. However, by 24 h, the light signal remained only in the tumor and persisted there for at least 48 h after injection. (adopted from Zhao et al., 2011)

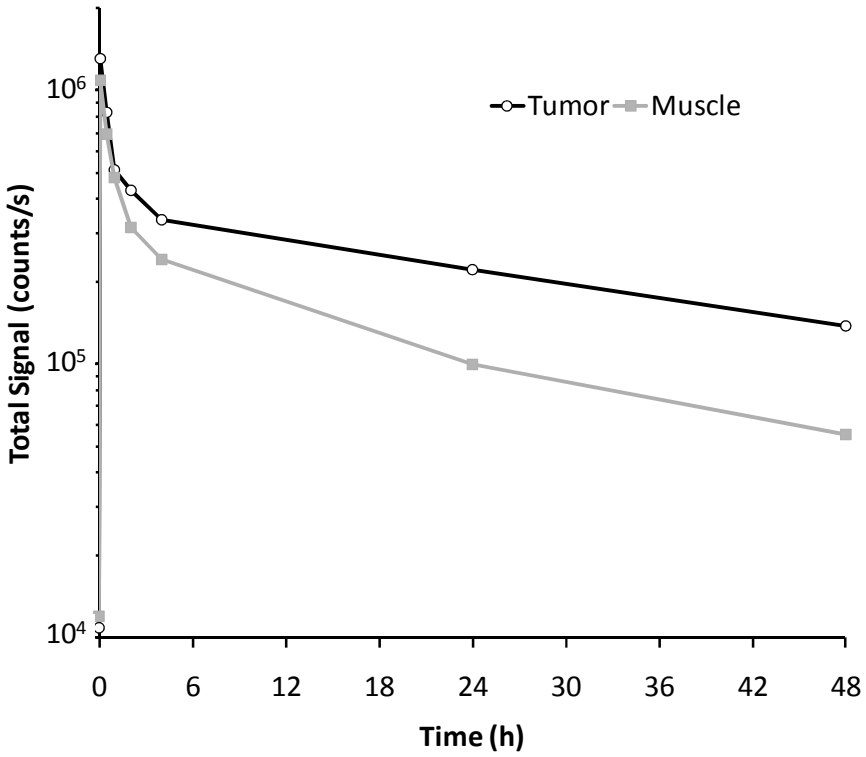

Figure 2.4. 800CW-1N11 clearance from tumor vs. muscle. Mean light intensity curves for the tumor (open circles) and the contralateral muscle (solid squares) revealed that 800CW-1N11 rapidly gave signals in both the tumor and the normal muscle but that the tumor signal persisted while the muscle signal washed out by 24 h. The tumor:muscle ratios were 2.2 at 24 h and 2.4 at 48 h. (adopted from Zhao et al., 2011)

Dynamics of PS exposure in response to radiation

A single dose of 12 Gy of irradiation was given to the left side tumor of mice carrying tumors on each thigh. 800CW-1N11 was injected 24 h later. As expected, the non-irradiated tumors on the right side gave similar results to those of mice with single tumors (**Fig. 2.3**) with a maximum TNR of 2.5 ± 0.5 being obtained 24 h after injection ($P < 0.05$**; Fig. 2.5 and 2.6**). Irradiation significantly enhanced tumor contrast. A TNR of

2.8 ± 1.1. was obtained 4 h after injection, rising to 4.0 ± 0.2 24 h after injection. The ratio of the TNR in the irradiated tumors to that in the non-irradiated tumors was 1.6 at 24 h after injection.

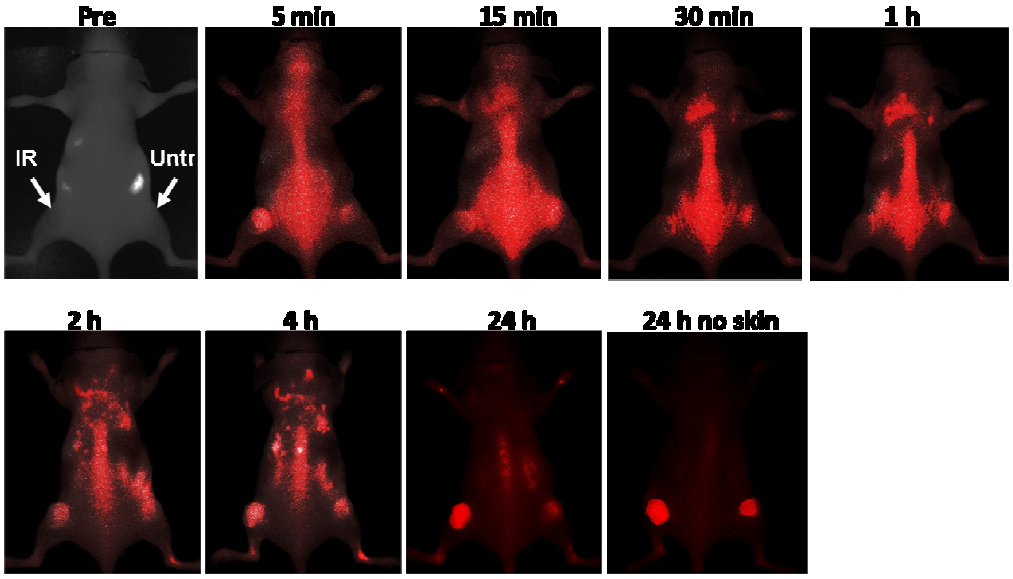

Figure 2.5. In vivo NIR imaging of PS exposure in gliomas before and after irradiation. Mouse bearing size-matched subcutaneous tumor on each thigh. A single dose of 12 Gy irradiation was delivered to the left side tumor. 24 h after radiation, 800CW-1N11 was injected via a tail vein and a series of *in vivo* fluorescence images was acquired at different time points. The contrast between the non-irradiated tumor on the right side and normal muscle increased over the 24 h period after injection to a TNR of 2.6. Irradiation of the tumor on the left side increased PS exposure to a TNR of 4.2. (adopted from Zhao et al., 2011)

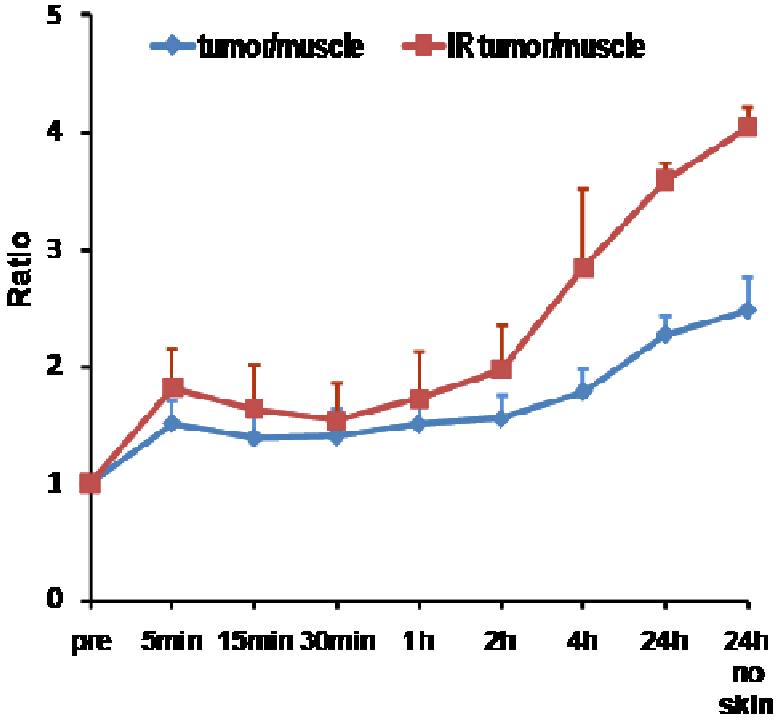

Figure 2.6 800CW-1N11 shows higher TNR in irradiated tumors. A time course study revealed that the maximal TNR of 2.5 was achieved at 24 h for non-irradiated tumors (n = 4; blue line), while an even higher TNR of 4.0 was obtained at 24 h for the irradiated tumors (n = 4; red line; $p < 0.05$). (adopted from Zhao et al., 2011)

Specificity of 800CW-1N11

The binding specificity of 800CW-1N11 was confirmed by comparing its localization pattern with that of the negative control 800CW-Aurexis. **Figure 2.7A** shows that 800CW-Aurexis entered both the irradiated and the non-irradiated tumors within 30 min of injection, but rapidly washed out. No significant contrast remained between either the irradiated or the non-irradiated tumors and normal tissues by 24 h (**Fig. 2.7B**). Furthermore, preadministration of unlabeled 1N11 before giving the 800CW-1N11 almost completely blocked localization of the 800CW-1N11 to both irradiated tumors and non-irradiated tumors (**Fig. 2.8**).

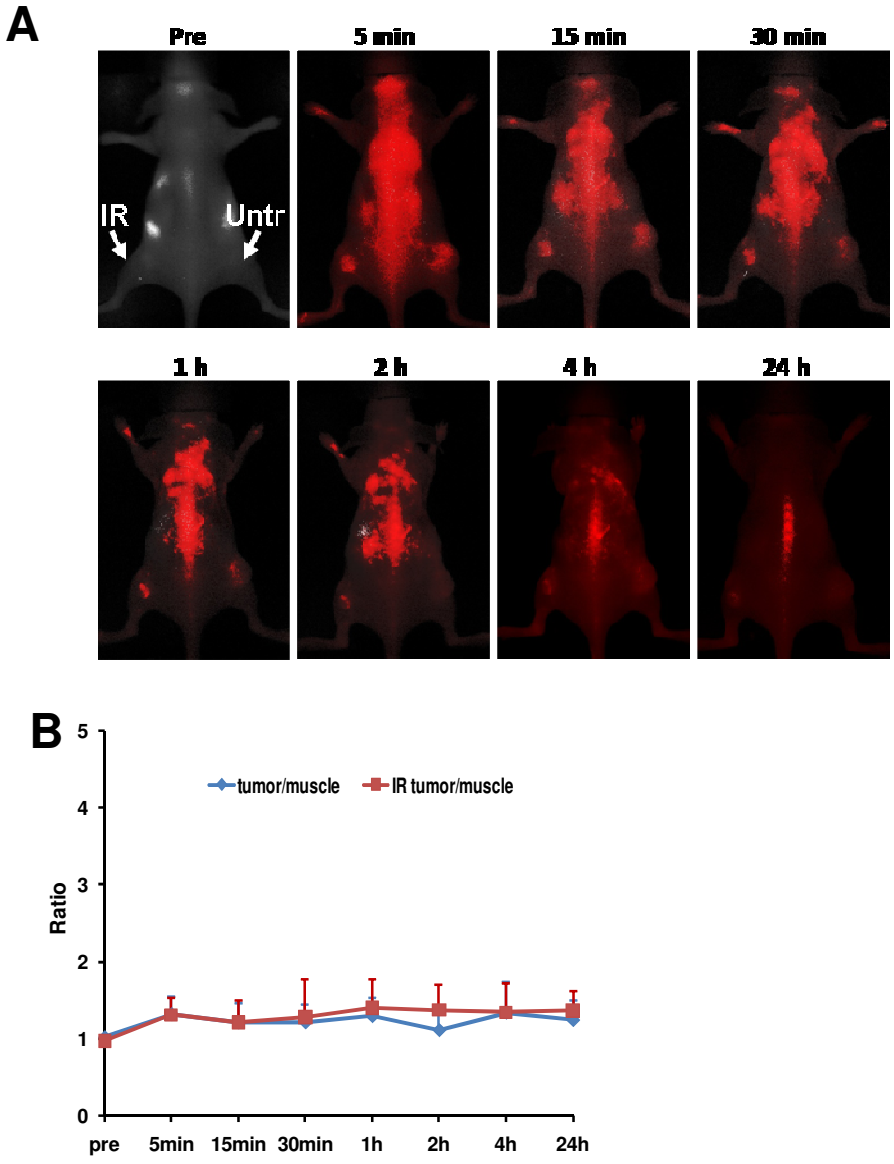

Figure 2.7. Specificity of 800CW-1N11 F(ab')$_2$ optical probe in vivo. To establish the antigen specificity of the 800CW-1N11 probe, a control probe 800CW-Aurexis was injected into the mice 24 h after irradiating one of the tumors in the flanks. A series of whole body images was acquired. A) The 800CW-Aurexis accumulated in both tumors during the first hour. However, both signals dimmed thereafter. There was no significant signal left in either tumor 24 h after injection. B) A time course study showed that 800CW-aurexis did not accumulate in either the non-irradiated tumors (n = 2) nor the irradiated tumors (n = 2). (adopted from Zhao et al., 2011)

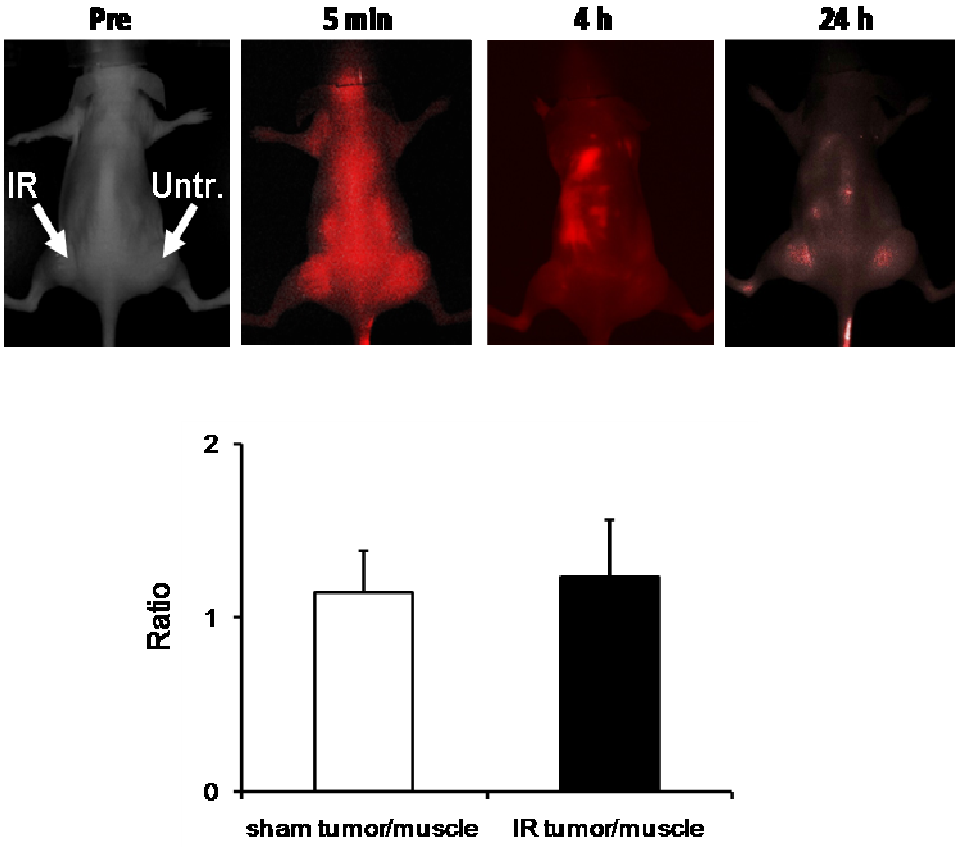

Figure 2.8. Pretreatment with unlabeled 1N11 blocks 800CW-1N11 tumor uptake. A competition study showed that preinjection of unlabeled 1N11 (2.5 mg/kg, i.v.) 4 h before imaging blocked 800CW-1N11 accumulation in both the irradiated tumor (left) and non-irradiated tumor (right). (adopted from Zhao et al., 2011)

In vivo optical imaging of PS exposure in orthotopic gliomas

800CW-1N11 successfully imaged U87 gliomas growing in the brains of mice, despite the light having to pass through the skull. Before optical imaging, MRI revealed that the mice had high signal intensity intracranial tumors on T_2-weighted images and ring-shaped contrast enhancement on T_1–weighted contrast enhanced images (**Fig. 2.9A**). A clear light signal that corresponded to the MRI image in location and size was obtained 24 h after injection of 800CW-1N11 (**Fig. 2.9B**). The signal approximately doubled after irradiation of the brain (**Fig. 2.10**). To confirm that the signal originated from the brain tumor, a surgical procedures was performed on anesthetized mice to reflect the scalp and remove the skull to expose the brain. A brighter and more focused light signal was emitted from the region of tumor growth (**Fig. 2.9B**). The tumor to normal brain ratio for irradiated tumors was 4.4 ± 0.4, as compared with 2.2 ± 0.6 for non-irradiated brain tumors (**Fig. 2.10**).

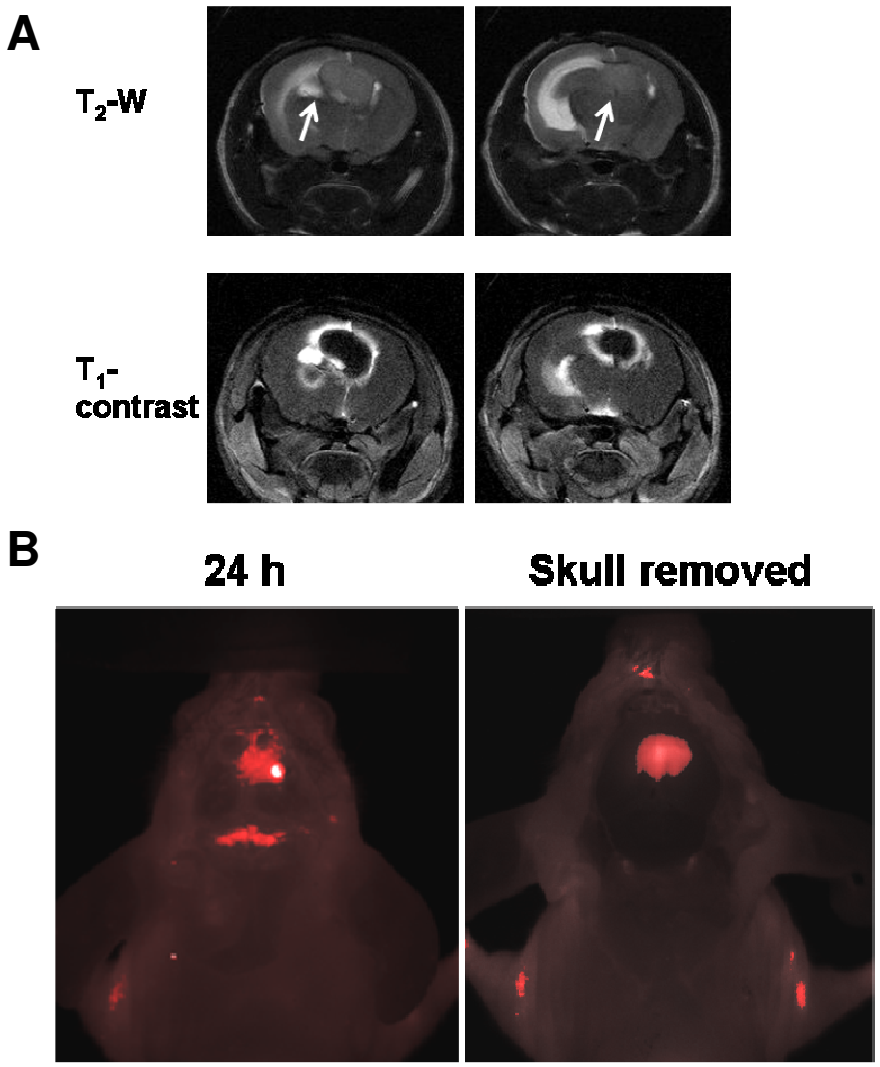

Fig. 2.9 In vivo optical imaging of PS exposure in orthotopic gliomas. A representative mouse bearing an orthotopic U87 glioma was irradiated with a single dose of 12 Gy to the whole brain using a D shaped collimator. A) Anatomic MRI revealed a 5 mm diameter intracranial lesion crossing the midline to invade the left side brain on the consecutive T_2-weighted slices. T_1-weighted contrast enhanced MRI showed the typical ring shaped enhancement in the tumor periphery. B) 800CW-1N11 was injected into the mouse 24 h after radiation and dynamic NIR optical imaging was performed. As with the subcutaneous tumors, maximal tumor contrast was achieved 24 h after injection. Removal of the skull increased the signal and subsequent dissection confirmed that the signal was from the tumor. (adopted from Zhao et al., 2011)

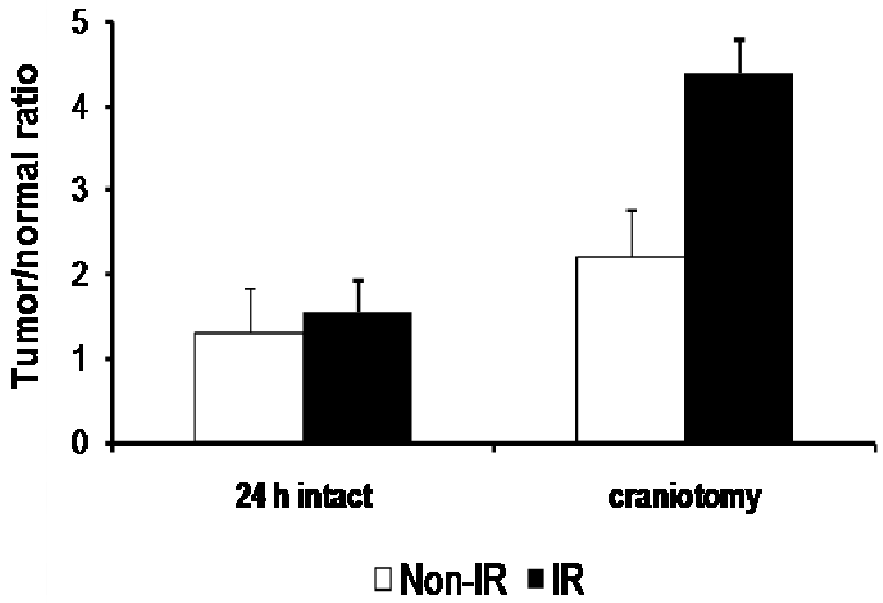

Figure 2.10. Quantification of 800CW-1N11 uptake in orthotopic U87 gliomas. The tumor versus contralateral normal brain ratio was 1.2 ± 0.6 for non-irradiated tumors and 1.5 ± 0.4 for irradiated tumors in the intact mouse brain 24 h after injection. After removal of the skull, the TNR of 4.4 ± 0.4 for irradiated tumors became significantly higher than the TNR of 2.3 ± 0.5 for non-irradiated tumors ($P<0.01$). (adopted from Zhao et al., 2011)

Near infrared fluorescence microscopy to detect 800CW-1N11 in tumors

A fluorescence microscope equipped with NIR filters was used to detect 800CW-1N11 in cryosections (7 μm) prepared from subcutaneous tumors 24 h after injection of 800CW-1N11. In good agreement with histological findings with unconjugated 1N11 (**Fig. 2.1**), merged images clearly showed that the 800CW-1N11 was binding essentially exclusively to vascular endothelial cells in non-irradiated tumors (**Fig. 2.11**). Irradiation increased the % of PS positive vessels and also induced PS exposure on the tumor cells themselves. Thus, the 800CW-1N11 signal in non-irradiated tumors derives from PS-positive vasculature, whereas the stronger signal in irradiated tumors derives from both PS-positive vasculature and tumor cells.

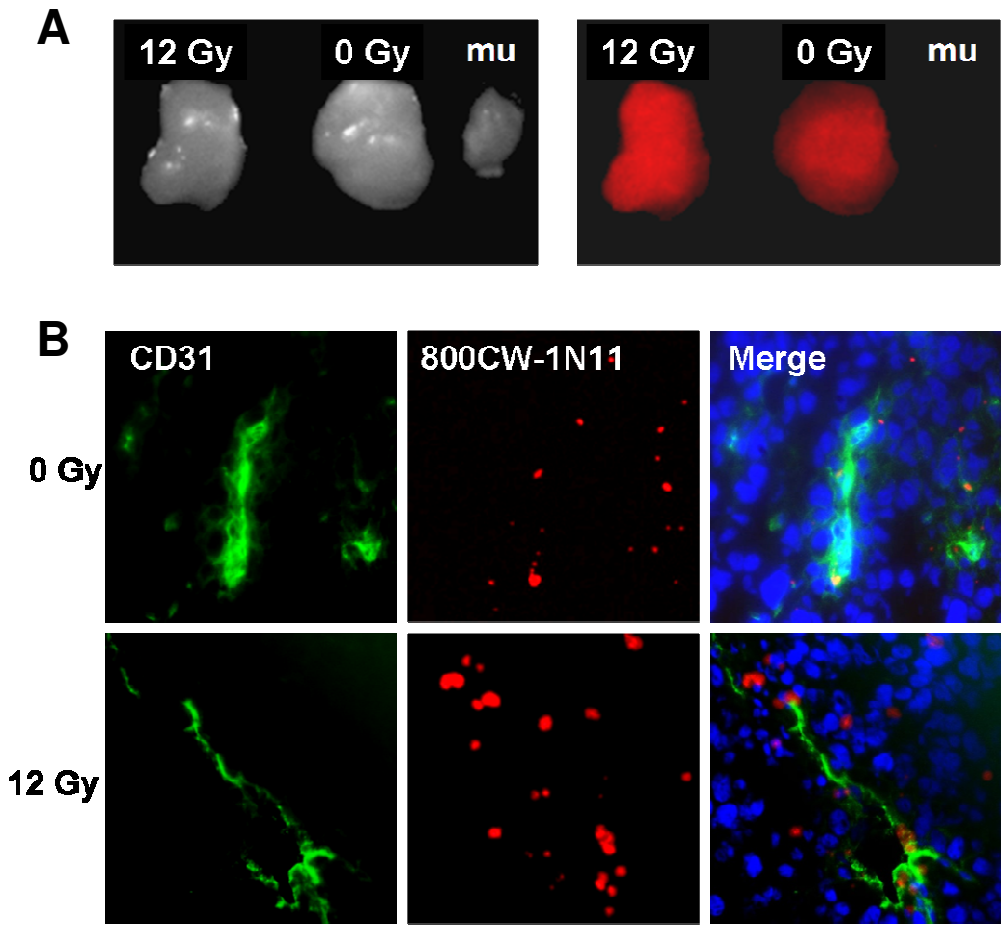

Fig. 2.11. NIR microscopy to detect of the location of the 800CW-1N11 optical probe in non-irradiated or irradiated gliomas. A) Mice bearing s.c. gliomas that had been irradiated (12 Gy) or sham-irradiated (0 gy) were injected with 800CW-1N11 24 h later. Irradiation increased the tumor signal, as above. The gliomas and contralateral muscle (mu) were excised. B) Sections of non-irradiated (top row) or irradiated U87 gliomas (bottom row) were examined for the presence of 800CW-1N11 (red), CD31 (green) or DAPI (blue). Vascular endothelial cells were detected by immunoflurescence staining with anti-CD31 (green). Nuclei were detected with DAPI (blue). NIR signals were detected with an infrared filter. The merged image shows that the 1N11 optical probe colocalized with tumor vascular endothelial cells in the non-irradiated tumor. In contrast, irradiation increased the NIR signal not only on the vascular endothelial cells but also on the tumor cells. (adopted from Zhao et al., 2011)

Discussion

We have demonstrated the feasibility of using 1N11 F(ab')$_2$ labeled with the NIR dye, 800CW, for optical imaging of PS exposure in both subcutaneous and orthotopic mouse models of U87 glioma. Baseline level of PS signals detected in non-irradiated gliomas by *in vivo* NIR imaging correlated with histological findings of endogenously exposed PS on tumor vascular endothelial cells. This is in a good agreement with previous studies performed in various tumor models [21-25, 88, 171]. Irradiation-induced PS exposure was successfully visualized by 800CW-1N11 optical imaging in mice. Fluorescence microscopy confirmed that both 1N11 and 800CW-1N11 localized more strongly to the irradiated tumors. The binding specificity of 1N11 was verified by competition experiments with unconjugated 1N11 and by the lack of staining with the irrelevant control 800CW-Aurexis.

Non-invasive molecular imaging of apoptosis is of great clinical interest as it would give an early indication of the responsiveness of a patient's tumor to therapy, allowing alterations in the therapy to be made if responses were not as good as expected [169-170, 177]. In the past several years, a great deal of effort has been made in developing such molecular imaging approaches. Radiolabeled and fluorescent annexin V preparations have been extensively tested in animal studies [73, 178-179]. More recently, clinical studies of PET or SPECT imaging with radiolabeled annexin V have shown that a higher uptake of annexin V by tumors during or after treatment correlates positively with a better prognosis in patients with breast, head and neck or lung cancer [59, 65, 180]. It is

important to note, however, that not all PS-expressing tumor cells in responding tumors are apoptotic. Hammill *et al* found that many of the cells that stain positively for annexin V are viable and can resume growth and reestablish phospholipid asymmetry once the therapy is discontinued. These results indicate that PS exposure, and thus loss of membrane asymmetry, precedes commitment to apoptotic death [181].

1N11, bavituximab and related murine monoclonal antibodies recognize PS and other anionic phospholipids in a β2GP1-dependent fashion. The antibodies have a more restricted specificity for PS than does annexin V, which recognizes PE in addition to PS and other anionic phospholipids [21, 182-183]. The high specificity of our antibodies for PS suggested their use for imaging tumor vasculature. We previously radiolabeled bavituximab with ^{74}As, which is a long-lived positron emitter having a radioactive half life of 17.8 days, and used it to image the vasculature of Dunning prostate R3227-AT1 tumors in rats. The long half life of ^{74}As allowed the intact antibody to reach its optimal target to background selectivity at 72 h without significant radioactive decay [26]. Tumor selective targeting was observed by PET imaging and a maximum of 22 tumor-to-liver ratio in rat tumors was achieved.

In the present study, we used the $F(ab')_2$ fragment of 1N11 for optical imaging to ensure its rapid clearance from the bloodstream and the achievement of high tumor:background ratios by 24 h after injection. Since the target on vascular endothelial cells is directly accessible to the blood, 1N11 localizes rapidly to tumor vessels. 1N11 is not internalized to any significant extent by cells and so persists for 2-3 days on the

endothelial cell surface, giving plenty of time for the unbound 1N11 F(ab')$_2$ in the blood to be cleared. We found in the present study that 1N11 labels about 27% of the vessels in non-irradiated U87 gliomas. Different tumors vary in the percentage of their vessels that have exposed PS [21, 23-24, 26]. In Dunning R3227-AT1 prostate tumors, 40% of vessels have exposed PS [26]. In F98 gliomas, the percentage is only 11% [24]. PS exposure on viable endothelial cells is induced by hypoxia, acidity and other stresses known to be present in the tumor microenvironment [21]. Probably, differences in PS positivity in different tumors relates to the levels of oxidative stresses in the tumor microenvironment.

Irradiation of U87 tumors with 12 Gy increased the percentage of tumor vessels that had exposed PS from 27% to 64 %, and increased the TNR from 2.8 to 4.0. These findings accord with our earlier finding that irradiation of A549 NSCLC xenografts and F98 gliomas increase vascular expression of PS [23-24]. Endothelial cells in tumors are highly sensitive to irradiation and will expose PS after a little as 5 Gy. We have previously shown that endothelial cells in tumors irradiated with 5 Gy appear to remain viable. They remain morphologically intact and lack markers of apoptosis for several days [23]. In the present study, 12 Gy of irradiation also induced PS exposure on the tumor cells in U87 tumors, thus contributing to the increased localization of 800CW-1N11 in irradiated tumors. Further studies are needed to determine whether the PS-expressing tumor cells are apoptotic or not.

Optical imaging is increasingly being used in preclinical cancer research [184-185]. It is being used in particular to study cancer specific markers, drug pharmacokinetics, and to monitor drug effects in small animals [119, 174, 186]. The attraction of the technique is that it is inexpensive, simple to conduct, gives real-time results, and does not require the handling and disposal of radioactive isotopes. In the clinic, optical imaging by visualizing fluorescently labeled tumor cells has recently emerged as an attractive approach to facilitate identification of tumor margins or sentinel lymph node metastases [187-188]. Several prior studies have demonstrated *in vivo* optical imaging of apoptosis with Annexin V labeled with Cy5.5, a red excitable dye [73]. However, the NIR dye IRDye800CW appears to be superior to Cy5.5 for *in vivo* imaging [119]. NIR fluorescence has advantages over visible fluorophores, including deeper penetration into tissues due to lower tissue absorption and scattering of light, and minimal autofluorescence. Our previous study showed the feasibility of imaging deep-seated orthotopic glioma of a mouse model with IRDye800 labeled 2-deoxyglucose [175]. Here, we have demonstrated the ability of NIR optical imaging to detect PS translocation in both subcutaneous and orthotopic glioma model.

Other labels besides optical dyes should be considered for attachment to 1N11 $F(ab')_2$ fragments. What is particularly impressive about 1N11 as a targeting ligand is its high specificity, lack of uptake by the liver or any other organs, rapid acquisition by its vascular target, and its persistence on the vascular target for days. It is an excellent candidate, for example, for labeling with DOTA and ^{64}Cu for PET or ^{111}In for SPECT. It

should have applications not only in tumor imaging but also in the imaging of thrombi or sites of ischemia for cardiovascular investigations. It will also be interesting to combine 1N11 probes with functional MRI to correlate vascular perfusion or permeability with PS distribution.

In summary, we have combined NIR optical imaging with 1N11, a novel monoclonal anti-PS antibody, to monitor *in vivo* dynamics of PS exposure in glioma of mouse models. We show that irradiation increases the PS signal, suggesting that irradiation causes intratumoral changes that may predict response to therapy. The high tumor specificity demonstrated by1N11 in the present study underscore the prospects of using 1N11 and related antibodies to treat cancer in humans.

CHAPTER 3

PET IMAGING OF EXPOSED PHOSPHATIDYLSERINE IN A MOUSE PROSTATE CARCINOMA MODEL

Introduction

Phosphatidylserine (PS) is an attractive molecular target for new cancer imaging agents designed to improve disease diagnosis and therapeutic planning. PS is a membrane lipid that is not normally found on the surface of healthy, resting cells because transporters and cytoskeletal proteins sequester PS to the inner leaflet of the plasma membrane. [100, 189] When cells undergo apoptosis, PS redistributes to the outer membrane leaflet to serve as a cell-surface marker for phagocytic clearance. [190-191] However, oxidative stress within the tumor microenvironment can also cause PS to become externalized on non-apoptotic cells. ROS induced by low pH, inflammation, and hypoxia within tumors together with reactive tumor metabolites damage the cell membrane allowing an influx of extracellular Ca^{2+} and, at the same time, stimulate ceramide production by acid sphingomyelinase (aSMase). Ca^{2+} signaling to transporters combined with membrane phase transitions by ceramide leads to redistribution of PS to the cell surface.[7, 9, 36-37, 192] PS has been found to be one of the most specific markers of tumor endothelium and is constitutively exposed on many tumor cells.[21, 25, 100, 171]

Several PS-targeting strategies have been employed to image tumors and their response to apoptosis-inducing therapies. The most widely studied PS-binding probe is Annexin V, a 35.8 kDa protein that binds PS in a calcium-dependent manner. Annexin V radiolabeled with different positron emitting isotopes has been used for positron emission tomography (PET) imaging of tumors in different animal models.[66, 70, 193] Technetium-99m (^{99m}Tc) labeled Annexin V has been used for single photon emission computed tomography (SPECT) imaging in human patients and showed some prognostic value for head and neck cancer, late stage lung cancer, and lymphoma.[65, 194] The C2A domain of synaptotagmin I, which is known to bind PS and other anionic phospholipids, has been radiolabeled for both PET and SPECT imaging of lung carcinomas treated with paclitaxel.[79-80] Similarly, a 14-residue PS-binding peptide labeled with ^{99m}Tc has been shown to localize to melanomas treated with paclitaxel.[84] However, each of these probes display unfavorable pharmacokinetics resulting in a high background signals throughout the abdominal region and specifically the liver and kidneys. ApoSense probes that mimic γ-carboxyglutamic acid (Gla) and synthetic compounds that coordinate Zn^{2+} (e.g. zinc(II)-dipicolylamine) are low molecular weight PS-specific probes that may have more desirable pharmacokinetic properties.[85, 87] However, further characterization and optimization of these probes is required to evaluate their true potential for tumor imaging.

We have developed an anti-PS mouse chimeric monoclonal antibody known as bavituximab as a tumor vascular targeting agent. Bavituximab binds PS through an interaction with the serum protein β2-glycoprotein I (β2GP1) with higher specificity than Annexin V and higher affinity than the other aforementioned probes. Upon binding to PS exposed on tumor endothelium, bavituximab inhibits tumor growth by recruiting tumor killing (type M1) macrophages. Chemotherapy, radiation, and hormone-deprivation therapy all increase exposure of PS in tumors and the antibody shows highest efficacy when used concomitantly with these treatments. Bavituximab does not accumulate in normal tissues, exhibits minimal side effects, and is currently being studied in phase II clinical trials. In order to determine the antibody's potential use for tumor imaging, we labeled it with the positron emitting isotope ^{74}As ($t_{1/2}$=17.8 days) and injected it into rats bearing subcutaneous prostate tumors. Radiolabeled bavituximab clearly labeled the tumors, but optimal images were not obtained until 72 hrs after injection.[26]

In the present study, we used a new fully human PS-targeting antibody, referred to as 1N11, to image prostate tumors growing in mice. The Fc portion of 1N11 was enzymatically removed and the resulting $F(ab')_2$ fragment was labeled with iodine-124 (^{124}I). ^{124}I-1N11 $F(ab')_2$ efficiently labeled both subcutaneous and orthotopic PC3 prostate tumors. Optimal images were obtained at 48 hours post-injection and the probe showed low uptake in non-target organs including the

liver and kidneys. ^{124}I-1N11 F(ab')$_2$ has a favorable signal: background ratio compared to other tumor imaging agents and may be particularly useful for assessing response to therapy.

Results

Radio iodination does not affect 1N11 F(ab')$_2$ binding to PS.

The PS-binding antibody fragment 1N11 F(ab')$_2$ was directly labeled with radioactive iodine through endogenous tyrosines (**Figure 3.1A**). After purification, the products of the ^{124}I-1N11 F(ab')$_2$ labeling reaction were analyzed using a gel filtration column and all radioactivity eluted with fractions corresponding to intact F(ab')$_2$ (**Figure 3.1B**). Furthermore**,** 1N11 F(ab')$_2$ labeled with ^{125}I fully retained binding activity. It had approximately the same ability to compete with biotinylated 1N11 (1N11-LB) as unlabeled F(ab')$_2$ for binding to PS immobilized on plastic. A 10-fold excess of ^{125}I-1N11 F(ab')$_2$ or unlabeled F(ab')$_2$ inhibited 1N11-LB binding to PS by 55.5% and 57.3% respectively (**Figure 3.2A**). Radioiodination also did not affect the ability of 1N11 F(ab')$_2$ to detect PS exposed on the surface of cultured endothelial cells and prostate tumor cells. We have previously shown that PS becomes externalized on the surface of cultured endothelial cells within 24 hr of x-irradiation.[27, 100] Therefore, ABAE and PC3 cells were irradiated with 5 Gy to induce exposure of PS. ^{124}I-1N11 F(ab')$_2$ showed specific binding to both types of PS-positive cells (**Figure**

3.2B). ^{124}I-Aurexis F(ab')$_{2,}$ the isotype matched control, did not show significant binding to irradiated or non-irradiated cells.

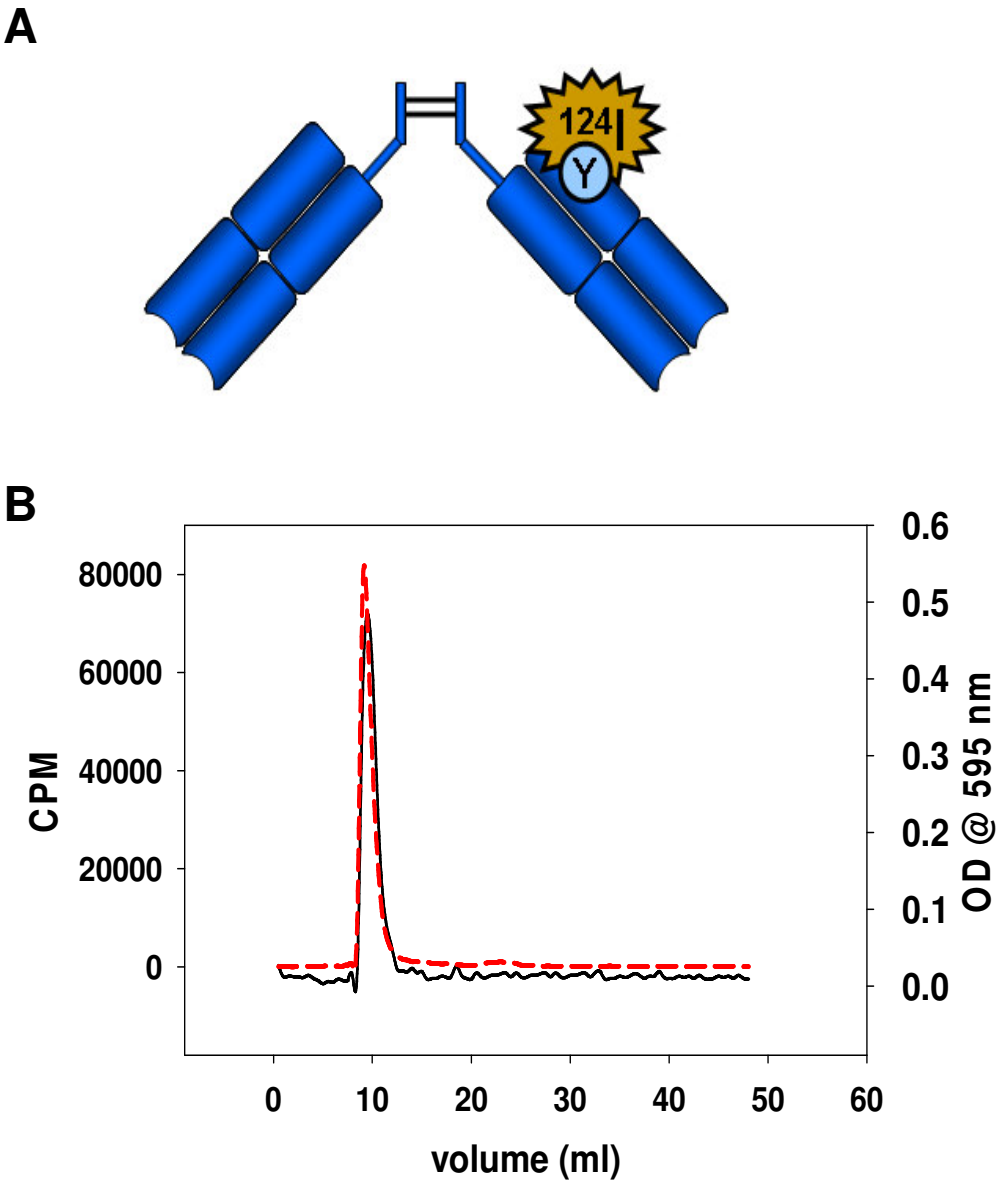

Figure 3.1. 1N11 F(ab')$_2$ is stable in PBS. A) Tyrosine residues in 1N11 F(ab')$_2$ were directly labeled with ^{124}I using the iodogen method. B) Gel filtration analysis demonstrated that radioactivity eluted with peak corresponding to intact F(ab')$_2$.

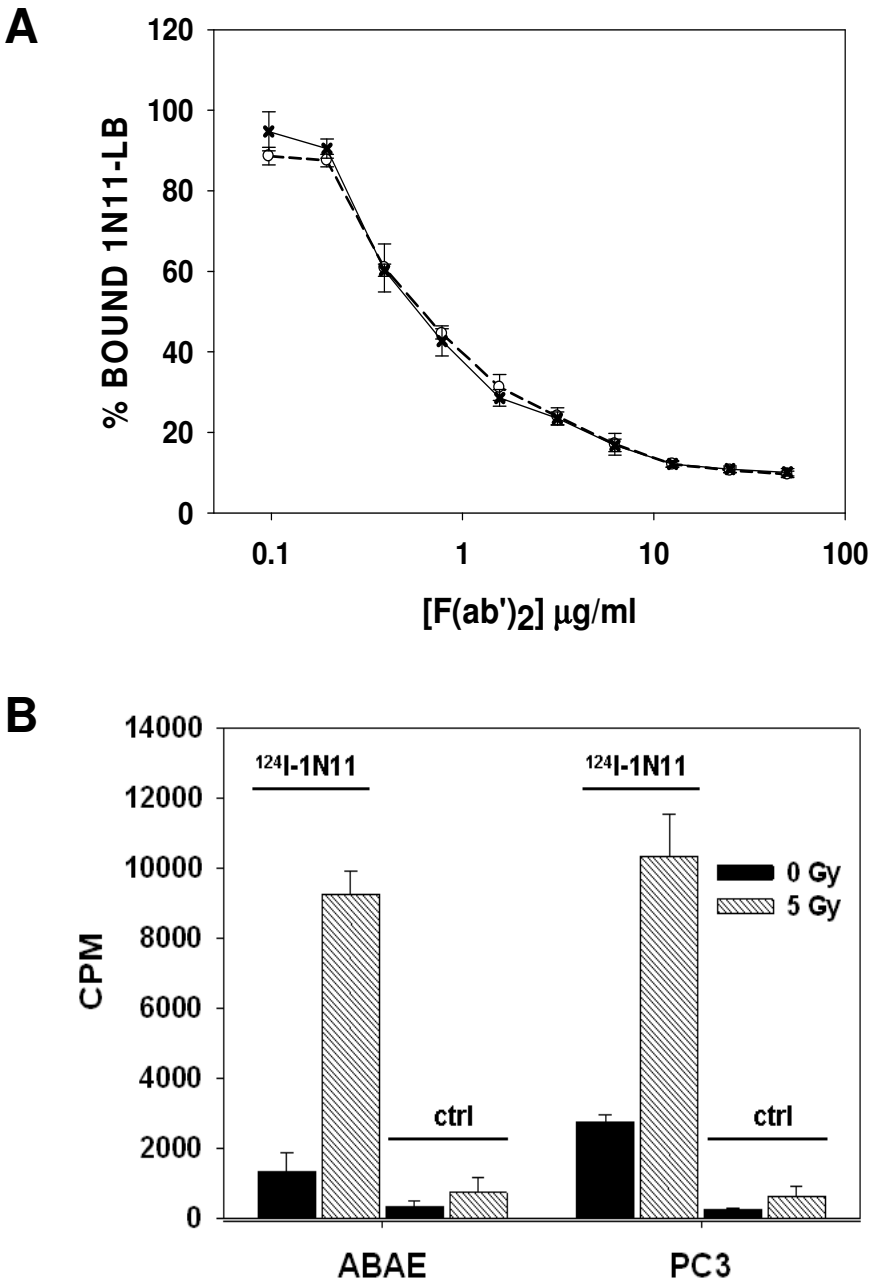

Figure 3.2. Radioiodination does not affect binding to PS. A) Competition ELISA showing 1N11 F(ab')$_2$ and ^{125}I-1N11 F(ab')$_2$ have same ability to compete with biotinylated 1N11 (1N11-LB) for PS. B) ^{124}I-1N11 F(ab')$_2$ bound specifically to PS exposed on the surface of irradiated EC and tumor cells.

^{124}I-1N11 F(ab')$_2$ is stable in vivo and binds serum β2GP1

Radioiodinated antibodies that bind cell-surface receptors can be internalized and dehalogenated by lysosomal proteolysis.[195] Therefore, serum collected from mice injected with ^{124}I-1N11 F(ab')$_2$ was analyzed by HPLC size exclusion chromatography to determine if ^{124}I-1N11 F(ab')$_2$ is also metabolized *in vivo*. At 48 hrs post-injection, there was no evidence of lower molecular weight ^{124}I-labeled degradation products or free ^{124}I in the circulation (**Figure 3.3A**). In fact, ^{124}I-1N11 F(ab')$_2$ ran at a higher molecular weight after injection into and recovery from mouse plasma. We hypothesized that the higher molecular weight was the result of ^{124}I-1N11 F(ab')$_2$ binding to serum β2GP1. In support of this hypothesis, full-length 1N11 antibody that had been injected into mice was found to co-immunoprecipitate with mouse β2GP1 (**Figure 3.3B**). Purified human β2GP1 (hβ2GP1) was used as a positive control and migrates slightly further than the mouse homolog during SDS-PAGE because it is less glycosylated (3 vs. 5 oligosaccharide side chains). Aurexis (ctrl) collected from mouse serum does not co-immunoprecipitate with β2GP1.

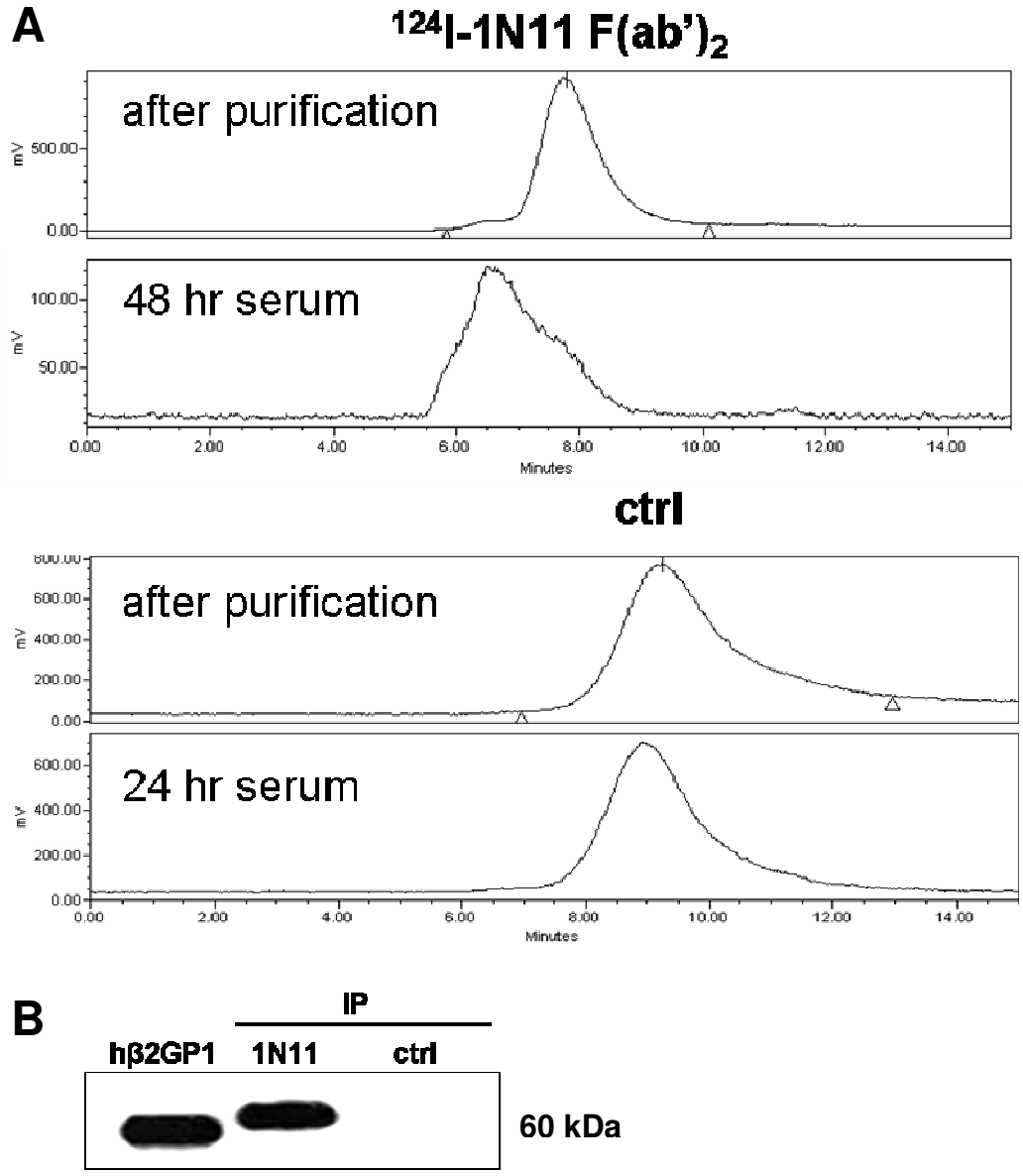

Figure 3.3 ^{124}I-1N11 F(ab')$_2$ is stable *in vivo* and binds serum β2GP1. A) HPLC analysis of serum from mice injected with ^{124}I-1N11 F(ab')$_2$ shows no evidence of dehalogenation or metabolic degradation of the probe at 48 hr. ^{124}I-Aurexis F(ab')$_2$ control also appears stable *in vivo*. B) W.Blot showing 1N11 co-immunoprecipitates with serum β2GP1 following systemic injection into mice. Aurexis (ctrl) collected from serum does not bind β2GP1.

1N11 F(ab')$_2$ biodistribution

To evaluate uptake of radioiodinated 1N11 F(ab')$_2$ in specific tissues, biodistribution studies were conducted in male athymic nu/nu mice bearing subcutaneous PC3 tumors. After 24 hr, ^{125}I-1N11 F(ab')$_2$ activity in the blood was measured at 6.7% ID/g (10.9% ID/organ) whereas uptake in all other tissues, including tumor, was <3% ID/g (<2% ID/organ) (**Figure 3.4**). The ^{125}I-Aurexis F(ab')$_2$ control displayed low uptake in all tissues with activity in the blood measured at only 0.2% ID/g (0.4%ID/organ) after 24 hr. After 48 hr, ^{124}I-1N11 F(ab')$_2$ activity was high in the tumor (1.1 %ID/g) and blood (1.4 %ID/g) relative to other tissues (**Figure 3.5**). The tumor:blood ratio was 0.8:1 whereas the tumor:liver ratio was 3.3:1.

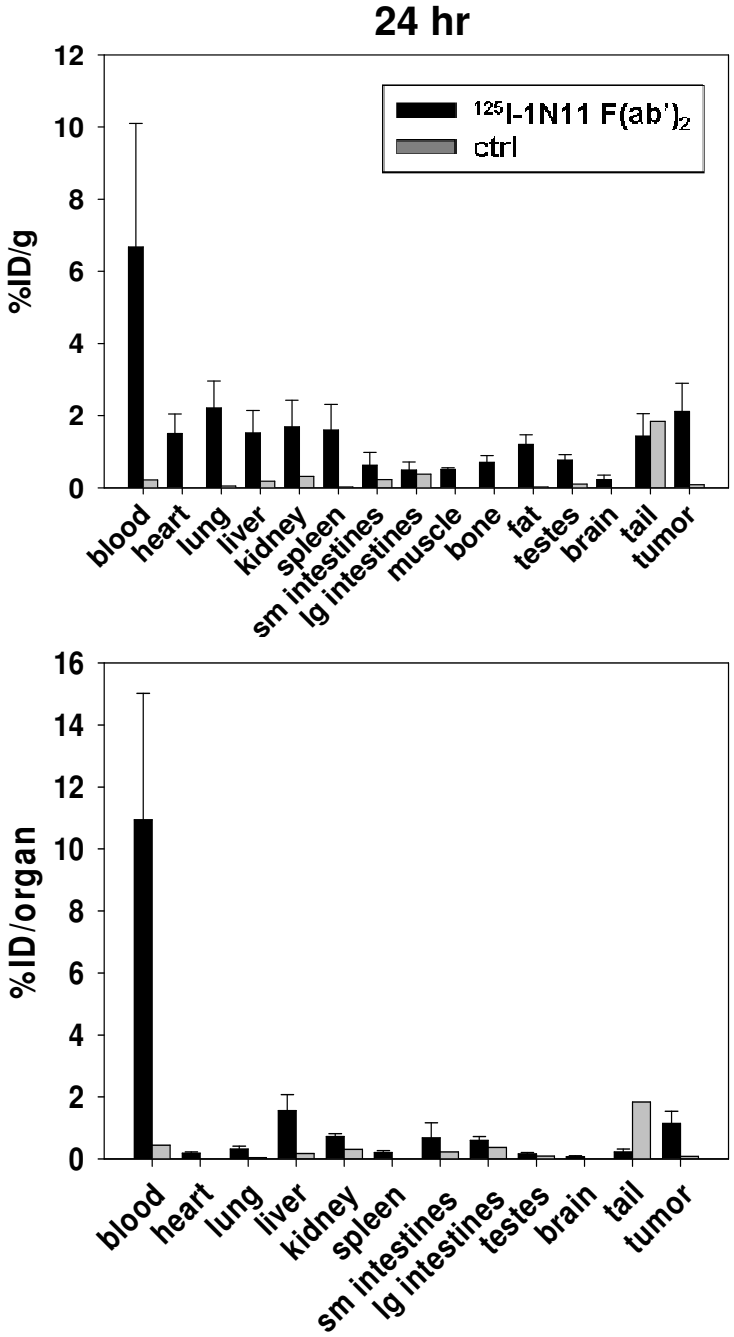

Figure 3.4. ^{125}I-1N11 F(ab')$_2$ biodistribution at 24 hr. 24 hr p.i., blood activity remains relatively high and tumor uptake of ^{125}I-1N11 F(ab')$_2$ is not higher than uptake in non-target organs. The ^{125}I-Aurexis F(ab')$_2$ control is almost completely cleared from the blood, organs, and tumor.

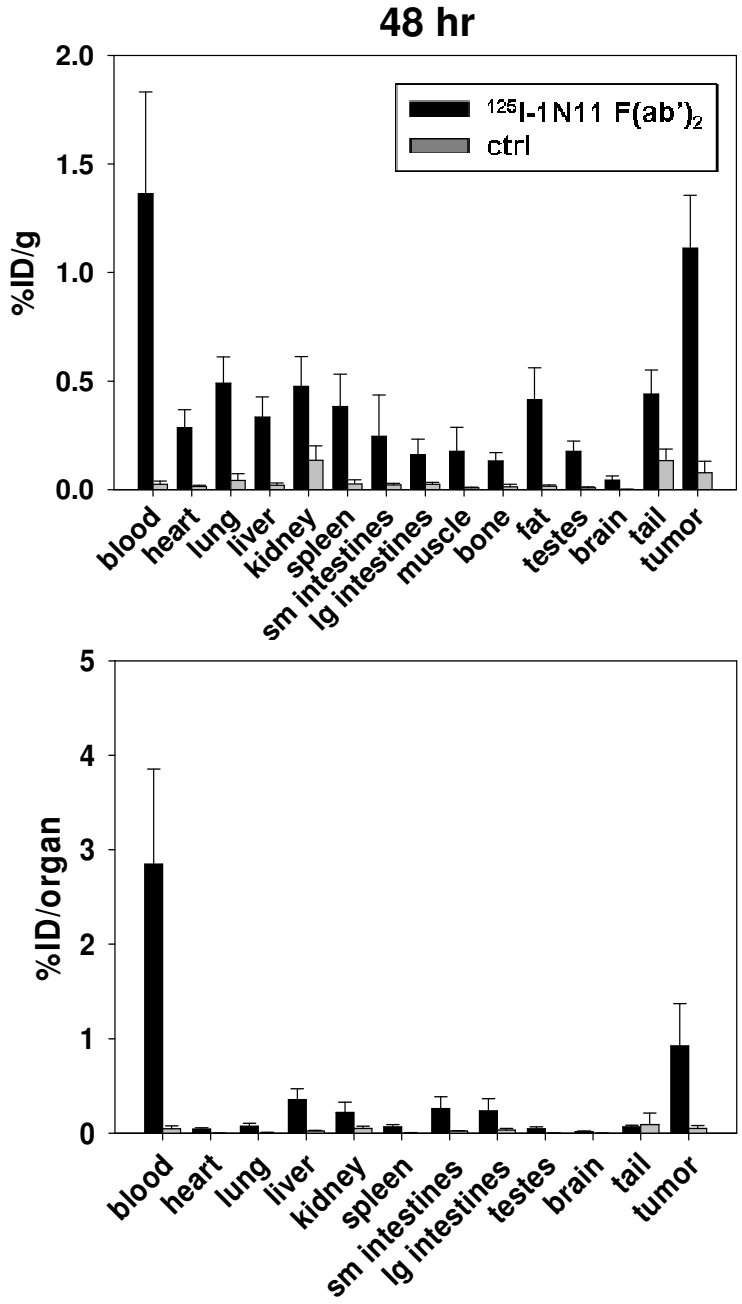

Figure 3.5. ^{125}I-1N11 F(ab')$_2$ biodistribution at 48 hr. 48 hr p.i., ^{124}I-1N11 F(ab')$_2$ activity was high in the tumor and blood relative to other tissues. The tumor:blood ratio was 0.8:1 whereas the tumor:liver ratio was 3.3:1.

MicroPET imaging of PC3 tumors with ^{124}I-1N11 F(ab')$_2$

Mice with subcutaneous PC3 tumors growing in their right flank were injected with ^{124}I-1N11 F(ab')$_2$ and imaged at 24 and 48 hr (**Figure 3.6**). Tumor-bearing mice injected with ^{124}I-Aurexis F(ab')$_2$ were used as negative controls. After 24 hr, the high background signal from normal tissues did not allow for specific imaging of the tumor. However, at 48 hr post-injection (p.i.) localization of ^{124}I-1N11 F(ab')$_2$ to the tumor provided sufficient tumor to background ratios to give clear delineation of the tumor. Quantitative analysis revealed that average tumor uptake was approximately 1.2% ID/g, thus correlating closely with the biodistribution studies performed with ^{125}I-1N11 F(ab')$_2$. Average uptake in the heart, liver and muscle was quantified as 0.9, 0.7, and 0.2 %ID/g respectively.

^{124}I-1N11 F(ab')$_2$ also successfully imaged PC3 tumors growing in the mouse prostate (**Figure 3.7).** Average tumor uptake of ^{124}I-1N11 F(ab')$_2$ 48 hr after injection. was 1.6% ID/g and the signal correlated to the approximate size and location of the tumors as determined by bioluminescence imaging (BLI). ^{124}I-Aurexis F(ab')$_2$ did not label either subcutaneous or orthotopic PC3 tumors.

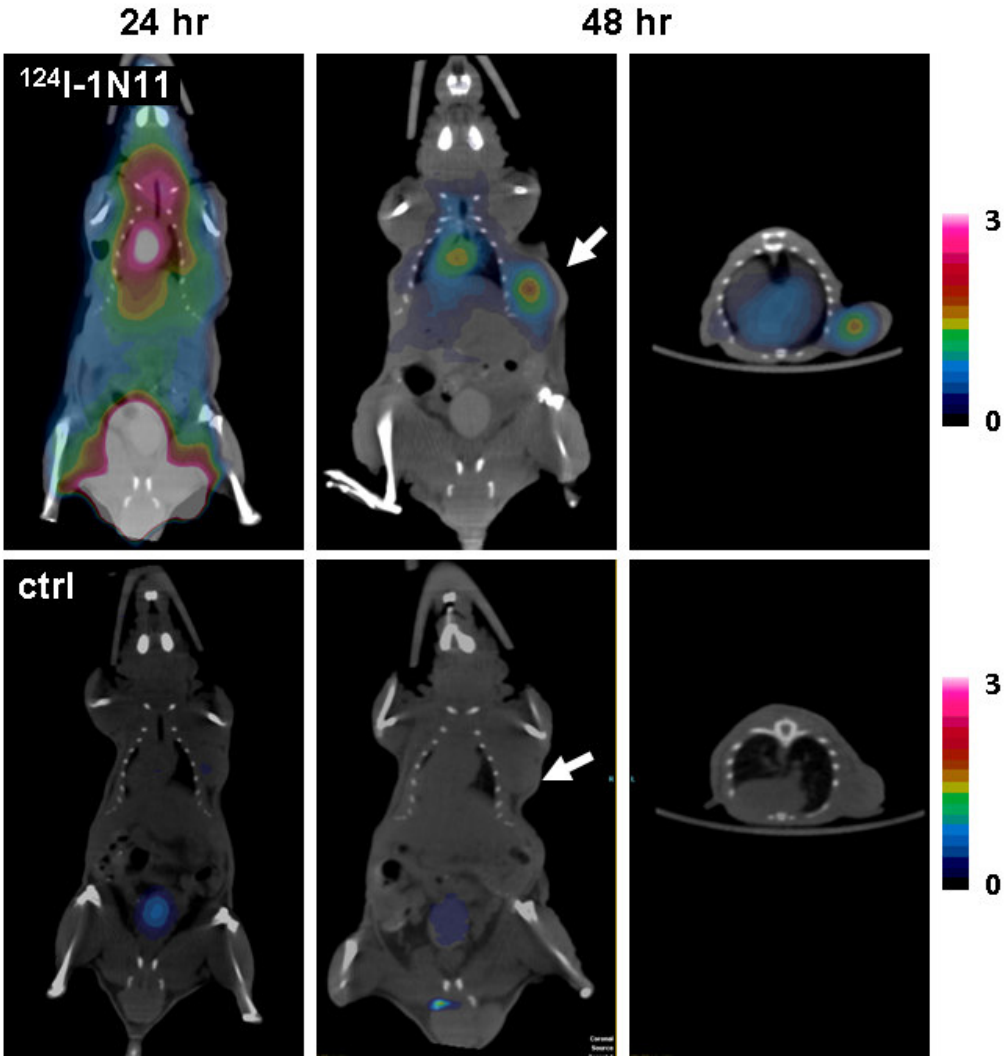

Figure 3.6. PET imaging of subcutaneous PC3 tumors with ^{124}I-1N11 F(ab')$_2$. At 48 hr p.i., subcutaneous PC3 tumors (arrow) were clearly delineated by ^{124}I-1N11 F(ab')$_2$. Signal in heart is from blood pool. Signal from the bladder was subtracted during image analysis. ^{124}I-Aurexis F(ab')$_2$ (ctrl) did not label tumors.

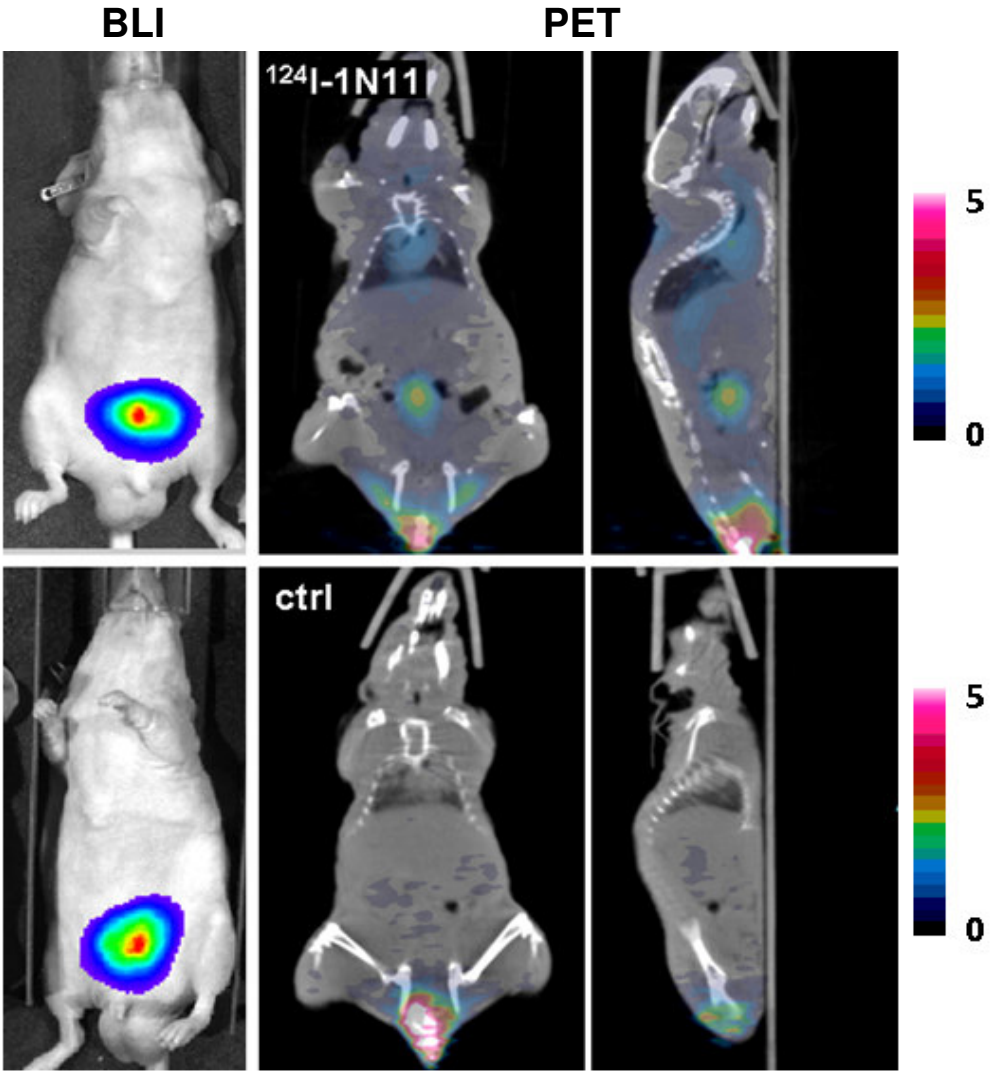

Figure 3.7. PET imaging of orthotopic PC3 tumors with ^{124}I-1N11 F(ab')$_2$. At 48 hr p.i., ^{124}I-1N11 F(ab')$_2$ successfully imaged PC3 tumors growing in the mouse prostate. The PET signal correlated to the approximate size and location of the tumors as determined by bioluminescence imaging (BLI). ^{124}I-Aurexis F(ab')$_2$ (ctrl) did not label orthotopic PC3 tumors.

Discussion

The present study demonstrates that the PS-binding antibody fragment 1N11 F(ab')$_2$ can be labeled with iodine-124 and used for PET imaging of prostate tumors growing in mice. The stability, affinity, and biodistribution of ^{124}I-1N11 F(ab')$_2$ compares favorably with PS-targeting probes previously studied for tumor imaging such as annexin V and C2A domains[56, 79, 196-197].

We used the iodogen method to oxidize iodine-124 to a positively charged reactive species that directly labels tyrosine residues in 1N11 F(ab')$_2$ through electrophilic substitution. Subsequently, several different assays were performed to verify that the antibody fragment retained both its structural and functional integrity following the radioiodination reaction. Chromatographic analysis of the reaction products did not provide any evidence of lower molecular weight ^{124}I-labeled peptides suggesting that neither the reaction with ^{124}I nor exposure to the oxidizing agent caused degradation of the F(ab')$_2$. Furthermore, radioiodination did not appear to have a significant affect on 1N11 F(ab')$_2$ binding to PS *in vitro*. Radioiodinated 1N11 F(ab')$_2$ efficiently detected PS both immobilized on plastic and exposed on irradiated cells grown in culture. Although the variable regions (Fv) in 1N11 contain 14 tyrosine residues with 5 in the light chain (V_L) and 9 in the heavy chain (V_H), none are present within the Complementary Determining Regions (CDRs). Nonetheless, Glaser et al. demonstrated that, annexin V directly iodinated using chloramine T reagent showed decreased binding to apoptotic

leukemia cells compared to annexin V indirectly labeled with Bolton-Hunter reagent (N-succinimidyl-3[^{124}I]-iodobenzene) [69]. The Bolton-Hunter method labels proteins through lysine residues instead of tyrosine and future studies will be aimed at determining if this method is superior to the Iodogen method for labeling 1N11 F(ab')$_2$. Antibodies iodinated by the Bolton-Hunter method have been reported to have higher *in vivo* stability and be less subject to dehalogenation than those directly iodinated through tyrosine.[153, 195, 197] This is less of a concern for 1N11 F(ab')$_2$ bound to exposed PS on tumor endothelial cells is not internalized. Also, we observed no evidence of dehalogenation or degradation of ^{124}I-1N11 F(ab')$_2$ in the serum of the mice examined in this study.

Biodistribution studies were conducted in tumor-bearing mice in order to determine the optimal pharmacokinetic parameters for PET imaging. We found that the optimal biodistribution was achieved by mixing radiolabeled 1N11 F(ab')$_2$ in a 1:10 ratio with unlabeled 1N11 F(ab')$_2$ with a total of 50 µg F(ab')$_2$ injected into each mouse. Tumor uptake (%ID/g) and the tumor-to-background ratio were significantly lower in mice injected with 5 µg ^{125}I-1N11 F(ab')$_2$ alone (data not shown). The higher total F(ab')$_2$ concentration achieved by supplementing radiolabeled F(ab')$_2$ with unlabeled F(ab')$_2$ may decrease the clearance rate of the radiolabeled F(ab')$_2$ and therefore allow for higher concentrations and retention of the probe at the target site.

Full-length 1N11 was enzymatically cleaved to allow for a more rapid clearance of unbound probe after i.v. injection. The 1N11 F(ab')$_2$ lacks a constant region (Fc) and cannot interact with neonatal Fc receptors (FcRn) on normal vascular EC that rescue IgG from early endosomes and return them to the bloodstream. [94-96] Wahl et al. were the first to show that radiolabeled anti-carcinoembryonic antigen (CEA) F(ab')$_2$ injected into hamsters cleared the circulation approximately 70% faster than full length anti-CEA IgG. [97] However, activity in the circulation of mice injected with ^{125}I-1N11 F(ab')$_2$ at 24 hr (7% ID/g) and 48 hr (1%ID/g) was significantly higher than in mice injected with the control ^{125}I-Aurexis F(ab')$_2$ at 24 hr (0.4% ID/g) and 48 hr (0.0% ID/g). The comparatively prolonged serum half-life of ^{125}I-1N11 F(ab')$_2$ can be explained by binding to circulating β2GP1. Although the normal physiological function of β2GP1 has yet to be defined, it has been shown to be the molecular target for autoantibodies responsible for antiphospholipid syndrome (APS).[198-200] β2GP1 is related to complement control proteins and consists of five Sushi domains. Domains I-IV are regular repeats of approximately 60 amino acids while domain V has 82 amino acids, including clusters of positively charged and hydrophobic amino acids that function in binding to PS.[88-89] Domain I interacts with domain V and β2GP1 normally exists in a closed loop conformation while circulating in the plasma. APS autoantibodies recognize cryptic epitopes in domain I and can only recognize β2GP1 when it unfolds to bind anionic surfaces.

APS antibodies do not recognize circulating β2GP1.[93] 1N11 also binds to β2GP1 domain I, but unlike APS antibodies, our data show that it recognizes the closed loop conformation of β2GP1 found in plasma and thus is not of the class of antibodies that cause APS.

The high binding specificity and high affinity possessed by 1N11 F(ab')$_2$ are ideal properties for a molecular imaging agent. However, the retention of radiolabeled 1N11 F(ab')$_2$ in the blood due to its interaction with β2GP1 is less than ideal for tumor imaging. To achieve maximal tumor-to-background ratios within a short time period, a molecular imaging agent should rapidly home to its target and any unbound residue should rapidly clear the circulation. We have previously shown that prostate tumors growing in rats could be imaged within 72 hr using the full-length PS-targeting IgG, bavituximab [26]. Bavituximab was labeled with a positron emitting isotope of arsenic (arsenic-74;^{74}As) because its' long half-life ($T_{1/2}$ = 17.8 days) was compatible with the long serum half-life of the IgG**.** After 72 hrs, uptake of ^{74}As-bavituximab was 22-fold higher in the tumor than in the liver. In the present study, we have found that, despite binding to serum β2GP1, ^{124}I-1N11 F(ab')$_2$ allows for more rapid imaging of tumors than ^{74}As-bavituximab. Subcutaneous and orthotopic PC3 human prostate tumors growing in mice were clearly imaged by ^{124}I-1N11 F(ab')$_2$ at 48 hr. Activity in the blood of mice injected with radiolabeled 1N11 F(ab')$_2$ was approximately 19-fold lower than that measured in rats injected with full-length radiolabeled

bavituximab IgG (unpublished data). In most normal tissues, residual ^{124}I-1N11 F(ab')$_2$ in the blood did not cause high background signals, but pooling of blood in the heart and, to a lesser extent, the liver resulted in signals above background. Although activity from the blood pool did not interfere with the imaging of either the subcutaneous or orthotopic prostate tumor model, activity in the bladder due urinary excretion of unbound ^{124}I-1N11 F(ab')$_2$ did interfere with the imaging of orthotopic tumors. Previous studies have shown that the diuretic furosemide can be used to prevent ^{18}F-FDG accumulation in the bladder and enhance PET imaging of abdominopelvic tumors.[201-202] We found that treatment with furosemide 2 hr prior to imaging also ensured urinary washout of ^{124}I-1N11 F(ab')$_2$ and decreased the signal in the bladder to background levels.

Total tumor uptake of ^{124}I-1N11 F(ab')$_2$ was relatively low compared to other molecularly targeted tumor imaging probes. PS exposed on tumor EC may be less abundant than antigens overexpressed on the malignant cells that constitute the tumor parenchyma. Tumor EC constitute a minor fraction of the tumor cell population and not all tumor blood vessels are PS-positive. We were able to detect the small amount of exposed PS in tumors because uptake of ^{124}I-1N11 F(ab')$_2$ in non-target organs was exceedingly low. This is because PS externalization is highly specific to tumor endothelium, with virtually no PS found on the surface of normal endothelium. Unbound ^{124}I-1N11 F(ab')$_2$ lacks FcRn recognition is likely metabolized by cells in the kidney and elsewhere with

rapid clearance of the radioactive metabolites. The favorable pharmacokinetic properties of ^{124}I combined with improved commercial availability has led to increased interest in its clinical evaluation.[150] ^{124}I-labeled antibodies specific for carbonic-anhydrase-IX (^{124}I-cG250) and A33 antigen (^{124}I-huA33) have been shown to successfully image tumors in patients with clear-cell renal cancer and colorectal cancer respectively. [163, 203]

The most important clinical use for ^{124}I-1N11 F(ab')$_2$ to translate the clinic may not be for early diagnosis of cancer, but rather for assessing tumor response to therapy. PS externalized on apoptotic and necrotic tumor cells after anti-tumor therapy should result in increased ^{124}I-1N11 F(ab')$_2$ uptake in responding tumors. Future studies will be aimed at determining if increased uptake of ^{124}I-1N11 F(ab')$_2$ in tumors treated with chemotherapy, radiation therapy, and/or androgen deprivation therapy can be used to predict the effect of each therapy on tumor growth.

CHAPTER 4

INCREASED EXPOSURE OF PHOSPHATIDYLETHANOLAMINE ON THE SURFACE OF TUMOR VASCULAR ENDOTHELIUM MAY SERVE AS A TARGET FOR TUMOR IMAGING

Introduction

In normal cells, the aminophospholipids phosphatidylserine (PS) and phosphatidylethanolamine (PE) are asymmetrically distributed across the plasma membrane with essentially all the PS and the majority of the PE localized in the cell's inner membrane leaflet [100, 189]. This membrane lipid asymmetry is maintained by a group of P-type ATPases known as aminophospholipid translocases (APTLs) that catalyze the active transport of PS and PE from the external to the internal plasma membrane leaflet of the membrane [8]. Unlike normal cells, apoptotic cells and tumor cells lose their capacity to maintain PS asymmetry resulting in the appearance of the lipid in the cells' outer membrane leaflet. The expression of PS at the cell surface inhibits immune responsiveness and, in the case of apoptotic cells, also serves as a recognition ligand and binding site for phagocytes [190-191]. PE has also been shown to be exposed on apoptotic cells, but it has not been associated with a specific function [99].

Increases in intracellular [Ca^{2+}] as a result of transcriptional activation or exposure to environmental stress can also cause loss of membrane asymmetry. Influx of exogenous Ca^{2+} or Ca^{2+} released from intracellular stores inhibits APTLs and, at the same time, activates ATP-binding cassette (ABC) transporters and phospholipid scramblases (PLSRs) that randomize all membrane phospholipids between leaflets resulting in a complete loss in plasma membrane lipid asymmetry [9]-[204]. Environmental stress also activates sphingomyelinases (SMases) that cleave sphinogomyelin to ceramide [36, 192]. Ceramide destabilizes the bilayer, activates pro-apoptotic signaling pathways and promotes membrane blebbing [7, 37]. Thus, cellular stress and activation can promote the exposure of aminophospholipids on the cell surface through multiple pathways. Indeed, unlike quiescent normal endothelium, there is significant environmental stress imposed on the tumor endothelium by acidity, reactive oxygen species (ROS) and transient hypoxia that results in the redistribution of PS to the cell surface [31, 205-206]. Because both PS and PE are co-regulated by the same transporters, the expression of cell surface PS on tumor EC raises the possibility that PE is also expressed on the surface of tumor blood vessels.

Duramycin (M.W.=2013 Da) is a highly specific PE-binding peptide produced by the bacteria *Streptovercillium cinnamoneus* . Duramycin binds PE at a 1:1 molar ratio with a K_d of 4-6 nM, an unusually high affinity for a small, ligand-binding peptide [101]. Duramycin is the smallest polypeptide known to

have a defined 3-dimensional binding pocket and recognizes ethanolamine phospholipids with exclusive specificity [101] by fitting over the ethanolamine head group like a glove [207]. The hydrophobic binding pocket is stabilized by three internal thioether linkages that makes the peptide resistant to heat and proteolytic degradation [104]. Pharmacokinetic studies in rats have shown that duramycin is rapidly cleared from the blood stream with a serum half-life of < 4 min [106]. ^{99m}Tc-labeled duramycin binds to PE exposed on apoptotic and necrotic cells and has been used successfully for the *in vivo* imaging of acute myocardial infarction [106].

In this report, we used duramycin to show that PE becomes specifically exposed on the surface of tumor EC and that treatment of cultivated EC with known tumor-associated stresses causes the formation of PE-positive blebs on the cell membrane. *In vivo* studies revealed that labeled duramycin specifically localized to the vascular endothelium in multiple tumor types. Duramycin was also effective at imaging subcutaneous tumors. Taken together, these findings indicate that externalized PE may be a general marker of tumor vasculature and suggests that duramycin possesses the specificity and pharmacokinetic properties to make it an effective agent for specifically targeting the tumor vasculature with imaging agents and/or therapeutic drugs.

Results

Modification of duramycin to create the PE-binding probe DLB2

Duramycin with two biotin tags, one at the N-terminus and one at the adjacent lysine, was assayed as a PE-binding probe. This construct was named duramycin-L-biotin 2 (DLB2) (**Fig. 4.1**) and was produced by reacting duramycin with an excess of NHS-L-biotin. Lipid binding was assessed by ELISA. Figure 1 shows that DLB2 binds PE whereas the control peptide does not. The negative control used for duramycin has the same amino acid sequence as duramycin except that the lanthanides (thioether-containing amino acids) were substituted with alanines (**Fig. 4.2**). This peptide does not form a 3D binding pocket and was named "linear duramycin" (linDUR). LinDUR has 3 amino groups available for reaction and is referred to as linDLB following biotinylation and 800CW-DUR following conjugation to NIR dye.

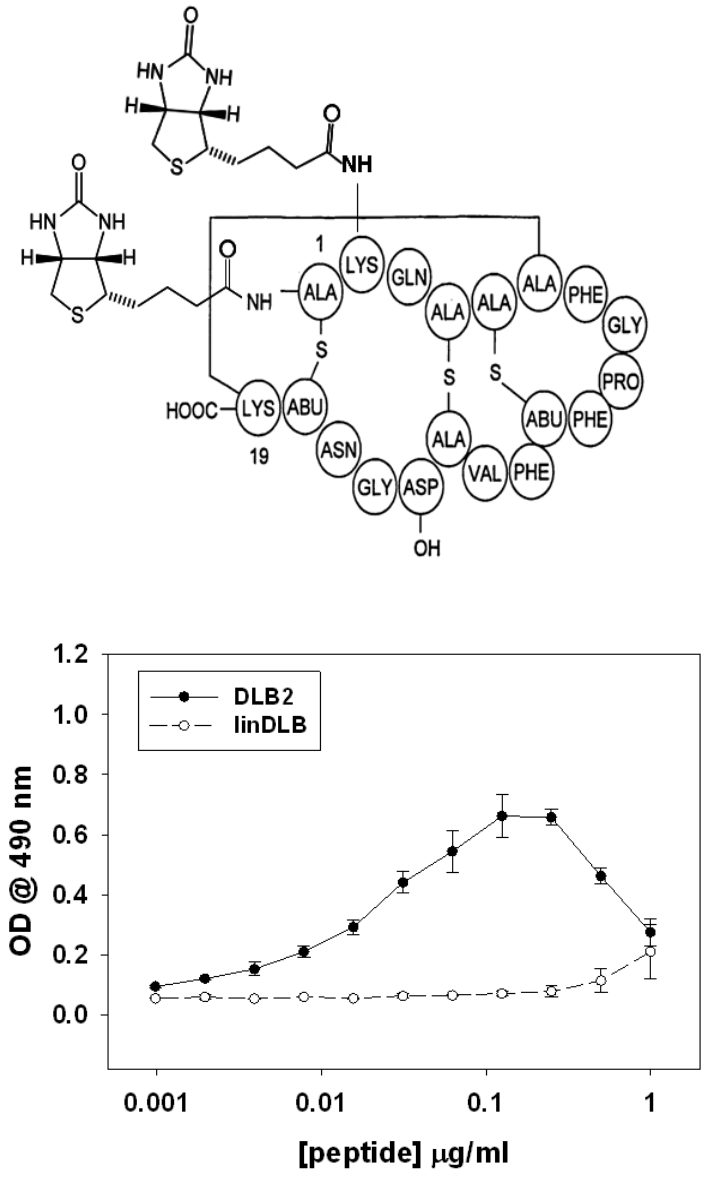

Figure 4.1. Duramycin-L-biotin 2 (DLB2) binds PE. Duramycin is biotinylated at both the N-terminus and adjacent lysine when reacted with $\geq$2 molar equivalents of NHS-L-biotin. DLB2 binds PE whereas the linear control peptide (linDLB) does not.

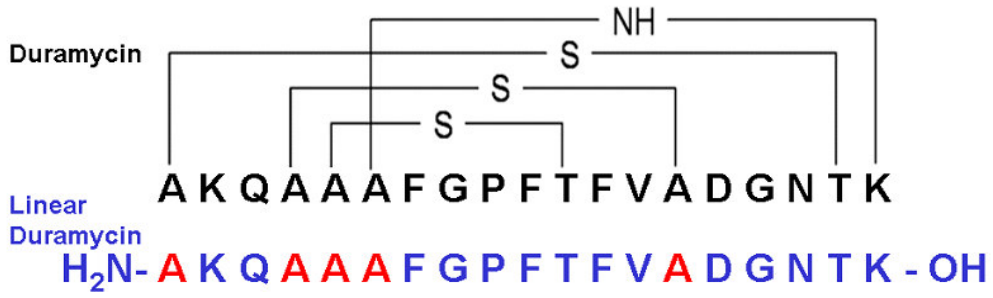

Figure 4.2. Control peptide sequence. The peptide used as a negative control for duramycin was named "linear duramycin" (linDUR). which has the same sequence as duramycin except that the lanthanides (thioether-containing amino acids) are replaced with alanine and does not form a 3-D binding pocket. This peptide has three amino groups available for reaction and is referred to as linDLB following biotinylation and 800CW-linDUR following conjugation to NIR dye.

Individual duramycin molecules form a complex

Competition ELISAs were performed in order to verify that DLB2 bound PE in the same manner as unmodified duramycin (DUR). Instead of competing with DLB2 for PE-binding sites as expected, unmodified duramycin (DUR) was found to enhance DLB2 binding to PE at molar ratios between 1:1 and 1:4 (DLB2:DUR) (**Fig. 4.3A**). DLB2 was also found to bind DUR immobilized on plastic in the absence of PE (Fig 3B). DLB2 did not bind linDUR nor did linDLB bind DUR. Different concentrations of DLB2 complexed with DUR (1:4) bound PE with a higher affinity than equivalent concentrations of DLB2 alone (**Fig. 4.3C**). These data led to the hypothesis that DLB2 and DUR are interacting to

form a pentameric PE-binding complex with one DLB2 peptide interacting with four DUR peptides (**Fig. 4.3D**). To test this hypothesis, duramycin and DLB2 were each analyzed by fast protein liquid chromatography (FPLC) using a size exclusion column. Neither peptide demonstrated aggregate formation in solution under physiological conditions (PBS, pH 7.2) (**Fig. 4.4**). DUR and DLB2 both yielded a single elution peak corresponding to monomeric peptide. However, DUR and DLB2 formed multimeric complexes in the presence of PE-containing membranes (**Fig. 4.5**). Interactions between peptides bound to different PE liposomes crosslinked the liposomes and caused them to from precipitates. DUR was more effective at precipitating PE liposomes than DLB2. A mixture of DLB2 and DUR showed similar crosslinking of liposomes to that seen with DUR alone.

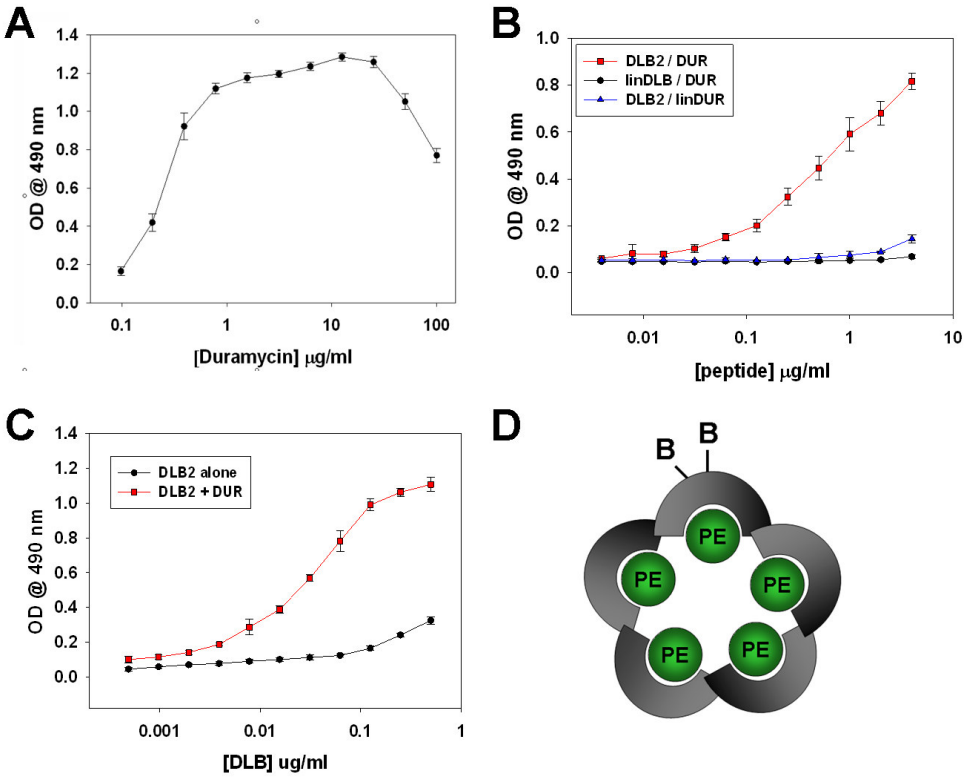

Figure 4.3. Individual duramycin molecules form a complex. (A) Competition ELISA ([DLB2]=0.1 μg/ml) demonstrating DUR/DLB2 mixtures with molar ratios ≤ 5:1 show enhanced binding to PE. (B) ELISA demonstrating DLB2 and DUR bind specifically to one another. (C) ELISA showing mixture of DLB2/DUR (1:4) binds PE with higher affinity than DLB2 alone. (D) Proposed model for pentameric PE-binding duramycin complex with one DLB2 peptide interacting with four unmodified duramycin peptides.

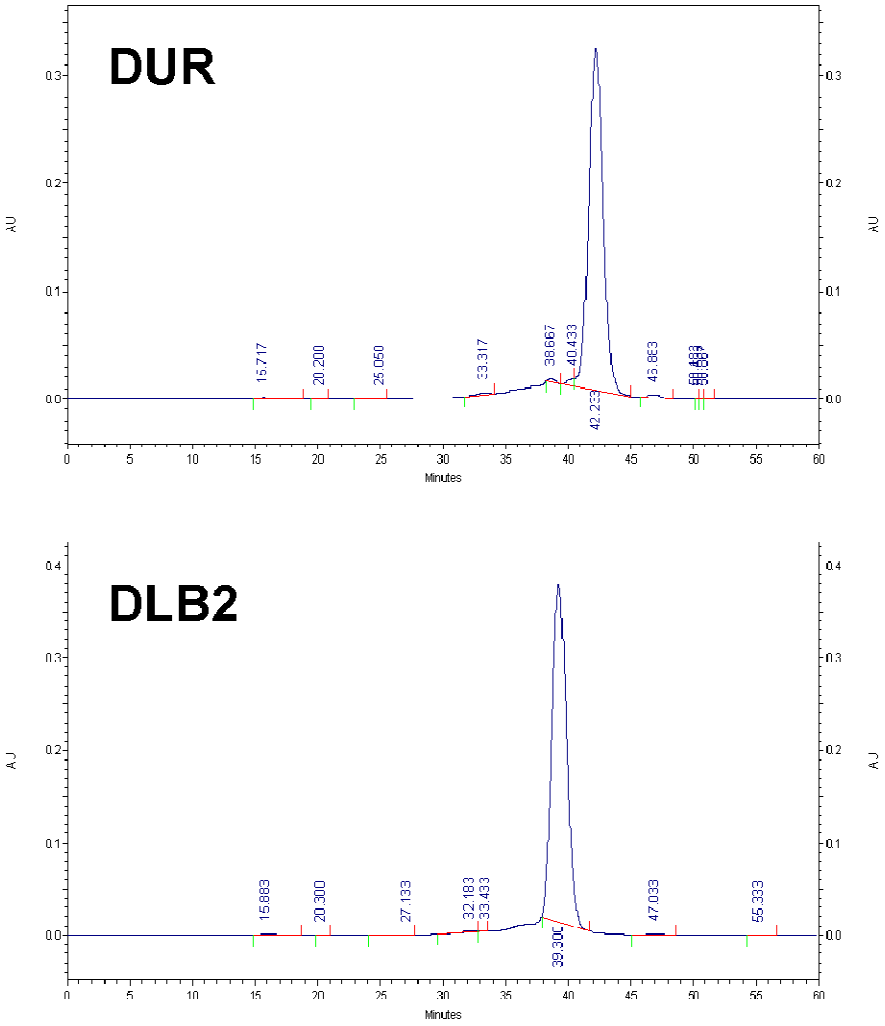

Figure 4.4. Duramycin does not form a complex in solution. Duramycin and DLB were each run on a Superdex 200 10/300 gel filtration column to determine their respective sizes in solution. Neither peptide demonstrated aggregate formation under physiological conditions (PBS, pH 7.2) with each having a single elution peak corresponding to monomeric peptide (DUR MW = 2,013 Da, DLB MW=2,352 Da).

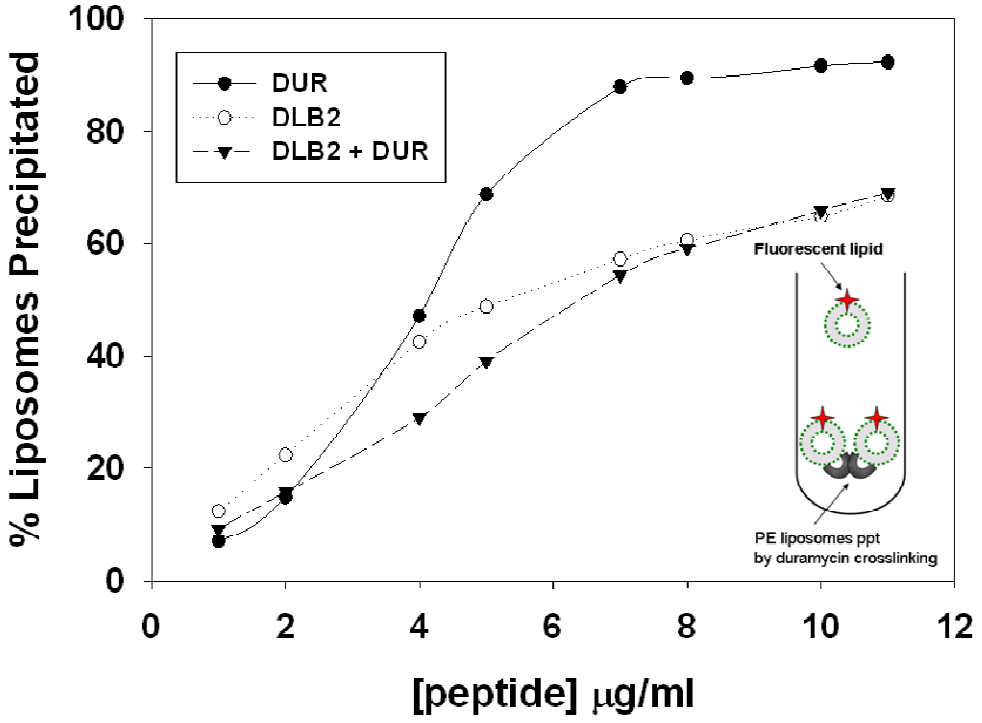

Figure 4.5. Formation of duramycin complexes requires interaction with PE-containing membranes. Interactions between duramycin peptides bound to different PE liposomes crosslinks the liposomes and causes them to form precipitates. DUR was more effective at precipitating PE liposomes than DLB2. A 1:1 mixture of DUR and DLB2 showed similar crosslinking to that seen with DUR alone.

Additional duramycin constructs

A duramycin dimer was constructed by conjugating two molecules of duramycin to one another using the tri-functional cross-linker tris-succinimidyl aminotriacetate (TSAT). The conjugation reaction left one amino group free for reaction with NHS-biotin and the resulting construct was referred to as D2TB. D2TB bound PE more efficiently than DLB2 (**Fig. 4.6**), but less efficiently than DLB2 complexed with DUR (data not shown). Duramycin was also conjugated to the metal ion chelators 1,4,7,10-tetraazacyclododecane-1,4,7,10-tetraacetic acid (DOTA) and 1,4,7-triazacyclononane-1,4,7-triacetate (NOTA). DOTA-duramycin had a single molecule of DOTA per molecule of duramycin and was labeled with copper-64 (^{64}Cu) or gallium-68 (^{68}Ga). NOTA(2)-duramycin had two molecules of NOTA per molecule of duramycin and was only labeled with ^{68}Ga. ^{64}Cu-labeled duramycin ([^{64}Cu]DOTA-DUR) bound specifically to PE immobilized on plastic (**Fig. 4.7**). [^{64}Cu]DOTA-DUR did not bind PC (data not shown). Addition of unmodified duramycin did not enhance [^{64}Cu]DOTA-DUR binding to PE. [^{68}Ga]DOTA-duramycin bound PE more efficiently than [^{68}Ga]NOTA(2)-DUR. Addition of unmodified duramycin did not enhance binding of [^{68}Ga]DOTA-duramycin, but did enhance binding of [^{68}Ga]NOTA(2)-DUR. These data suggest that duramycin constructs with a single modification bind PE more efficiently than duramycin constructs with modifications at both the N-terminus and the adjacent lysine.

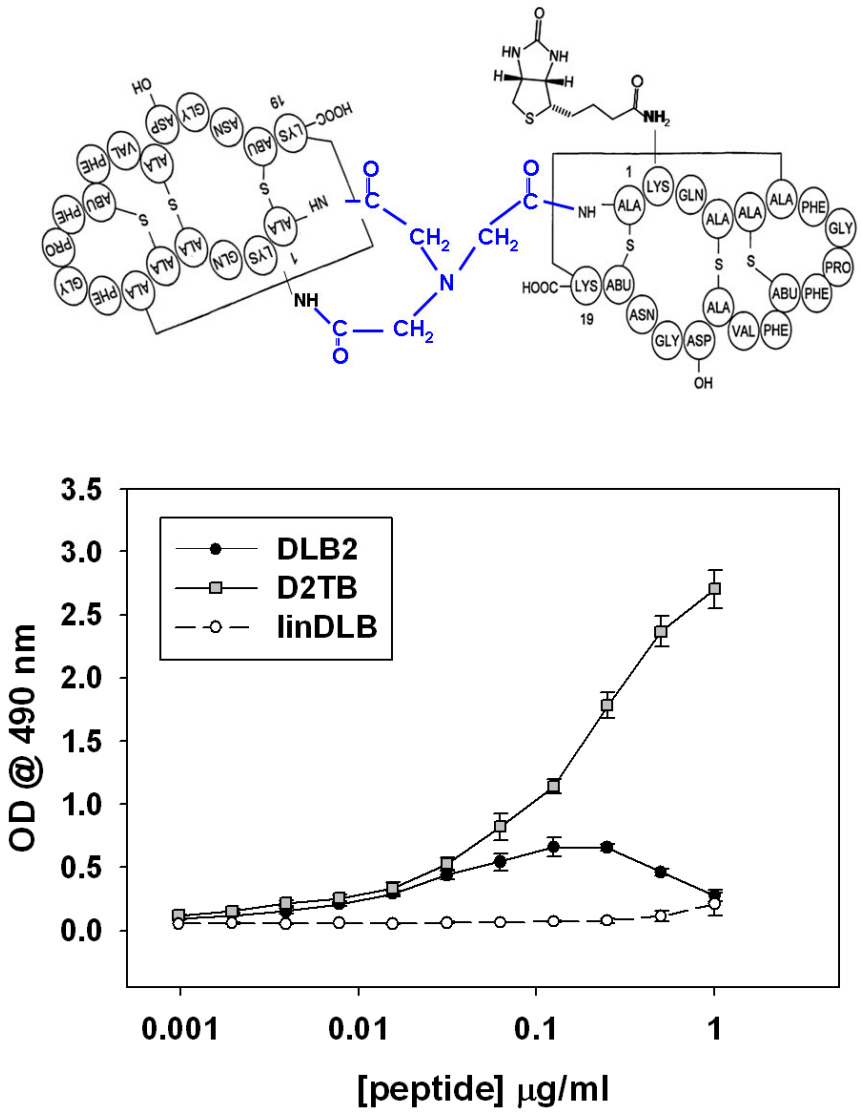

Figure 4.6. Duramycin dimer (DT2B) binds PE better than DLB2. Structure of duramycin dimer with two molecules of duramycin conjugated to one another by a T-shaped linker leaving one amino group free for biotin conjugation (D2TB) and ELISA demonstrating D2TB binds PE better than DLB2.

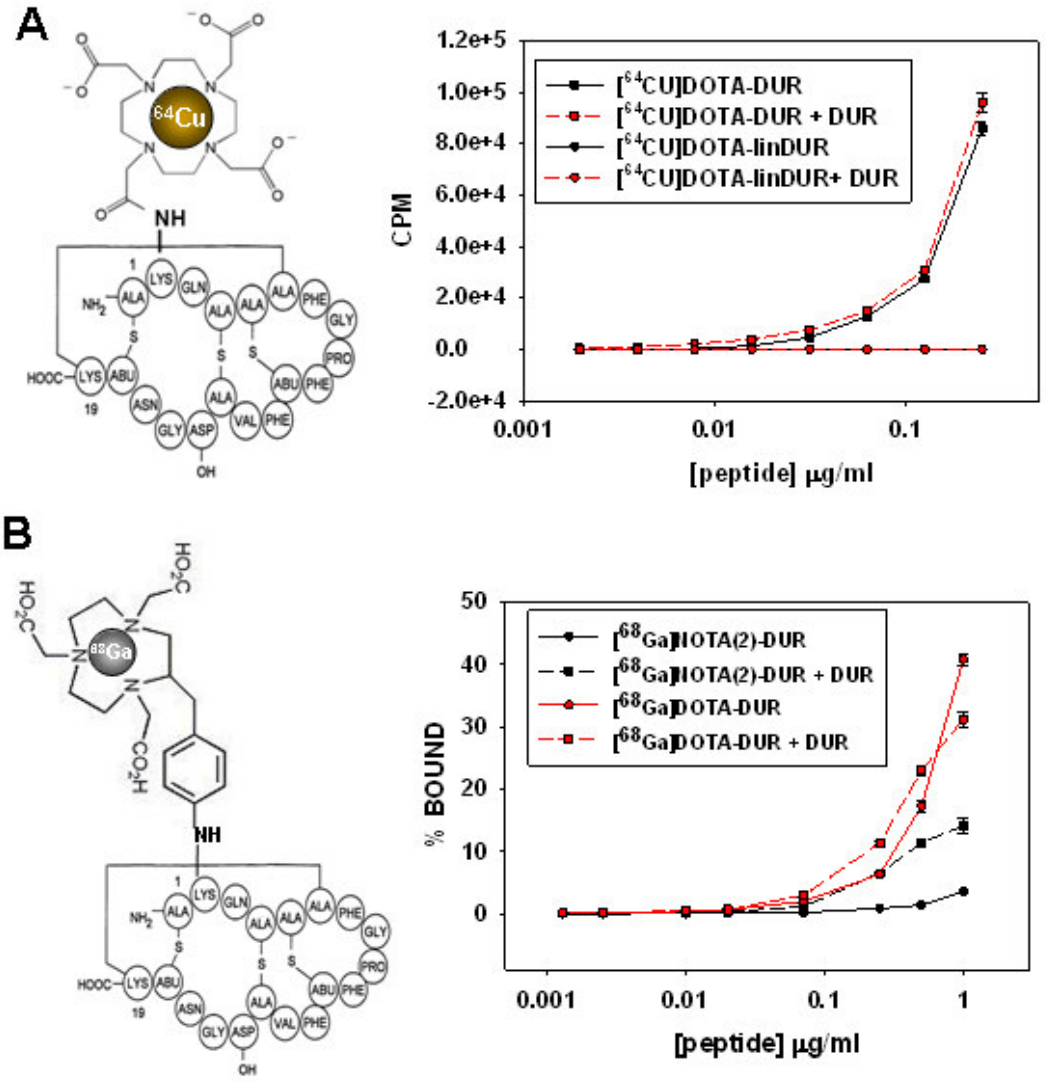

Figure 4.7. Duramycin labeled with PET isotopes. **(A)** Structure of copper-64-labeled duramycin ([64Cu]DOTA-DUR) and binding assay demonstrating [64Cu]DOTA-DUR binds PE specifically**.** [64Cu]DOTA-DUR is not enhanced by the presence of unmodified duramycin. **(B)** Structure of gallium-68-labeled duramycin ([68Ga]NOTA-DUR) and binding assay demonstrating that duramycin with a single modification binds more efficiently than duramycin modifications at both the N-terminus and adjacent lysine (e.g. [68Ga]NOTA(2)-DUR). However, addition of unmodified duramycin enhances binding of [68Ga]NOTA(2)-DUR.

Modification of duramycin to create the PE-binding probes DLB and 800CW-DUR

Duramycin labeled with a single biotin tag (DLB) was produced by reacting duramycin with the NHS ester of L-biotin (**Fig. 4.8A**) in a 1:1 molar ratio. Preliminary *in vitro* binding data indicated that DLB binding to PE was strengthened by the addition of an equal weight of unmodified duramycin (DUR) and that DLB/DUR functioned as a superior PE-binding probe compared to DLB2/DUR (data not shown). Therefore, the remaining experiments described in this thesis were conducted with a 1:1 mixture of DLB and DUR referred to as DLB to simplify nomenclature. The lipid binding specificity of DLB was assessed by ELISA. **Figure 4.8A** shows that DLB binding was specific for PE with maximum binding occurring at ~0.5 µg/ml (0.2 µM). Although some binding to PC was observed at the higher concentrations, binding to PS, PI, PA and SM was undetectable. 800CW-DUR for non-invasive *in vivo* imaging, was produced by reacting duramycin with the NHS ester of IRDye 800CW (**Fig. 4.8B**). Similar to DLB, the IR probe (800CW-DUR) demonstrated specificity for PE up to ~5 µg/ml (**Fig. 4.8B**). Maximal binding occurred at ~5 µg/ml (1.7 µM). Thus, modification of duramycin by conjugation to L-biotin did not change its affinity or specificity of binding to PE. DLB lysed 50% of murine red cells at 80 µM as compared with 20 µM for duramycin itself, showing that biotinylation reduced the hemolytic activity of duramycin cells by 4-fold (**Fig. 4.9**).

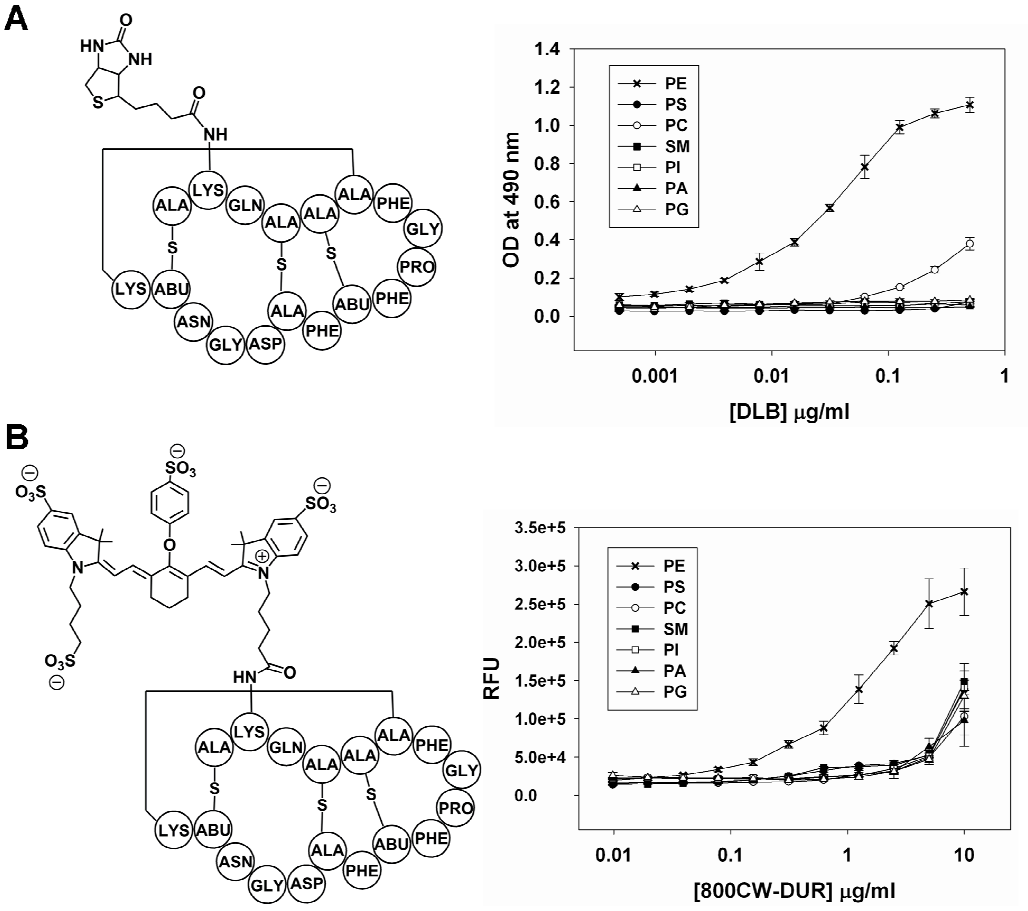

Figure 4.8. Lipid specificity of the PE binding probes DLB and 800CW-DUR. (A) Structure of duramycin-L-biotin (DLB) and ELISA showing DLB binds specifically to PE. (B) Structure of duramycin conjugated to the near-infrared fluorophore IRDye 800CW (800CW-DUR) and ELISA showing 800CW-DUR also retains binding specificity for PE. The structures show conjugation through the preferred lysine although conjugation can also occur at the N-terminus.

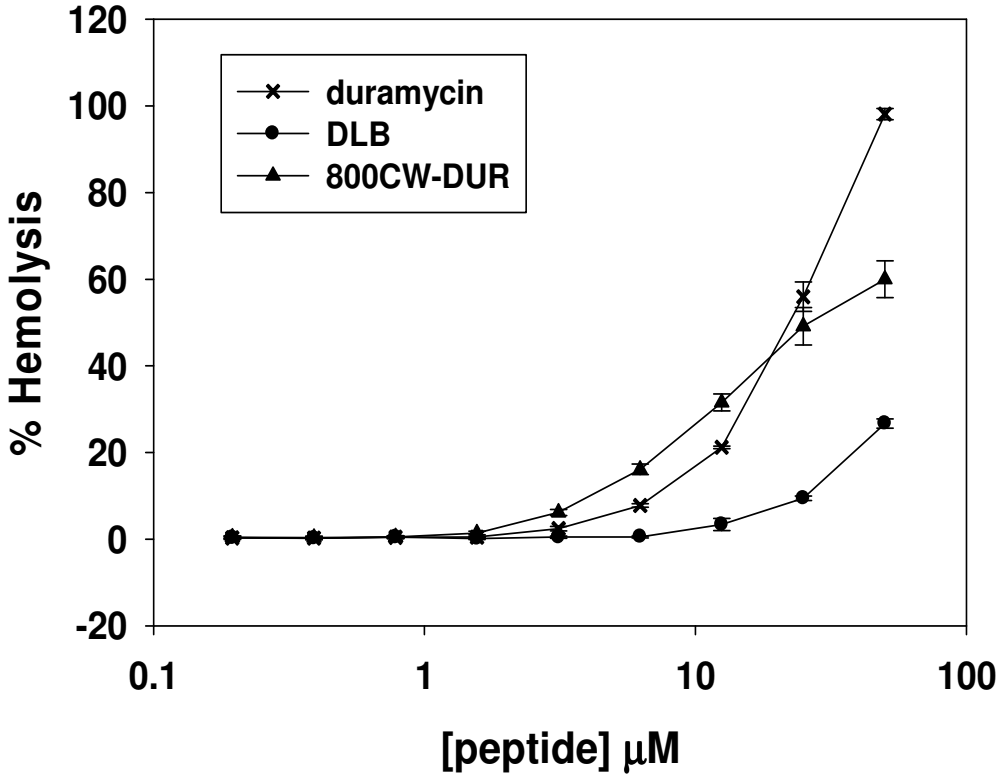

Figure 4.9. DLB and 800CW-DUR are less hemolytic than unmodified duramycin. Chemical modification of duramycin reduced the hemolytic activity by approximately 4-fold. DLB and 800CW-DUR lysed 50% of murine red cells at ~80 μM whereas ~20 μM unmodified duramycin caused 50% hemolysis.

DLB binds to PE on the surface of irradiated EC

We have previously shown that binding of fluorescent liposomes coated with duramycin or bavituximab to ABAE cells is enhanced by x-irradiation [100]. Here, we used biotinylated duramycin (DLB) with FACS analysis and immunofluorescence staining to detect PE on the surface of non-irradiated and irradiated ABAE cells. **Figure 4.10A** shows that DLB bound to 37% of control ABAE cells. Irradiation increased DLB binding to 93% of the cells and increased their median fluorescence intensity by 4-5-fold. Consistent with previous data showing that irradiation induces PS externalization, immunofluorescence analysis of the cells 24h after 5Gy irradiation showed that both DLB (PE) and bavituximab (PS) bound to membrane blebs (**Fig. 4.10B**).

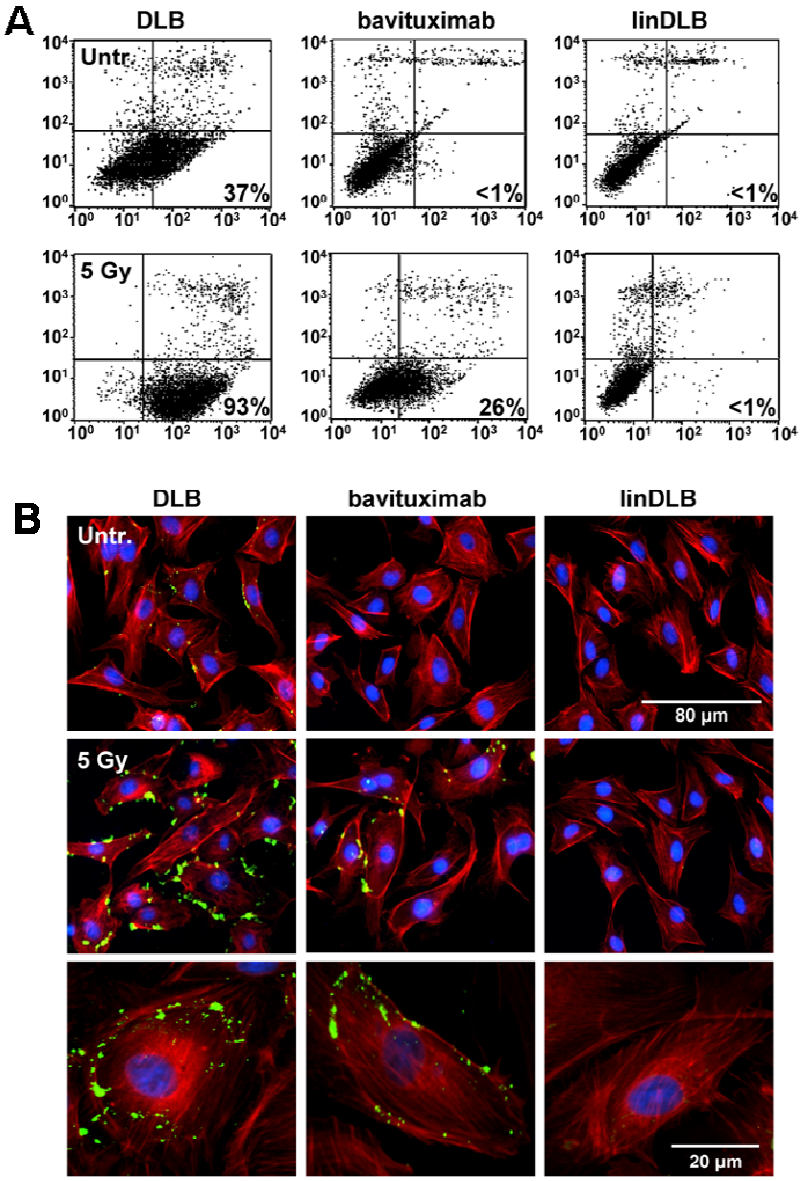

Figure 4.10. DLB Binds PE exposed on cultured EC. DLB was used to detect PE on the surface of irradiated ABAE cells. A) FACS analysis of DLB-labeled ABAE cells that were untreated (upper panels) or had been irradiated with 5 Gy 24 h earlier (lower panels). B) Cells were incubated with DLB or bavituximab and binding was detected with streptavidin-Alexa Fluor 488 and Cy2-goat anti-human IgG, respectively. LinDLB was used as a negative control for DLB. The cells were counterstained with Texas red-phalloidin.

Induction of PE exposure on cultured EC by ROS, hypoxia, and low pH

Flow cytometry was used to assess PE levels on EC after treatment with different inducers of oxidative stress present in the tumor microenvironment. Treatment of cultured EC with irradiation, H_2O_2, low pH and hypoxia increased the percentage of cells expressing PE from ~35% to 70-90% (**Fig. 4.11**). Treatment with vascular endothelial growth factor (VEGF) did not influence the externalization of PE. Similar trends were seen when bavituximab was used to stain externalized PS. Bavituximab did not stain resting EC, but stained 10-25% of the cells after they had been treated with irradiation, H_2O_2, low pH or hypoxia.

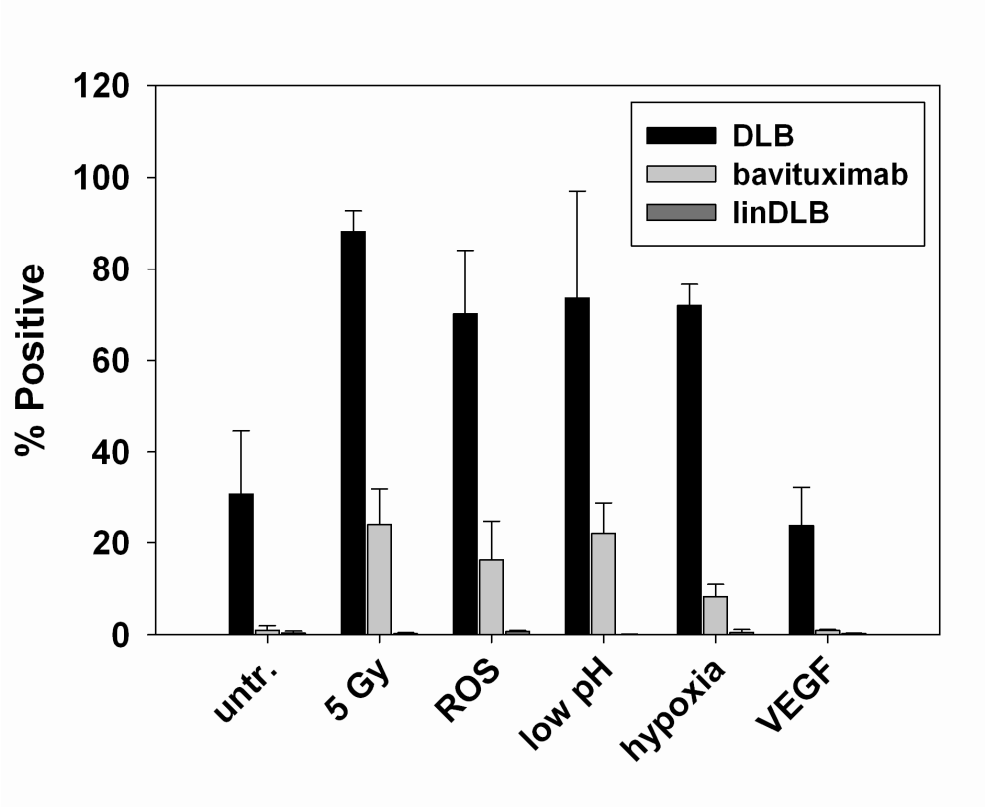

Figure 4.11. Multiple stresses associated with the tumor microenvironment induce increased PE exposure on cultured EC. Flow cytometry was used to assay PE levels on ABAE cells following: 1) treatment with 10 µM H_2O_2 to simulate ROS; 2) incubation in media at pH 5.8 for 24 h; 3) incubation under hypoxic conditions (1% O_2, 94% N_2, 5% CO_2) followed by reoxygenation for 4 h (5% CO_2 in air); and 4) treatment with 20 ng/ml VEGF. 5 Gy irradiation was used as a positive control. Bavituximab was used to detect PS externalization. Rituxan gave no staining (not shown). LinDLB was used as a negative control DLB.

Some cancer cells and tumor-associated macrophages are constitutively PE-positive

We have previously identified several transformed cell lines that have constitutive exposure of PS on their surface. Since PS and PE share common transporters, we reasoned that these same lines would also have exposed PE. Flow cytometry with DLB was used to assay PE levels on these cell lines. A20 murine B-cell lymphoma, P388 murine monocytic leukemia, and J774 murine macrophages, all express relatively high levels of PS on their surface with approximately 30-80% staining positive for bavituximab (**Fig. 4.12B**). However, corresponding levels of exposed PE were only observed on the A20 cells (**Fig. 4.12A**). Approximately 57% of A20 cells stained positively for PE and 43% stained positively for PS. J774 and P388 cells had significantly less PE on their surface with approximately 25% and 10% staining positively for DLB respectively. L540 human Hodgkin's lymphoma and U937 human monocytic leukemia did not stain positively for PS, but approximately 15-25% of these cells did stain positively for PE. Further work is required to uncover the reason for PS and PE not showing parallel exposure patterns in these cell types.

Irradiation increased PE exposure on all of the cell lines except for A20 cells (**Fig. 4.13B**). The fraction of viable PE-positive ($DLB^{+}PI^{-}$) J774 cells increased from 12% to 66% 24 h after treatment with 5 Gy (Fig. 13A). Similarly, the percentage of PE-positive P388, L540, and U937 cells increased from 10-25%

to 25-50% (**Fig. 4.12B**). The lack of an increase in viable PE-positive A20 cells was due to a dramatic increase in apoptotic cells (DLB^+PI^+) following 5 Gy irradiation (data not shown).

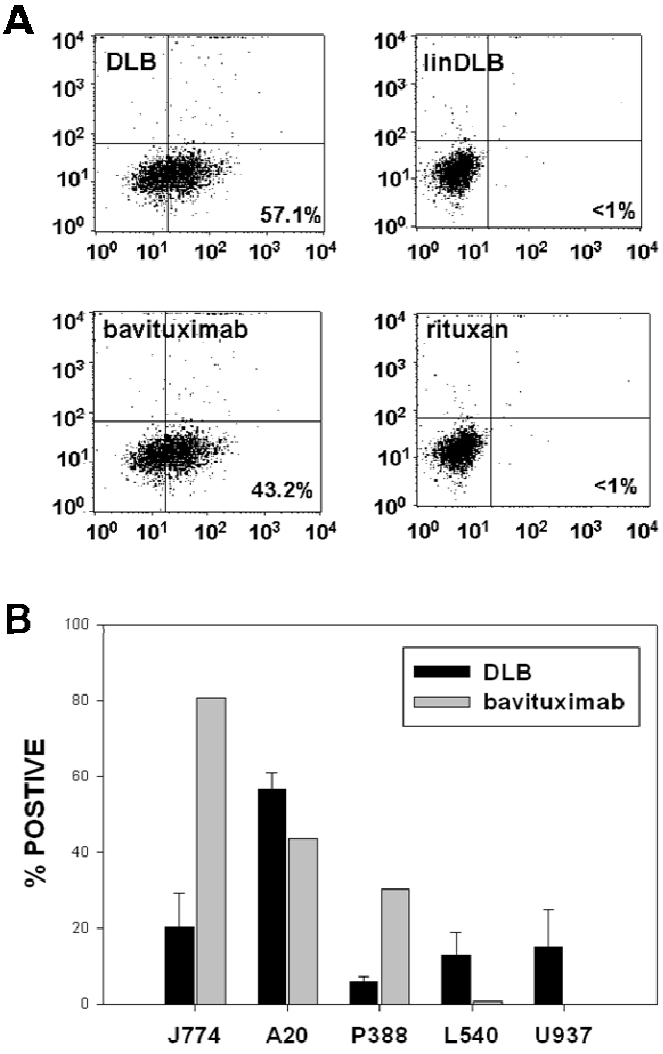

Figure 4.12. Some cancer cells and tumor-associated macrophages are constitutively PE-positive. (A) FACS plots showing A20 mouse B lymphoma cells have both PE and PS exposed on their surface under normal physiological conditions. Approximately 57% were positive for PE as indicated by duramycin staining and 43% were positive for PS as indicated by bavituximab staining. Apoptotic cells were identified by PI staining (Y-axis). LinDLB and rituxan were used as negative controls for DLB and bavituximab respectively. (B) Summary of FACS analysis of multiple transformed cell lines. All cell lines examined stained positive for PE. Although macrophage cell lines J774 and P388 were found to high levels of PS there was not a tight correlation with PE exposure.

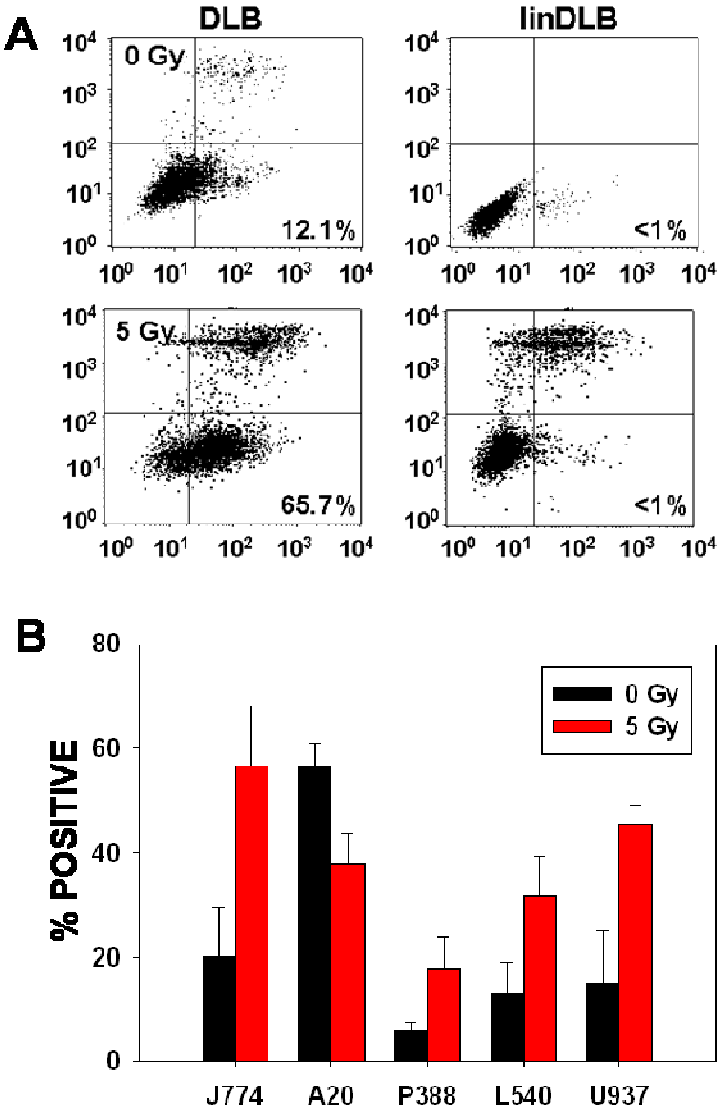

Figure 4.13. Radiation treatment increases PE exposure on cancer cells and tumor-associated macrophages. A) FACS plots showing 5 Gy irradiation increases exposure of PE on the surface of viable J774 cells. Apoptotic cells were identified by double staining with DLB and PI (upper right hand quadrant). B) Summary of FACS analysis demonstrating that DLB detected increased PE expression in all irradiated cancer cell lines except A20. A20 cells are extremely sensitive to radiation and the apparent decrease in PE-positive cells is due to an increase in apoptotic cells.

DLB localizes to tumor blood vessels

Intravenously injected DLB localized to tumor vessels in all tumors examined (**Table 2, Fig. 4.14**). PE-positive vessels were identified from colocalization of DLB with CD31 stained structures having a vascular morphology. Among the implanted solid tumor models, the endothelium in syngeneic RM-1 and RM-9 prostate carcinomas displayed the highest levels of exposed PE with ~50% of the vessels staining positive. Orthotopically implanted human (MDA-MB-231) and mouse (4T1) breast carcinomas displayed ~29% and ~13% PE-positive blood vessels, respectively. Spontaneously developing breast tumors in MMTV-PyMT transgenic mice contained 44% PE-positive vessels (**Fig. 4.15**).

The fraction of PE-positive blood vessels in each tumor model correlated with the fraction of PS-positive blood vessels detected with bavituximab (**Table 2, Fig. 4.14**). Co-injection of DLB and bavituximab into mice bearing subcutaneous RM-9 tumors revealed that the same tumor blood vessels were positive for both PE and PS (**Fig. 4.16**). The pattern of DLB staining generally resembled that of bavituximab, with both demonstrating relatively homogeneous co-staining with CD31. However, some DLB-positive vessels also exhibited punctate staining (as in **Fig. 4.16**) that may indicate regions of endothelium having membrane blebs similar to those seen on cells in tissue culture. DLB bound specifically to PE exposed on the tumor endothelium and did not appear to

extravasate from the blood vessels and bind tumor cells, or become trapped within the interstitium. Intravenously-injected linDLB did not localize to tumor blood vessels.

The binding of DLB to vasculature was largely restricted to tumor blood vessels. DLB did not localize to the endothelium in the heart, lung, liver, spleen, stomach, intestine, muscle, fat, brain, or testis (**Table 2, Fig. 4.17**). In the kidney, DLB did not stain endothelium in the glomeruli or larger vessels but did stain endothelium in intertubular vessels between the distal tubules. DLB also showed diffuse staining of the distal kidney tubules themselves, and, to a lesser extent, of proximal tubules. DLB uptake by the kidneys was not unexpected since the urinary system is the main route by which duramycin is eliminated from the body [208-209]. DLB also stained a population of CD31-negative cells in the liver, which appeared from their morphology to be Kupffer cells.

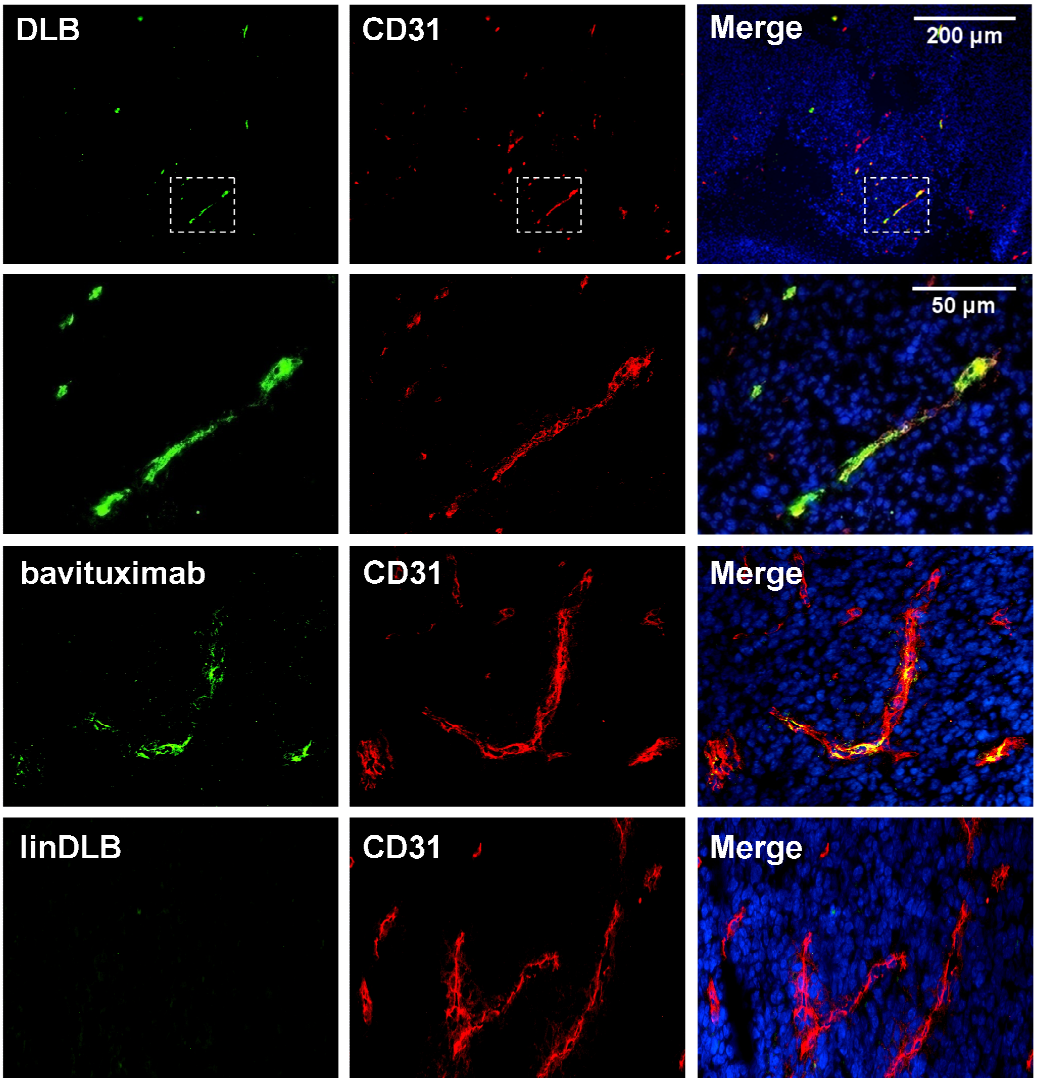

Figure 4.14. Exposure of PE on vascular endothelial cells in tumors. 100 µg DLB was injected i.v. into mice bearing subcutaneous RM-9 prostate tumors. After 1 hr, mice were perfused and tumors and major organs were harvested. IHC staining of frozen sections revealed that DLB (green) co-localized with the pan-endothelial marker CD31 (red) in tumors. PE exposure was observed in multiple tumor types (Table 1). Bavituximab produced a similar staining pattern to DLB.

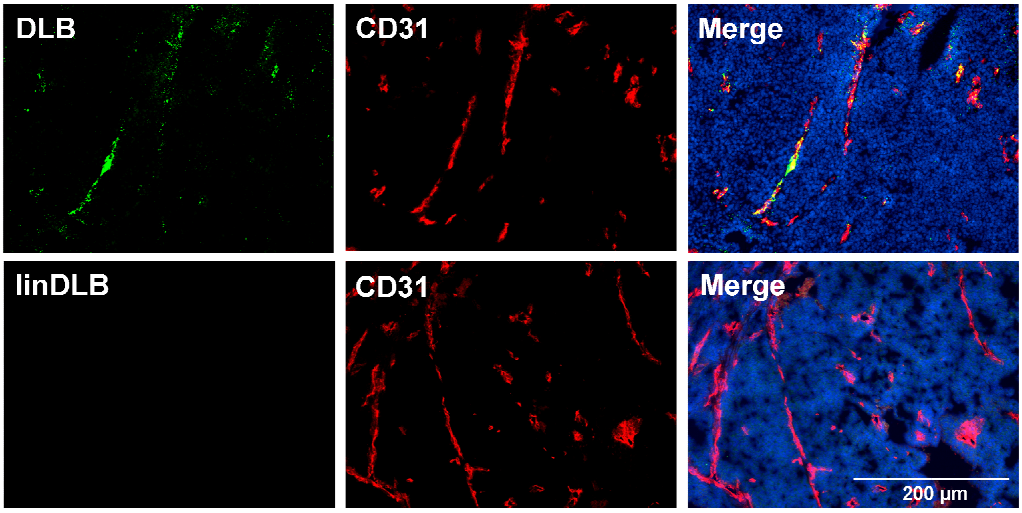

Figure 4.15. DLB localizes to vasculature in spontaneously developing PyMT breast tumors. 100 µg DLB was injected i.v. into female PyMT mice bearing palpable breast tumors (~ 0.3 cm in diameter). After 1 hr, mice were perfused and tumors and major organs were harvested. IHC staining of frozen sections revealed that DLB (green) co-localized with the pan-endothelial marker CD31 (red) in tumors.

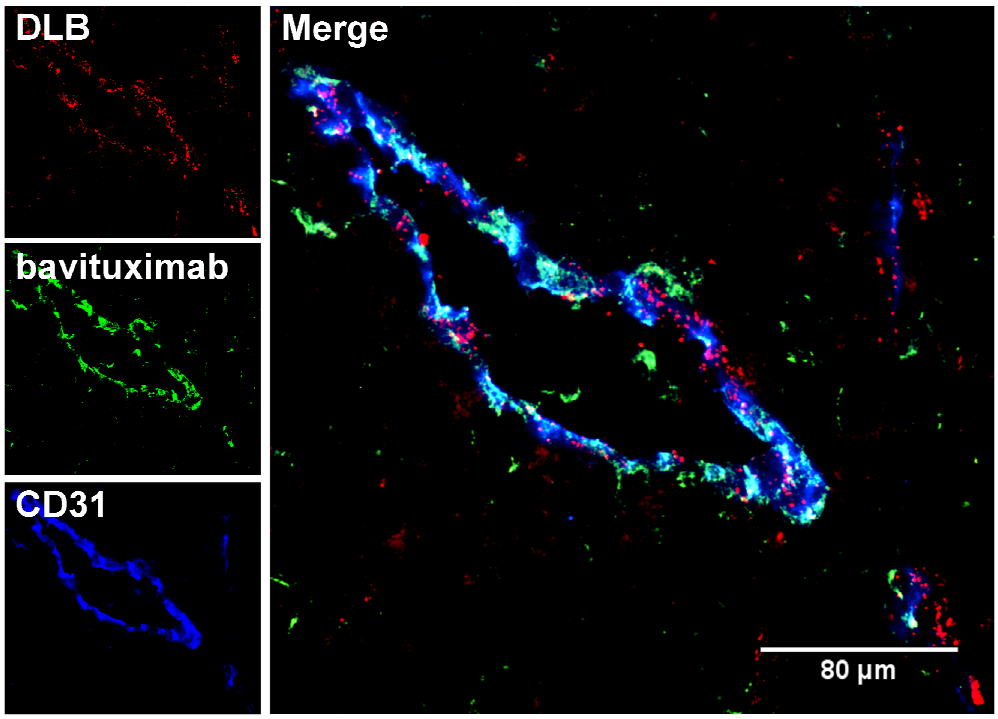

Figure 4.16. DLB and bavituximab co-localize to the same tumor vessels following intravenous injection. 150 µg bavituximab and 100 µg DLB were injected i.v. into mice bearing subcutaneous RM-9 prostate tumors. After 1 hr, mice were perfused and tumors and major organs were harvested. IHC staining of frozen sections revealed co-localization of DLB (red) and bavituximab (green) on tumor blood vessels identified by CD31 staining (blue). Blebs that appear yellow or white are costained. Most of the blebs that appear red in this merged image were also bavituximab positive, but the red color dominated the green color.

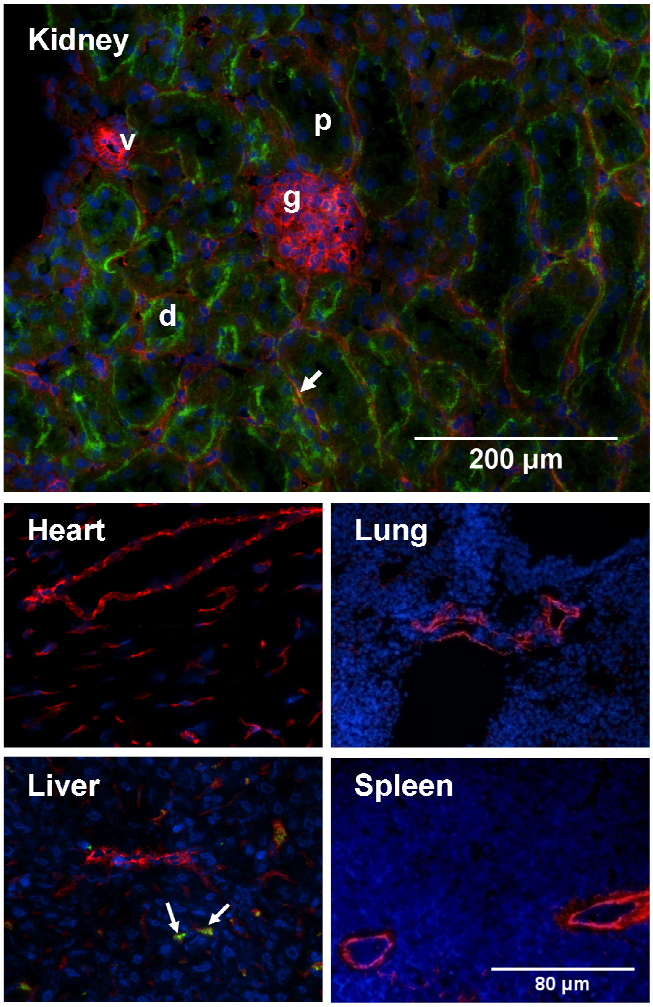

Figure 4.17. DLB localizes to tubules and intertubular vessels in the kidney, but does not localize to endothelium in other normal tissues. 100 µg DLB was injected i.v. into mice bearing subcutaneous RM-9 prostate tumors. After 1 h, mice were perfused and tumors and major organs were harvested. Frozen sections were analyzed by IHC. DLB was detected by Alexa Fluor 488-streptavidin (green), CD31 was detected by rat anti-mouse CD31/goat anti-rat IgG-Cy3 (red), and cell nuclei were detected by DAPI (blue). DLB bound to the proximal (p) and distal (d) collecting tubules of the kidney. DLB also bound to the intertubular blood vessels (arrow) between distal tubules. It did not stain endothelium in larger blood vessels (v) or in the glomeruli (g). DLB did not bind to endothelium in the heart, lung, liver or spleen. DLB stained CD31-negative cells in the liver that appear to be Kupffer cells (arrows).

Tissue	DLB	bavituximab	linDLB
Tumors			
RM-1	47 ± 9	58 ± 12	0
RM-9	56 ± 3	60 ± 8	0
MDA-MB-231	29 ± 5	31 ± 8	0
4T1	13 ± 3	28 ± 5	0
B16	17 ± 5	18 ± 7	0
A549	21 ± 7	23 ± 6	0
MMTV-PyMT	41 ± 3		0
Normal			
Heart	0	0	0
Lung	0	0	0
Liver	0	0	0
Kidney	45 ± 10	0	0
Spleen	0	0	0
Stomach	0		
Intestine	0		
Bladder	0		
Muscle	0		
Fat	0		
Brain	0		
Testes	0		

Table 2. Percentage of PE-positive blood vessels in various tissues.

PE may be exposed on endothelium during physiological angiogenesis

DLB localized to ovarian blood vessels in ovulating female BALB/C mice (**Fig. 4.18**). Most EC in the ovaries were found to have relatively high levels of PE on their surface with DLB exhibiting the same punctate staining pattern observed on tumor EC. However, unlike tumor EC, EC in stimulated ovaries did not stain positively for bavituximab. This suggests that PE may be an angiogenesis marker whereas PS is not.

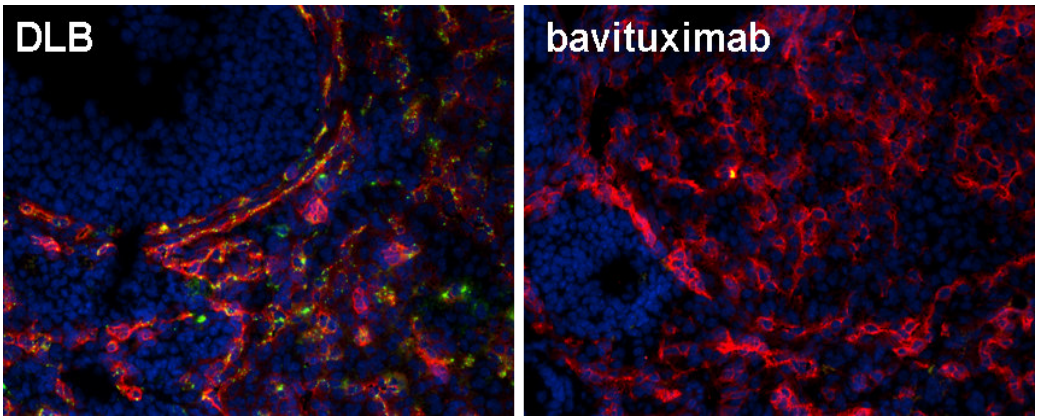

Figure 4.18. PE may be exposed on endothelium during physiological angiogenesis. IHC staining of ovary sections showing DLB (green) co-localized with CD31 (red) following i.v. injection in ovulating female mice. Bavituximab did not localize to angiogenic endothelium in the ovaries.

Radiation treatment increases PE exposure on tumor endothelium

Treatment with 15 Gy significantly increased the fraction of PE-positive vessels in 4T1 tumors within 24 h (**Fig. 4.19**). Whereas only ~13% of the blood vessels in untreated 4T1 tumors stained positively for DLB, >50% stained positively in irradiated tumors. This increase PE exposure on tumor endothelium in response to irradiation correlated with an increase in PS exposure as detected by bavituximab localization (**Fig. 4.19**).

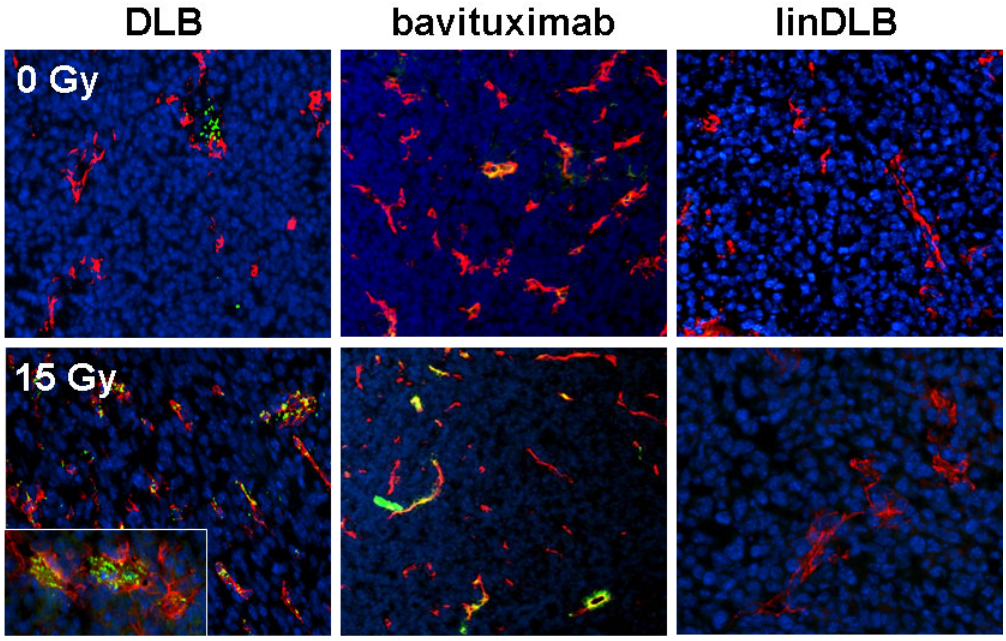

Figure 4.19. Radiation treatment increases PE exposure on tumor endothelium. IHC staining showing an increased number of PE-positive (DLB, green) blood vessels (CD31, red) in orthotopic 4T1 murine mammary tumors treated with 15 Gy focal irradiation 24 h prior to injection of DLB. Increased PE exposure on irradiated tumor endothelium correlated with increased PS exposure detected by bavituximab localization.

DLB binding is high in hypoxic areas of tumors

Abnormal angiogenesis in tumors often results in malformed blood vessels that fail to provide adequate blood flow throughout the tumor. Therefore, specific areas within a tumor are subject acute ischemic hypoxia that is often transient [210-211]. Since hypoxia induced PE exposure in *in vitro* cultivated EC (**Fig. 4.11**), we determined whether tumors growing in mice also expressed PE in hypoxic regions. Mice bearing similar-sized (1 cm diameter) RM-9 or 4T1 tumors were injected with DLB to detect PE and pimonidazole to assess hypoxia. The mice were killed 1 h after injection, perfused with saline and frozen sections of tumors were examined by immunohistochemistry. The results presented in **Figure 4.20** show a correlation between the distribution of PE-positive (red) EC and hypoxic regions (green) of the tumor. RM-9 tumors, in which PE-positive vessels were abundant, had large areas of hypoxia throughout the tumor, whereas 4T1 tumors, in which PE-positive vessels were sparse, had smaller, more localized, areas of hypoxia and much less hypoxia overall (**Fig. 4.21**). Hypoxic regions were most pronounced around necrotic regions and in central areas of the tumor. Consistent with previous localization experiments, DLB stained >50% of the blood vessels in the RM-9 tumors. Most of the DLB positive vessels were located in and around the hypoxic regions (top right panel **Fig. 4.20**). The control peptide linDLB did not bind tumor EC (not shown).

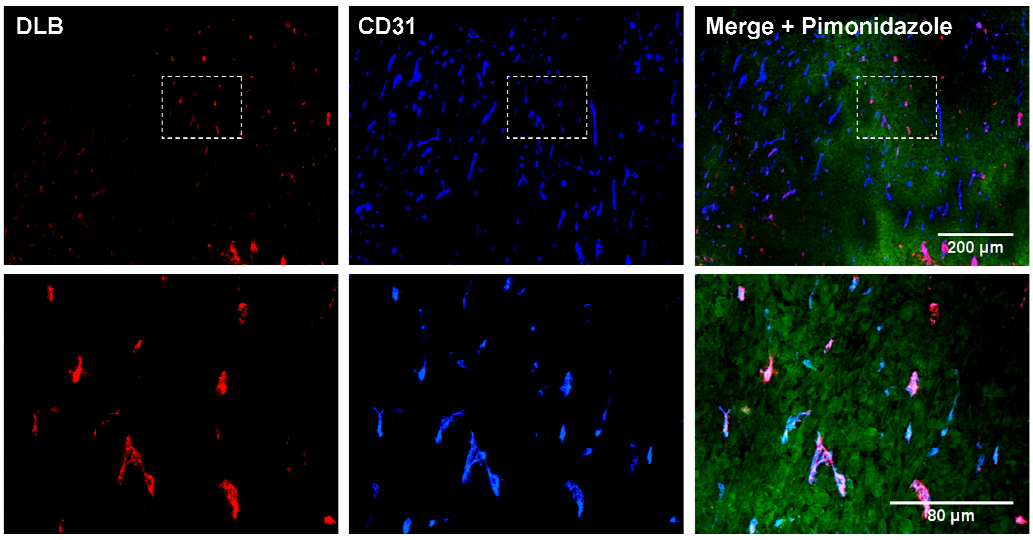

Figure 4.20. PE exposure on tumor vessels is predominately in hypoxic areas. Mice bearing subcutaneous RM-9 prostate tumors were injected with DLB to detect PE and pimonidazole HCl to detect hypoxia. IHC staining of frozen sections demonstrated that PE exposure on tumor vessels occurred predominantly in hypoxic areas of the tumor. DLB, red; CD31, blue; hypoxia, green.

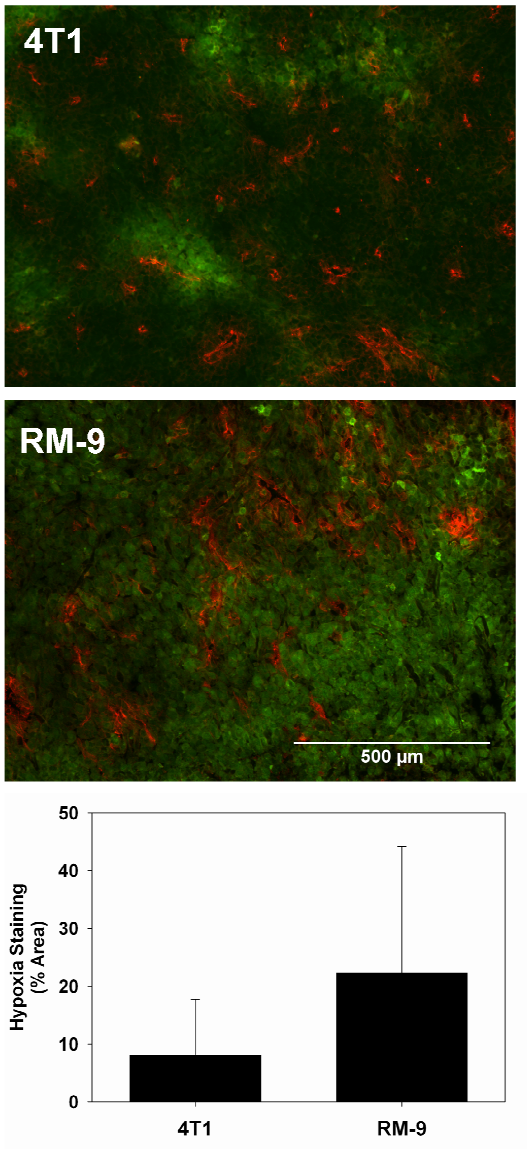

Figure 4.21. RM-9 prostate tumors are more hypoxic than 4T1 breast tumors. Pimonidazole HCl was injected into mice bearing either subcutaneous RM-9 tumors or orthotopic 4T1 tumors to detect hypoxia. IHC staining of frozen sections revealed that RM-9 tumors were markedly hypoxic throughout, whereas 4T1 tumors had smaller, more discrete, areas of hypoxia. Hypoxia, green; CD31, red. The greater hypoxic fraction in RM-9 tumors may explain the greater percentage of PE-positive vessels in these tumors compared to 4T1 tumors.

Duramycin radiolabeled for PET imaging demonstrates high uptake in liver and kidneys

Duramycin labeled with gallium-68 ([^{68}Ga]DOTA-DUR) was injected intravenously into female athymic nu/nu mice bearing subcutaneous A549 human lung carcinomas in their right hand flank. [^{68}Ga]DOTA-DUR showed some tumor uptake in PET images obtained at 30 min and 120 min post-injection (**Fig. 4.22**). However, the signal intensity from the liver was significantly higher than the tumor. Duramycin was also labeled with copper-64 ([^{64}Cu]DOTA-duramycin) and injected into mice bearing A549 tumors. Tumors and normal tissues were harvested after 2 hr, wet-weighed, and measured for activity. [^{64}Cu]DOTA-duramycin did demonstrate any tumor uptake and only showed high accumulation in the liver and kidneys (**Fig. 4.23**). Addition of unmodified duramycin did not improve tumor uptake as expected, but instead increased uptake in the liver.

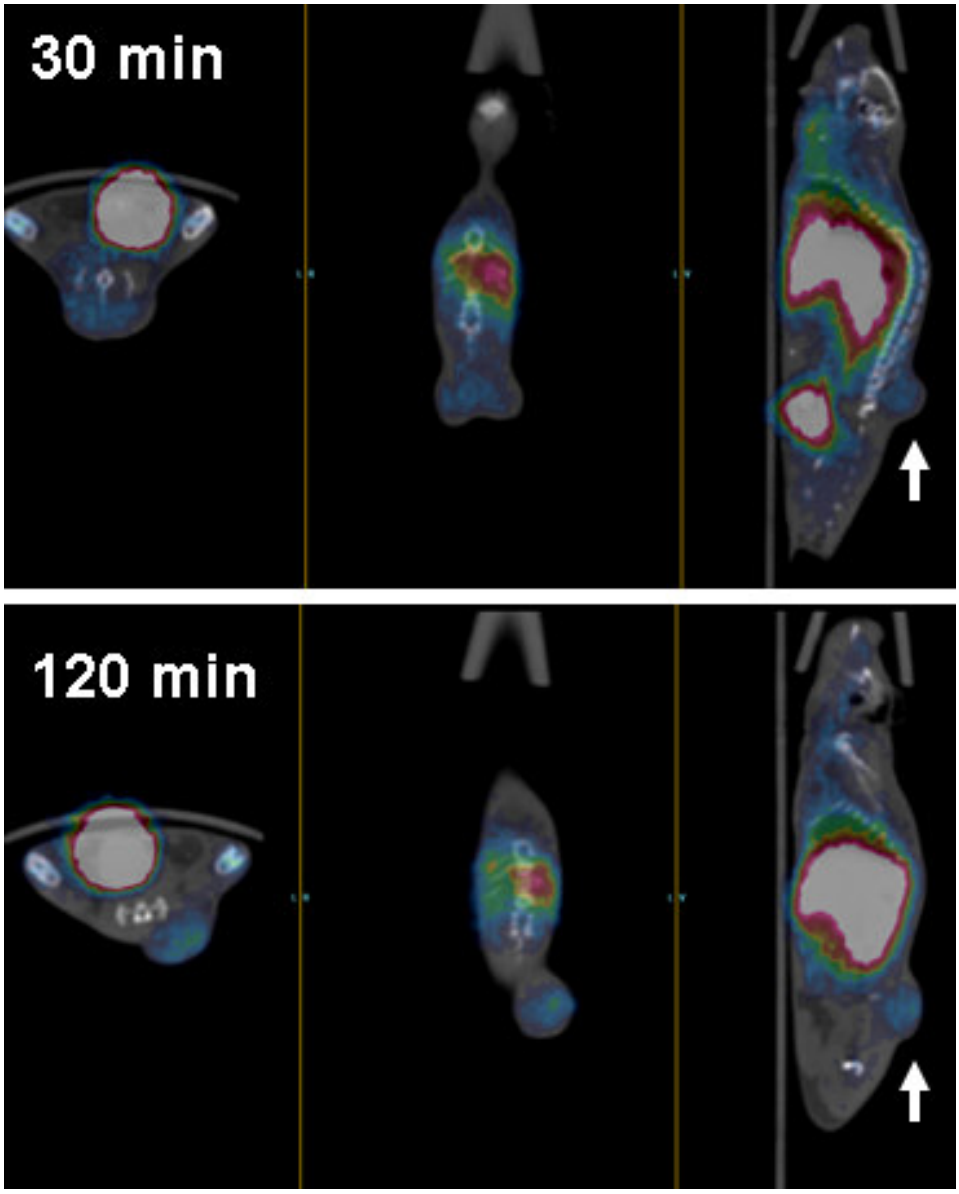

Figure 4.22. [68Ga]-DOTA-DUR labels tumors, but exhibits high liver uptake. Duramycin labeled with gallium-68 ([68Ga]-DOTA-DUR) was used for PET imaging of A549 xenografts growing in the right hind flank of mice (arrow). Tumor uptake of [68Ga]-DOTA-DUR was low compared to liver uptake. Transverse, coronal, and sagittal images are shown from left to right.

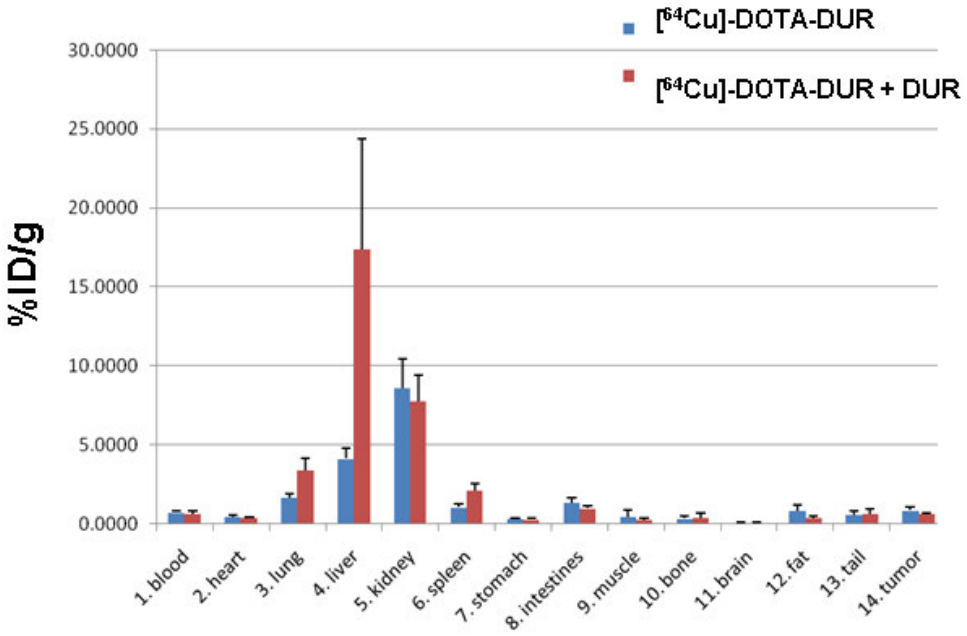

Figure 4.23. Biodistribution data for radiolabeled duramycin. Duramycin labeled with Copper-64 ([64Cu]-DOTA-DUR) was injected into mice bearing subcutaneous A549 tumors. Biodistribution analysis revealed that [64Cu]-DOTA-DUR homed to the liver and kidneys. Addition of unmodified duramycin increased uptake by the liver.

In vivo tumor imaging with 800CW-DUR

To determine the ability of duramycin to target tumor vasculature *in vivo*, mice bearing subcutaneously-implanted RM-9 tumors were injected with 800CW-duramycin (800CW-DUR). The distribution of the probe was detected with the Xenogen IVIS imaging system 24 h later. Images are shown in **Figure 4.24**. Remarkable delineation of the implanted tumors was achieved in 3 of 3 mice. No other normal tissues showed detectable accumulation of label, with the exception of the kidneys which were strongly labeled.

Subcutaneous RM-9 tumors growing in mice were also imaged with a LI-COR Pearl imager that is optimized for 800CW (**Fig. 4.25**). Image analysis performed with this imaging system revealed that the tumor-to-background ratio for 800CW-DUR is not higher than that achieved with the control probe 800CW-linDUR. Nonetheless, overall signal intensity was significantly higher in tumors labeled with 800CW-DUR. Immunohistochemical analysis of the tumors demonstrated that 800CW-DUR colocalized with CD31 much like DLB (**Fig. 4.26**).

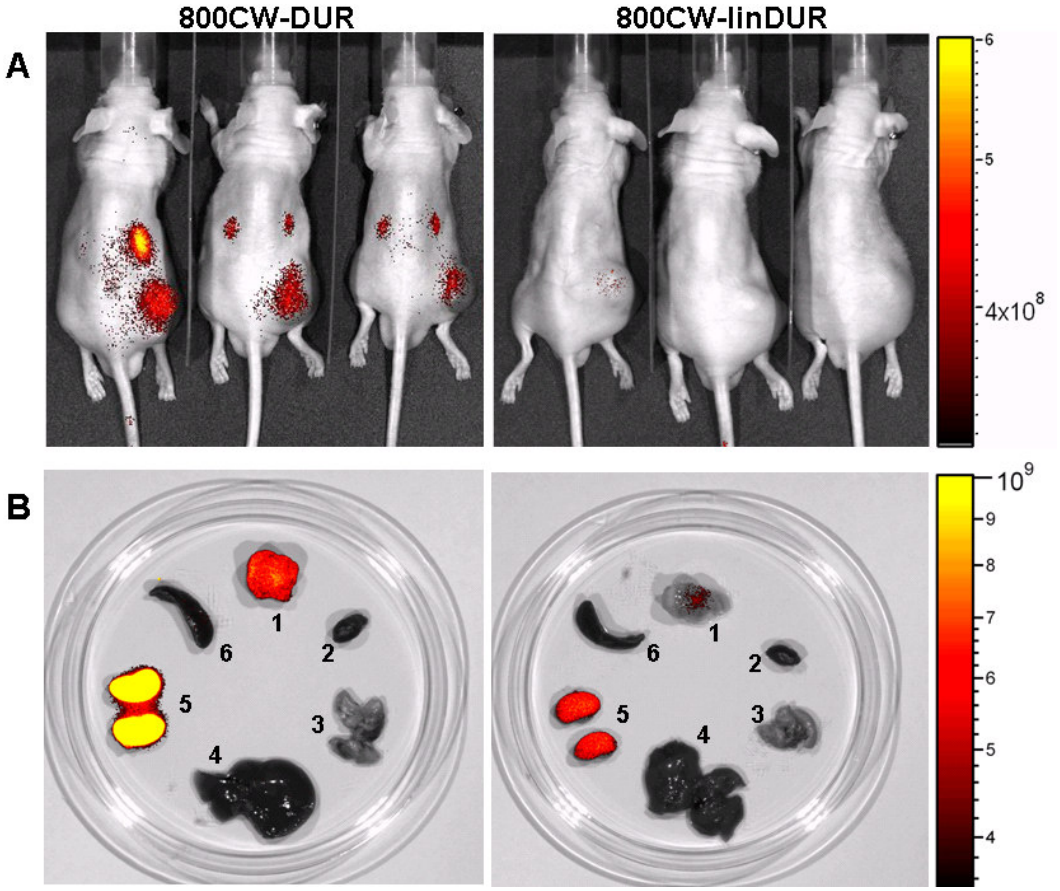

Figure 4.24. In vivo imaging of RM-9 tumors with 800CW-DUR. A) Male athymic nu/nu mice bearing subcutaneous RM-9 tumors in their right hind flank were injected with 50 µg 800CW-DUR. 800CW conjugated to linear duramycin was used as a negative control (800CW-linDUR). The mice were imaged after 24hr with a Xenogen IVIS Lumina imaging system. Fluorescence intensity is displayed as photons/s/cm2/sr. B) *Ex vivo* imaging of tumors and organs: 1) tumor, 2) heart, 3) lungs, 4) liver, 5) kidneys and 6) spleen.

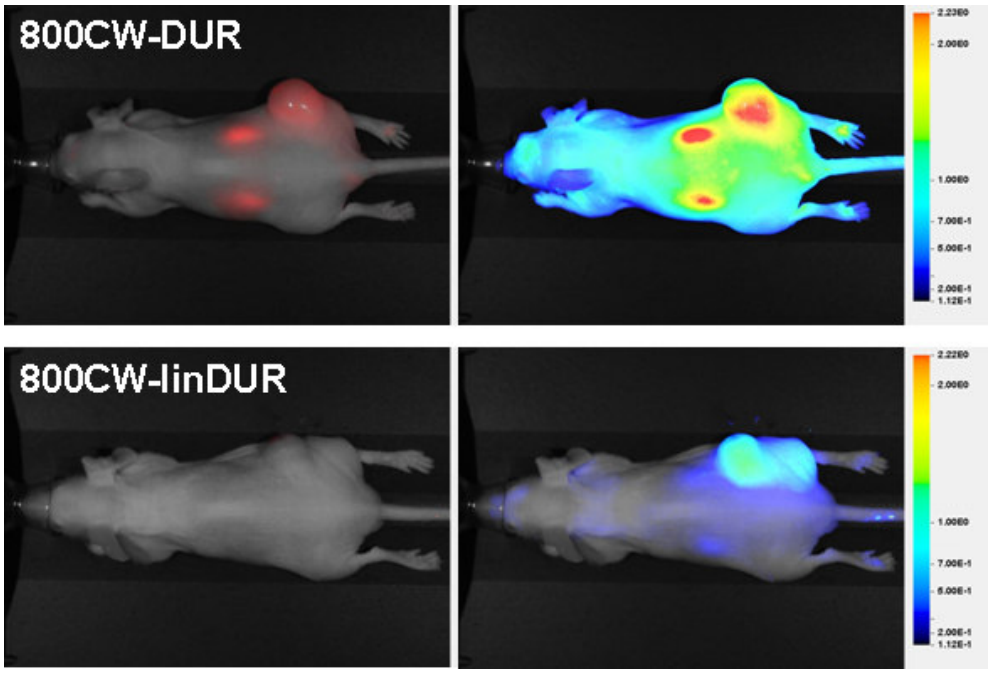

Figure 4.25. 800CW-DUR gives relatively high background signal throughout the body. Mice bearing subcutaneous RM-9 tumors were injected with 800CW-DUR and imaged with a LI-COR Pearl imager**.** The heat maps (right-hand panels) show that the tumor-to-background ratio is not higher for 800CW-DUR than the control. Nonetheless, overall signal intensity is significantly higher in tumors labeled with 800CW-DUR.

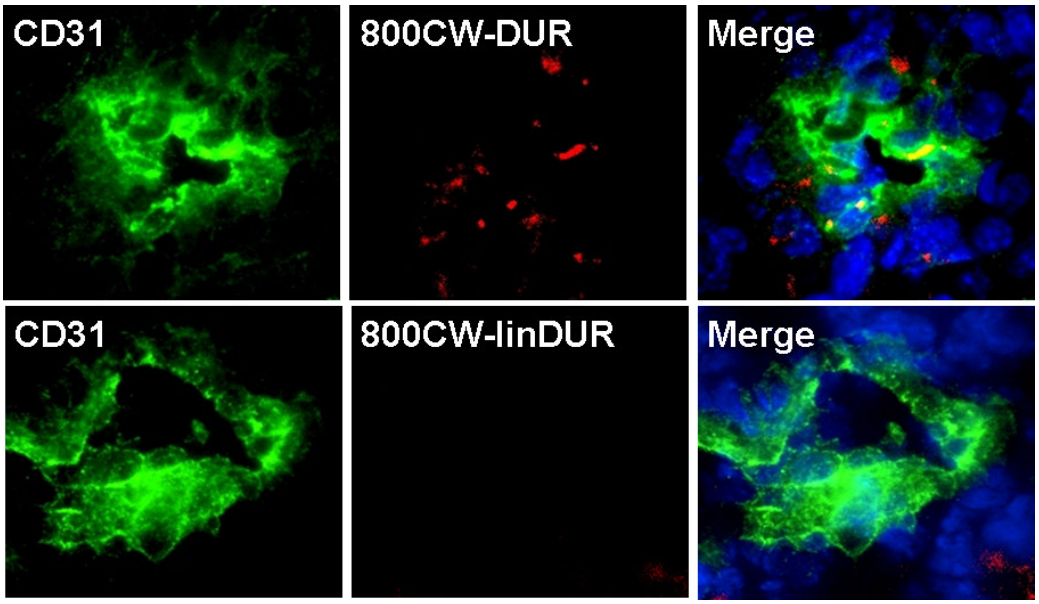

Figure 4.26. 800CW-DUR Localizes to Tumor Endothelium. IHC analysis of RM-9 tumors from mice injected with 800CW-DUR revealed that 800CW-DUR colocalized with CD31 much like DLB.

PE is externalized in prostate tumors treated with ADT

PS has received much interest as a marker for tumor response to therapy.[50, 73, 196] and the correlation in the membrane distribution of PS and PE *in vivo* suggests that exposure of PE may be an indicator of tumor response. Indeed, 800CW-DUR showed high uptake in spontaneously developing prostate tumors growing in 4 month old TRAMP mice treated with androgen deprivation therapy (ADT) compared to untreated tumors (**Fig. 4.27**). The control probe did not show any uptake in treated or untreated tumors.

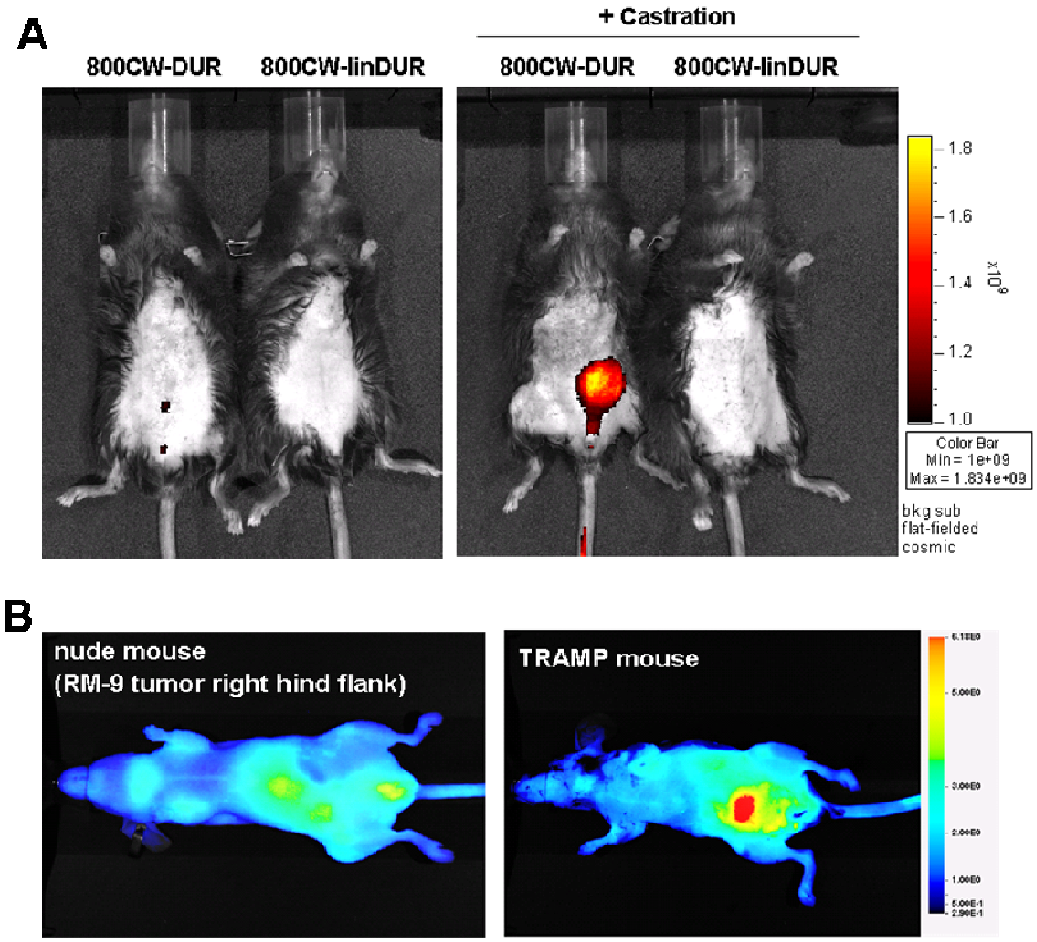

Figure 4.27. 800CW-DUR can be used to detect PE exposed in tumors in response to ADT. (**A**) Spontaneously developing prostate tumors growing in 4 month old TRAMP mice were treated with androgen deprivation therapy (ADT) (via castration) exhibited high uptake of 800CW-DUR compared to untreated tumors. B) Castrated TRAMP mouse imaged with a LiCOR Pearl imager. A mouse that does not have an orthotopic prostate tumor was injected with 800CW-DUR and used as a negative control.

Discussion

The major finding of this study is that PE becomes exposed on the luminal surface of the vascular endothelium of tumors. PE exposure is most prominent in and around regions of hypoxia and is probably induced by oxidative stresses in the tumor microenvironment.

The PE-binding peptide duramycin tagged with a single molecule of L-biotin was used to assess the presence of PE on the cell surface. Biotinylation appears to have reduced the ability of duramycin to disrupt cell membranes, since the hemolytic activity of DLB was 4-fold lower than that of duramycin itself. This is likely attributable to the increased hydrophilic character imparted by the water-soluble biotin moiety. This change may explain why DLB stained cell surface structures but not intracellular membranes at the concentrations tested. In addition, duramycin with a single modification (DLB) appeared to be more efficient at forming multimeric PE-binding complexes that duramycin modified at both the N-terminus and adjacent lysine (DLB2). Navarro et al. were the first to show that duramycin induced aggregation of PE containing liposomes using free-fracture election microscopy [105]. Their results were later confirmed by Choung et al. who proposed that membrane ion channels formed by duramycin were formed by clustering of PE molecules [212]. However, neither group directly proposed the idea of a multimeric duramycin complex. The data from competition experiments in this study suggested that such a complex may take the

form of a pentamer and therefore should be approximately 10 kDa in size. However, this complex does not form in solution in the absence of PE and therefore its size could not be confirmed by gel filtration experiments.

DLB staining indicated a 4-5 fold increase in exposure of PE on irradiated EC. DLB strongly stained membrane blebs that formed on the surface after irradiation. The pattern of DLB staining in irradiated ABAE closely resembled that of bavituximab suggesting that both PE and PS preferentially localize to membrane patches and blebs [100]. Unlike PS, basal levels of PE are exposed on normal (untreated) ABAE cells, either naturally or because ABAE cells do not readily enter a fully resting state in culture. These observations are consistent with data indicating that essentially all the membrane PS and ~80% of the membrane PE are restricted to the cells plasma membrane inner membrane leaflet [4]. Increased PE exposure has also been shown at the cell surface along the cleavage furrow in Chinese hamster ovary (CHO) cells during cytokinesis and in a subset of EC in the rat aorta [213-214]. Although PS and PE are both externalized during apoptosis and in response to stress, PS is more highly restricted to the inner membrane leaflet in healthy cells.

FACS analysis revealed that stress conditions associated with the tumor microenvironment induced significant PE exposure when applied to EC cultivated *in vitro*. Tumors are known to contain high levels of ROS due to a number of disregulated metabolic processes. These include growth factor-mediated

activation of mitochondria, inflammatory responses from tumor-infiltrating leukocytes and activation/overexpression of enzymes such as NADPH-oxidase [32-33, 215]. Transient hypoxia in tumors can lead to ROS generation by this last mechanism (i.e. activation of NADPH-oxidase) [31]. In addition to high ROS levels, the tumor microenvironment is also often characterized by low pH relative to normal tissues. Tumor cells can undergo high rates of glycolysis irrespective of oxygen tension (the Warburg effect) and generate lactic acid as a byproduct [29]. We found that the fraction of ABAE that expressed PE at the cell surface after treatment with ROS (H_2O_2), hypoxia or acidic media significantly increased (Fig. 3). These stresses also induced PS exposure. These observations suggest that ROS, hypoxia and acidic pH, possibly in concert with other factors (e.g., inflammatory cytokines and thrombin), promote the exposure of PE and PS in tumors. Although some cancer cells and tumor associated macrophages were found to exhibit constitutive PE and PS exposure, there was not a tight correlation between the two aminophospholipids across all cell lines. U937 and L540 lymphomas do not normally have any exposed PS on their surface, but were found to have a basal level of exposed PE (15-20%). Conversely, while >80% of J774 tumor-associated macrophages were found to be PS-positive the fraction of PE-positive cells was only ~25%. However, PE and PS levels were much more tightly correlated following treatment with 5 Gy. This suggests that potential PS and PE targeting drugs may function similarly when used in combination with

radiation therapy and that PS and PE targeting imaging agents may function similarly in assessing tumor response to therapy.

Without exception, increased PE exposure was found on the tumor endothelium in all the tumors examined. These models included syngeneic, human xenografts, subcutaneous, orthotopic and transgenic tumors. This suggests that, much like PS, PE functions as a broad tumor marker common to many malignancies. The percentage of PE-positive vessels varied between models, but corresponded to the fraction of PS-positive vessels (determined by bavituximab binding) for each type of tumor. This correlation was maintained in irradiated tumors, with a more that 2-fold increase in the percentage of PE-positive and PS-positive blood vessels. Moreover, the exposure of PE and PS occurred on the same tumor vessels suggesting that the same mechanism is responsible for the redistribution of both PE and PS. Tumor-bearing mice were co-injected with DLB and pimonidazole HCl to assess hypoxia in areas immediately surrounding PE-positive blood vessels. A general correlation between DLB binding and pimonidazole staining showed that PE-positive vessels were concentrated in hypoxic portions of the tumor. RM-9 tumors, which have abundant PE-positive vessels, were markedly hypoxic whereas 4T1 tumors, which have relatively few PE-positive vessels, were largely not hypoxic. These results further indicate that hypoxia, and other stresses in hypoxic tumor regions, drive PE exposure on tumor vasculature.

Despite evidence from *in vitro* experiments that normal EC contain basal levels of PE on their surface, DLB did not localize to endothelium in heart, lung, liver, spleen, stomach, intestine, muscle, fat, brain or testis. This difference might be because EC grown *in vitro* are activated due to sustained low levels of chronic stress that promote higher levels of exposed PE, whereas EC in most normal tissues *in vivo* attain true quiescence. Although there is no evidence to suggest PS is a marker of physiological angiogenesis, PE exposure was observed on EC in the ovaries of non-tumor bearing mice undergoing follicular angiogenesis. The transport enzymes that maintain membrane lipid asymmetry have a higher affinity for PS and its rate of PS transport is approximately 10-fold higher than its rate of PE transport [4, 216]. This could explain why stress has a more profound effect on the redistribution of PE.

The selective exposure of PE on tumor vascular endothelium suggested that it might serve as a marker for imaging tumors vasculature. Being luminally exposed and in direct contact with the blood, we reasoned that duramycin labeled with radioisotopes would localize rapidly and specifically to tumor endothelium. To test this hypothesis, we labeled duramycin with two different isotopes used for PET imaging ^{64}Cu and ^{68}Ga. Although duramycin labeled with either isotope demonstrated specific binding to PE, it demonstrated low tumor uptake and high liver uptake when injected into tumor bearing mice. High uptake of [^{64}Cu]DOTA-DUR and [^{68}Ga]DOTA-DUR in the liver was similar to that

observed with ^{3}H-duramycin [107], but inconsistent with the biodistribution reported by Zhao and Bugenhagen for ^{99m}Tc-duramycin [106]. One major difference between our constructs and the one used by Zhao and Bugenhagen is that the succinimidyl 6-hydrazinonicotinate acetone hydrazone (HYNIC) and tricine-phosphine coligand system used to chelate ^{99m}Tc is highly negatively charged. This difference in charge may allow duramycin, which normally has a pKa of ~9.5, to avoid uptake by cationic transporters in the liver.

In an effort to generate an *in vivo* imaging probe with an overall negative charge similar to ^{99m}Tc-duramycin, we labeled duramycin with the near-infrared dye 800CW, which is derivatized with four phosphate groups to enhance its water solubility. 800CW-duramycin was injected it into mice bearing RM-9 prostate tumors. The biodistribution of injected 800CW-DUR confirmed that the levels of exposed PE are indeed high in tumors. 800CW-DUR binding to RM-9 tumors allowed them to be clearly distinguished above background fluorescence. 800CW-DUR also demonstrated high uptake in spontaneously developing TRAMP prostate tumors treated with ADT. The TRAMP model closely mimics human prostate cancer. These data suggest that PE-specific probes may be particularly useful for imaging and assessing tumor response to therapy. However, both 800CW-DUR and DLB showed high uptake in the kidneys, as observed with ^{99m}Tc-duramycin [106]. Immunohistochemical analysis revealed that DLB localized strongly to the distal kidney tubules and less strongly to the

proximal kidney tubules. DLB also stained intertubular blood vessels between distal tubules, although it did not bind endothelium in larger renal vessels or the glomeruli. Other studies have shown that duramycin forms ion channels in artificial membranes and can disrupt mitochondrial membranes at concentrations greater than 5 μM [110, 217]. Cinnamycin has also been shown to be toxic and promote its own binding by inducing flipping of membrane lipids [218]. It is possible that, as the kidneys filter DLB or 800CW-DUR from the blood, local concentrations of the drug in the collecting ducts and the associated vasculature increase to the extent that it disrupts membranes and exposes PE. DLB mixed with unmodified duramycin demonstrated the highest binding affinity among the different constructs tested but, the duramycin dimer D2TB demonstrated higher affinity than DLB alone. Further studies are required to determine if D2TB localizes to tumors and at the same time demonstrates less kidney uptake than unmodified duramycin.

In conclusion, the data presented in this report demonstrate that PE becomes exposed on the luminal surface of tumor vascular endothelium. PE appears to be a broad marker found in a number of mouse models of solid malignancies including spontaneously developing tumors. We demonstrate that PE on tumor vasculature can be imaged with PE-targeting probes. These probes are small in size compared with PS-targeting antibodies and annexins, and clear rapidly from the bloodstream making them particularly suitable for imaging

purposes. In addition, PE is more abundant than PS, giving the potential for stronger signals. Indeed, duramycin labeled with ^{99m}Tc is being developed for imaging exposed PE in cardiac ischemia [106]. The results reported herein suggest that PE also has potential as a marker for imaging human malignancies.

CHAPTER 5

CONCLUSIONS AND FUTURE DIRECTIONS

Previous work done in Dr. Thorpe's laboratory had established PS as a highly specific marker of tumor endothelium that can be targeted by therapeutic monoclonal antibodies.[12] Jennewein et al. had also shown that one of these antibodies, bavituximab, could be labeled with the ^{74}As and used for PET imaging of tumors growing in rats.[26] Imaging tumors with ^{74}As-bavituximab served as proof-of-principle and my project was aimed at developing PS imaging agents with more favorable pharmacokinetics, lower immunogenicity and, ultimately, increased potential for translation to the clinic.

At approximately the same time my thesis work was initiated, Peregrine Pharmaceuticals, Inc. developed a fully human PS-targeting antibody named 1N11. 1N11 was found to equally effective as bavituximab in its ability to home to PS exposed on the surface of tumor endothelium following injection into tumor-bearing mice (Yin, unpublished data). This led to the hypothesis that 1N11 could also be used for non-invasive imaging of tumors. I first tested this hypothesis in collaboration with Dr. Dawen Zhao from the department of Radiology here at UT Southwestern (UTSW). Dr. Zhao had extensive experience with optical imaging and it is a modality well suited for studying drug pharmacokinetics in small animals. We were able to demonstrate that 1N11

F(ab')$_2$ conjugated to the near-infrared fluophore 800CW (800CW-1N11 F(ab')$_2$) could be used to image U87 gliomas growing in mice within 24 hr of injection of the probe. The incubation time was significantly shorter than the 72 hr required for optimum tumor-to-background ratios for ^{74}As-bavituximab. Moreover, we were able to image increased PS exposure in tumors following radiation treatment. To my knowledge, this was the first demonstration that a PS-targeting antibody (fragment) could be used to image therapy-induced changes in tumor physiology *in vivo*. Due to the design and scope of this study, however, we did not correlate 800CW-1N11 F(ab')$_2$ uptake and the effect of radiation treatment on tumor growth. Also, the low depth-of-penetration associated with NIR imaging limits the potential clinical applications for 800CW-1N11 F(ab')$_2$.

In an effort to generate a probe more useful for imaging tumors in human patients, I next tested the hypothesis that radiolabeled 1N11 F(ab')$_2$ could be used for PET imaging. Preliminary PET imaging studies with ^{64}Cu labeled bavituximab F(ab')$_2$ demonstrated high activity in both the liver and kidneys (unpublished data). The poor biodistribution of ^{64}Cu-bavituximab F(ab')$_2$ was attributed to transchelation of ^{64}Cu released from the DOTA ligand required for radiolabeling to copper-binding proteins such as Cu^{2+}/Zn^{2+} super oxide dismutase (SOD1).[219] Therefore, I chose to directly label 1N11 F(ab')$_2$ with ^{124}I instead of ^{64}Cu or ^{68}Ga, which also requires the use of a chelator (either DOTA or NOTA). ^{124}I-1N11 F(ab')$_2$ clearly imaged PC3 prostate tumors growing in mice

by 48 hr with low activity in the liver and kidneys. The biodistribution of ^{124}I-1N11 F(ab')$_2$ was in good agreement with that observed for 800CW-1N11 F(ab')$_2$. Unlike 800CW-1N11 F(ab')2, ^{124}I-1N11 F(ab')$_2$ did not allow clear imaging of tumors within 24 hr. This discrepancy may be explained by the divergent physics of optical and PET signal detection. In optical imaging, a laser is used to excite a fluophore which emits a photon in the exact location of the imaging agent. The photon, however, is subject to absorption as it passes through tissue. In PET imaging, the location of the imaging agent is less precisely represented because the emitted positrons travel a short distance before they annihilate with electrons and generate the gamma rays detected by the imager. Also, the gamma rays are not absorbed as they pass through tissue.[220] At 24 hr post-injection., the background signal may be higher for ^{124}I-1N11 F(ab')$_2$ than 800CW-1N11 F(ab')$_2$ while the tumor signal is lower (i.e. less concentrated) despite what are likely to be similar probe concentrations in each tissue in terms of %ID/g. Moreover, the lens aperture (f/stop) of the CCD camera used for optical imaging can be manipulated to optimize image sensitivity and depth-of-focus, which is not possible with a gamma detector.

Exposure of PS on tumor endothelium is characteristic of all tumor models so far examined and the results of the optical and PET imaging studies demonstrate the potential versatility of imaging agents based on 1N11 F(ab')$_2$. Two types of tumors that may stand to benefit the most from PET imaging with

1N11 F(ab')$_2$ are renal and brain carcinomas. ^{18}F-FDG PET has been shown to have both insufficient specificity and sensitivity to accurately identify renal masses and does not offer any advantage over standard imaging with CT.[221-222] Also, many molecularly targeted PET probes evaluated in preclinical studies exhibit high kidney uptake due to urinary excretion. ^{124}I-1N11 F(ab')$_2$ showed minimal background signals in the kidney and should be evaluated in an orthotopic mouse model of renal carcinoma. High glucose metabolism in normal cortical gray matter prevents the accurate identification of brain tumors with ^{18}F-FDG.[130] ^{124}I-1N11 F(ab')$_2$ demonstrated minimal background activity in the brain and we have already shown that 800CW-1N11 F(ab')$_2$ can be used to image gliomas. Therefore, a logical follow-up study would be to determine if ^{124}I-1N11 F(ab')$_2$ can be used for PET imaging of brain tumors growing in mice. Imaging agents that target PS exposed on tumor EC would be particularly attractive for brain tumor imaging because, unlike tracers that target biomarkers on the tumor cells, they would not have to cross the blood brain barrier.

1N11 F(ab')$_2$ compares favorably to other PS-targeting agents in terms of affinity and specificity, but still requires 24-48 hours for optimal imaging. Ideally, a physician should be able to inject a patient with an imaging agent and image the tumor within hours rather than days. Consequently, much of my thesis work was devoted to developing a imaging agent with a much lower molecular weight that an F(ab')$_2$ (MW = 110 kDa). Importantly, the agent also needed to not interact

with serum components (i.e. β2GP1) so that any residue not retained at the target site rapidly clears the circulation.

I started to research small peptides that could potentially be used to image PS in tumors. Ultimately, I chose to study a peptide that didn't bind to PS, but rather bound to PE, the other abundant aminophospholipid found in mammalian plasma membranes. Duramycin is attractive from an imaging standpoint because it possesses an unusually high affinity for a short peptide, it is resistant to degradation, is non-immunogenic, and has a short serum half-life.[106] Although PE had not been validated as a marker of tumor endothelium, duramycin had been studied to some extent by some of my predecessors in Dr. Thorpe's laboratory. Dr. Jin He conjugated duramycin to an IgG backbone and found that the construct inhibited the growth of Meth-A fibrosarcomas in mice (unpublished data). Dr. Andrei Marconescu used duramycin conjugated to flurophore-filled liposomes to show that PE becomes externalized on irradiated endothelial cells grown in culture.[100] Their data served as the foundation of a two-pronged hypothesis: 1) PE is a marker of tumor vasculature much like PS and 2) duramycin can be used for tumor imaging.

In an effort to design a PE-binding probe with a low molecular weight, I biotinylated duramycin and tested its ability to localize to tumor endothelium when injected into tumor bearing mice. Interestingly, I found that DLB only localized to tumor vasculature when co-injected with unmodified peptide.

Subsequently, I used DLB to demonstrate increased externalization of PE on tumor EC *in vivo* in several different mouse tumor models and that the mechanism for PE externalization was most likely related to hypoxia and other oxidative stress within the tumor microenvironment. Furthermore, I was able to image two different mouse models of prostate cancer using a NIR derivative of duramycin, 800CW-DUR [27] Thus, I believe the data presented in this dissertation support the hypothesis that PE is a tumor vascular marker that could be used as a target for imaging agents.

800CW-DUR effectively imaged tumors growing in mice, but more work needs to be done to fully evaluate the clinical potential of duramycin-based probes. I tested [^{64}Cu]DOTA-DUR for PET imaging of tumors, but observed high hepatic uptake of the probe. The biodistribution of [^{64}Cu]DOTA-DUR was similar to that reported for ^{3}H-duramycin and we hypothesized that the more favorable biodistribution reported for ^{99m}Tc-duramcyin was related to its negative charge. [106-107] Therefore, we labeled duramycin with 800CW, which is also strongly negatively charged and tested its pharmacokinetic properties. In support of our hypothesis, 800CW-DUR exhibited a similar biodistribution profile to ^{99m}Tc-duramcyin. It should be possible in future studies to radiolabel 800CW-DUR with isotopes used for PET. However, conjugation to 800CW also significantly increased the serum half-life of duramycin and tumors cannot be clearly delineated until 24 hr after injection of the probe. Any PET imaging

construct derived from 800CW-DUR would also suffer from a relatively slow blood clearance rate.

The high signal in the liver associated with [^{64}Cu]DOTA-DUR may not solely be related to charge, but also may be caused by transchelation of ^{64}Cu. An ethylene cross-bridged cyclam derivative 4,11-bis(carboxymethyl)-1,4,7,10 tetraazabicyclo[6.6.2]hexadecane (CB-TE2A) has been reported to have higher *in vivo* stability than DOTA.[159, 219, 223] CB-TE2A is more resistant to transchelation than DOTA because it forms an octahedral complex with 2 axial nitrogens, 2 equitoral nitrogens, and 2 cis-equatorial carboxylates all coordinating ^{64}Cu. DOTA, on the other hand, forms a distorted octahedron with 4 equatorial nitrogens and 2 weakly binding carboxylates coordinating ^{64}Cu (**Figure 5.1**).[219] Future studies are needed to determine if duramycin radiolabled with [^{64}Cu]CB-TE2A has a more favorable biodistribution than [^{64}Cu]DOTA-DUR. The advantages in cost, commercial availability, and decay scheme that ^{64}Cu has over ^{124}I suggest that 1N11 F(ab')$_2$ should also be derivatized with [^{64}Cu]CB-TE2A and evaluated in future experiments.

The fact that maximal PE binding of DLB and 800CW-DUR was only achieved when each probe was complexed with unmodified duramycin is another factor that may complicate the development of clinically useful duramycin-based imaging agents. Further experiments are needed to test the hypothesis that unmodified duramycin is disrupting endothelial membranes in the proximal and

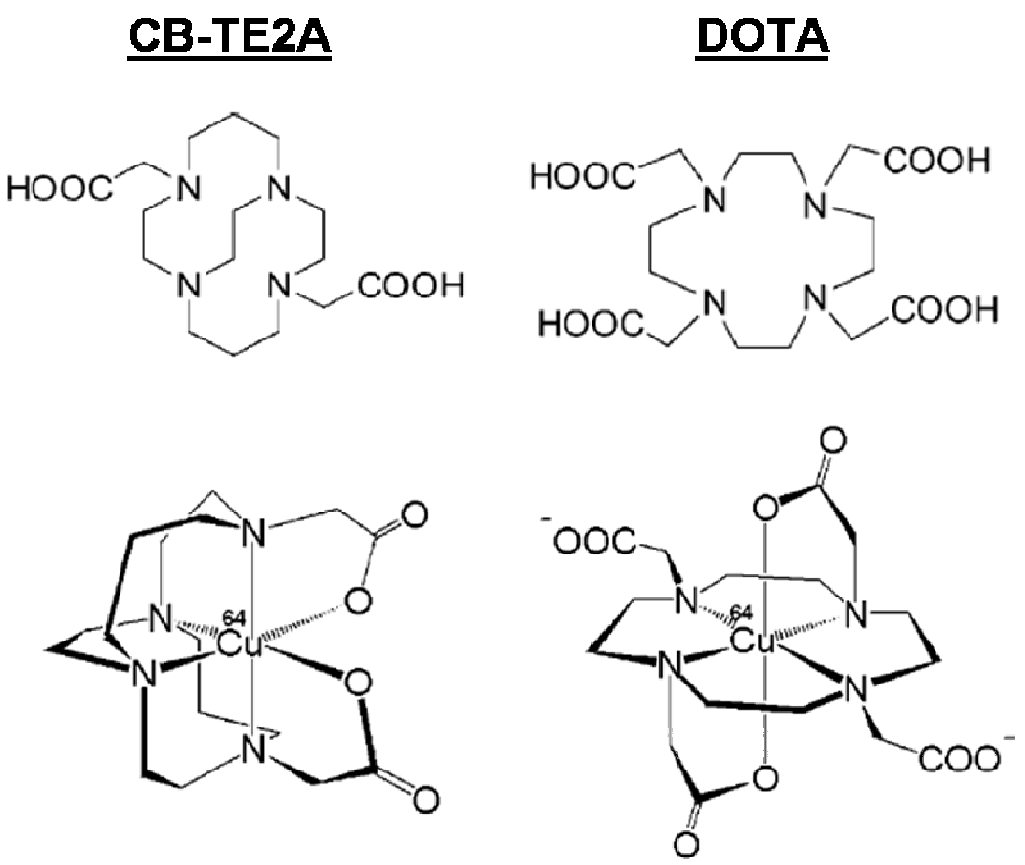

Figure 5.1. Structures of different chelators used for ^{64}Cu radiolabeling. The ethylene "cross-bridged" cyclam derivative CB-TE2A is less susceptible to transchelation than DOTA, a nonbridged tetramacrocyclic. (*adapted from Boswell et al., 2004*) [219]

distal collecting tubules and therefore causing high retention of DLB and 800CW-DUR in the kidney. An ideal duramycin-based imaging construct would demonstrate low cytotoxicity and allow complex formation between individual molecules of the construct, thereby eliminating the need for unmodified peptide. This strategy may be more attractive than using linker molecules to create multivalent duramycin constructs because the complex would only form in the presence of PE and unbound probe could clear the circulation at a faster rate

Imaging exposed aminophospholipids on tumor endothelium may not offer any advantage over standard imaging methods (e.g. ^{18}F-FDG-PET) for the early detection of primary or metastatic lesions. Even in large tumors, the total amount of exposed PS or PE can be relatively low compared to overexpressed tumor antigens that have been targeted for imaging including: the bombesin receptor, folate receptor, somatostatin receptor, EGFR, VEGFR, ER, CEA, PMSA, and $\alpha_v\beta_3$ integrin.[156, 159, 224-229]

Assessing tumor response to therapy is where PS and PE imaging agents are likely to have the greatest impact. Localization and imaging studies using a variety of animal models have consistently demonstrated increased binding of 1N11- and duramycin-based probes in tumors treated with radiation, chemotherapy and androgen deprivation therapy. I am currently conducting studies aimed at correlating tumor uptake of ^{124}I-1N11 F(ab')$_2$ and inhibition of tumor growth in tumors treated with each of these "conventional therapies". If

1N11- and/or duramycin-based probes are shown to predict the effect of standard treatments then they should also be evaluated for their ability to predict the effect of targeted drug therapies or immunotherapies. The development of novel targeted therapies has led to a rapid expansion in the number of cancer drugs undergoing clinical evaluation over the last ten years. However, the genotypic and phenotypic heterogeneity of human cancer frequently causes patients with similar tumor types to have markedly different responses to the same therapy.[230-231] Consequently, the majority of experimental drugs fail to demonstrate efficacy as they advance to Phase III trials.[232] Preclinical optical imaging studies using 800CW-1N11 F(ab')$_2$ or 800CW-DUR to test the efficacy of these drugs in animal tumor models could help to improve the design of downstream studies in humans. Early phase clinical trials are usually conducted in patients with late stage disease where antitumor therapies may be much less effective. In the clinic, PET imaging with aminophospholipid-targeting probes could guide physicians to abandon ineffective treatments earlier, allowing them to adopt alternative treatments at an earlier stage of disease.

CHAPTER 6

MATERIALS AND METHODS

CHAPTER 2 MATERIALS AND METHODS

Preparation of 1N11 F(ab')$_2$ fragments and labeling with IRDye800CW

The human monoclonal antibody 1N11 is produced under serum-free conditions by Peregrine Pharmaceuticals, Inc. (Tustin, CA). Aurexis is a human monoclonal antibody that binds to an irrelevant antigen (*S. aureus* clumping factor A) and was used as a negative control antibody. 1N11 and Aurexis F(ab')$_2$ fragments were generated by reacting antibodies with pepsin at a molar ratio of 1:130 (antibody:pepsin) for 1 h at 37ºC. F(ab')$_2$ fragments (MW = 110 kD) were purified by FPLC using an S-200 column (Pharmacia, Piscataway, NJ) and PBS running buffer. F(ab')$_2$ was then reacted with an N-hydroxysuccinimide ester derivative of IRDye 800CW (Li-COR, Lincoln, NE) at molar ratio of 1:10 (F(ab')$_2$:dye) for 2 h at room temperature. Unreacted dye was separated from the conjugate using a PD-10 desalting column (GE Healthcare, Uppsala, Sweden). Analyses of the final product, based on the absorbance of the dye at 778 nm and the absorbance of the F(ab')$_2$ at 280 nm, showed that it consisted of approximately 2 molecules of dye bound to each F(ab')$_2$ fragment. The products are referred to as 800CW-1N11 or 800CW-aurexis throughout this dissertation.

Glioma xenografts

All animal procedures were approved by the Institutional Animal Care and Use Committee of University of Texas Southwestern Medical Center.

Subcutaneous model

2×10^6 human U87MG glioma cells (ATCC, Manassas, VA, USA) in 100 µl serum-free medium containing 25% MatriGel (25%, BD Biosciences, San Jose, CA) were injected subcutaneously into the right thigh of anesthetized nude mice (n = 4; BALB/c nu/nu; Harlan, Indianapolis, IN). For radiation studies, gliomas were implanted into both thighs of the mice (n = 8).

Orthotopic implantation

A 1 cm long incision was made along the midline of the head of anesthetized nude mice (n = 4) to expose the skull. Using a high-speed drill, a 1 mm burr hole was made in the skull over the right hemisphere, anterior to the coronal fissure. About 10^5 U87 cells in 4 µl of PBS and Matrigel were injected directly into right caudal diencephalon 1.5 mm beneath the dura mater using a 32G Hamilton syringe. Usage of a 32G fine needle minimizes tissue damage. The burr hole was filled with bone wax and the scalp was closed with sutures.

Radiation treatment

When the subcutaneous tumors on both thighs reached ~ 5mm in diameter, a single dose of 12 Gy of irradiation was delivered to the tumors on the left thigh of anesthetized mice using a small animal irradiator (XRAD320, Precision X-ray, Inc. North Branford, CT) fitted with a variable collimator to generate a single adjustable collimated iso-dose beam of X-rays at a dose rate of 10 Gy/min. For the orthotopic gliomas, a single dose of 12 Gy of irradiation was delivered using a D-shaped collimator to the whole brain excluding the olfactory bulb.

Detection and quantification of PS exposure in vivo.

Mice bearing two thigh tumors were given a single dose of 12 Gy irradiation to the left tumor to induce PS exposure, as described above. Twenty-four hours later, 150 μg 1N11 or the control body Aurexis was injected *i.v.* and allowed to circulate for 4 h. The mice were anesthetized, exsanguinated, and perfused with heparinized saline. The tumors on both sides were removed and frozen for preparation of cryosections. Vascular endothelium was stained using a rat anti-mouse CD31 antibody (BD Biosciences, San Jose, CA) followed by Cy3-labeled goat anti-rat IgG. 1N11 or Aurexis was detected using biotinylated goat anti-human IgG conjugated to Cy2. Images were captured using a Coolsnap digital camera mounted on a Nikon microscope and analyzed with MetaVue software (Universal Imaging Corporation). Doubly labeled endothelial cells (i.e. CD31 positive/1N11 positive) were identified by yellow fluorescence on merged images. The

percentage of doubly positive vessels was calculated as follows: (mean number of yellow vessels per field/mean number of total vessels) × 100. Ten random 0.079-mm^2 fields were evaluated for each section.

In vivo Imaging

MRI

Orthotopic gliomas were examined by anatomic MRI using a 9.4T horizontal bore magnet with a Varian INOVA Unity system (Palo Alto, CA). Each mouse was maintained under general anesthesia (air and 2 % isoflurane). T_1- and T_2-weighted fast spin-echo multislice coronal images were acquired. T_1-weighted contrast enhanced images were acquired after *i.v.* bolus injection of the contrast agent Gd-DTPA-BMA (0.1 mmol/kg body weight; Omniscan^{TM}, Amersham Health Inc., Princeton, NJ) into a tail vein.

Near Infrared Fluorescence Imaging

When the subcutaneous tumors reached ~ 5 mm in diameter, *in vivo* fluorescence imaging was performed using a Maestro imaging system (CRI Inc. Woburn, MA). Each mouse was maintained under general anesthesia (air and 2 % isoflurane). NIR images were acquired before and at different times after administration of 800CW-1N11 or 800CW-Aurexis (2 nmol/mouse) via a tail vein. For the irradiated tumors, the NIR dye-labeled conjugates were injected 24 h after irradiation and imaging was carried out

periodically for 24 h. A set of filters specifically for NIR imaging (excitation, 671-705 nm; emission, 730-950 nm) was applied. Immediately after the last image at 24 h, mice were anesthetized and the scalp of the mouse was surgically reflected to expose the skull and a fluorescence image was acquired. For the orthotopic glioma bearing mice, the skull was further removed to expose both sides of the brain tissues and a last *in vivo* image was obtained. The whole surgical procedure and imaging was completed within 10 min under anesthesia and no obvious bleeding occurred.

Analysis of fluorescence imaging

Fluorescence images were processed with the Maestro software 2.8. The spectrum of background signal (peak emission ~ 770 nm) was first obtained from a mouse before the 800CW-antibody conjugate injection, while the spectrum of 800CW conjugates (peak emission ~ 800 nm) was detected from a solution of the dye in PBS (0.01 nmol/µl). The spectra were then imported and used to unmix the NIR dye signal from the background signal for both *in vivo* and *ex vivo* studies. The whole set of *in vivo* images of an individual mouse, obtained before and at various times after injection of the dye, was examined for quantification. A common ROI was based on the most obvious signal of the tumor 24 h after injection and was applied to both the tumor and normal tissue of each image. The total photon counts (counts/s) in identical ROI were compared to detect dynamic changes in signal intensity.

Ex vivo fluorescence imaging

Immediately after the last *in vivo* image, tumor-bearing mice were sacrificed and tumor tissues and thigh muscles were dissected. *Ex vivo* fluorescence imaging was performed using the Maestro imaging system.

Near infrared florescence microscopy

Immediately after *in vivo* imaging, tumor-bearing mice were sacrificed and tumor tissues were dissected out. The cryosections were immunostained with antibodies to the endothelial marker, CD31 (Serotec, Raleigh, NC) followed by Cy3-conjugated secondary antibody (Jackson Immunoresearch Laboratories, West Grove, PA). The NIR fluorescence signal was detected using a Zeiss AxioObserver (Carl Zeiss MicroImaging, Inc., Thornwood, NY) equipped with NIR filters. The NIR signals were recorded and merged with the CD31 image and the DAPI-stained image of the same field.

Statistical analysis

Statistical significance was assessed using an ANOVA on the basis of Fisher's protected least significant difference (PLSD; Statview; SAS Institute Inc., Cary, NC) or Student's t tests.

CHAPTER 3 MATERIALS AND METHODS

Materials

Iodine-124 (^{124}I) was obtained from IBA Molecular, Inc. (Richmond, VA). Iodine-125 (^{125}I) was obtained from Perkin Elmer (Waltham, MA). Pre-coated iodination tubes were purchased from Pierce Biotechnology (Rockford, IL). Instant thin-layer chromatography plates (ITLC-SG) were purchased from Pall Life Sciences (East Hills, NY). Dulbecco's modified Eagle's (DMEM) tissue culture medium, Roswell Park Memorial Institute (RPMI) 1640 tissue culture medium, Dulbecco phosphate buffered saline (PBS) containing Ca^{2+} and Mg^{2+}, glutamine and fetal bovine serum (FBS) were obtained from HyClone (Thermo Scientific, Logan, UT). F-12K tissue culture medium was purchased from Invitrogen (Grand Island, NY). Matrigel was purchased from BD Biosciences (Bedford, MA). Bio-Spin 6 gel filtration columns were purchased from Bio-Rad Laboratories (Hercules, CA). 96-well Immulon 1B microtiter plates were obtained from Thermo LabSystems (Franklin, MA). Phosphatidylserine (PS) was obtained from Avanti Polar Lipids (Alabaster, AL). Bovine serum albumin (BSA) was purchased from Sigma-Aldrich (St. Louis, MO). Furosemide was purchased from Sigma-Aldrich (St. Louis, MO).

Antibodies

The anti-PS antibody 1N11 was generated by Affitech A.S. (Oslo, Norway) in collaboration with Peregrine Pharmaceuticals, Inc. (Tustin, CA). For *in vitro* assays, 1N11 required 1:1 addition of human β2 glycoprotein to bind PS. Aurexis is a human monoclonal antibody that binds an irrelevant antigen *(S. aureus* clumping factor A) and was used as a negative control. Rat antimouse CD31 antibody was purchased from BD Biosciences (San Jose, CA). Goat antihuman immunoglobulin conjugated to Cy2 and goat antirat conjugated to Cy3 secondary antibodies were obtained from Jackson Immunoresearch Labs (West Grove, PA).

Preparation of $^{124/125}$I-1N11 F(ab')$_2$

F(ab')$_2$ fragments were generated by reacting antibodies with pepsin at a molar ratio of 1:130 (antibody:pepsin) for 1 h at 37ºC. F(ab')$_2$ fragments (MW = 110 kD) were purified by FPLC using an S-200 column *(*Pharmacia*,* Piscataway, NJ) and PBS running buffer. The F(ab')$_2$ fragments were then radioiodinated using the indirect IODO-GEN method (Pierce Biotechnology). Briefly, 1-3 mCi radioactive iodine was activated in 100 µl iodination buffer (125 mM Tris-HCL, pH 6.8, 150 mM NaCl) in a pre-coated iodination tube and then reacted with 0.2-0.6 mg F(ab')$_2$ in 100 µl iodination buffer in a separate uncoated tube. Free iodine was removed using Bio-Spin 6 gel filtration columns that were pre-blocked

with iodination buffer supplemented with 10% FBS. Radio-TLC analysis was used to determine radioiodination efficiency and was performed on a Rita Star Radioisotope TLC Analyzer (Straubenhardt, Germany) using ITLC-SG plates and PBS as the mobile phase.

Cells

PC3 human prostate carcinoma cells that express luciferase (PC3luc) and LNCaP human prostate carcinoma cells were obtained from American Type Cell Collection (Rockville, MD). Adult bovine aortic endothelial (ABAE) cells were obtained form Clonetics (Walkerville, MD). PC3 cells were maintained in F-12K media, LNCaP cells were maintained in RPMI media, and ABAE cells were maintained in DMEM media. All tissue culture media was supplemented with 10% FBS and 2 mM L-glutamine. Cells were trypsinized with 0.25% trypsin and 2.1 mM EDTA (Mediatech Inc., Manassus, VA).

Growth of s.c. Implanted Tumors

For localization and imaging studies, 2 x 10^6 PC3luc cells were injected into the right flank or 5 x 10^6 LNCaP cells were injected into the left flank of male athymic nu/nu mice (Charles River Fredrick, MD). Tumors were allowed to grow to a volume of 0.4-0.7 cm^3.

PS Competition ELISA

Phosphatidylserine (PS) was dissolved in *n*-hexane (10 µg/ml) and 50 µl of this solution was added to wells of Immulon 1B 96-well plates. The solvent was evaporated at room temperature (RT) and the plates were blocked for 1 h with 1% BSA dissolved in PBS. ^{125}I-1N11 F(ab')$_2$ and unlabeled PGN636 F(ab')$_2$ was diluted in blocking buffer at an initial concentration of 200 µg/ml and 2-fold dilutions were performed in a separate 96-well plates (100 µl per well). Biotinylated 1N11 (1N11-LB, 0.1 µg/ml) and β2GP (1 µg/ml) were then added to each well (final volume/well = 200 µl) and mixed. PS-coated plates were washed with PBS and F(ab')$_2$ mixtures (100 µl/well) were transferred from dilution plates to PS-coated plates. The plates were then incubated for 1 hr at RT. The plates were washed and bound 1N11-LB was detected using HRP-conjugated streptavidin (1:2000 in blocking buffer) and developed with the chromogenic substrate ODP. The plates were read at 490 nm using a microplate reader (BioTek Instruments, Winooski, VT).

Cell Binding Assay

ABAE and PC3 cells were cultured in 12-well tissue culture plates (BD Falcon, Bedford, MA) until approximately 80% confluent. To induce PS exposure cells were irradiated with 5 Gy 24 h prior to incubation with ^{124}I-PGN645 F(ab')$_2$. Untreated cells were used as a control. Cells were incubated

with 1 µg/ml ^{124}I-1N11 F(ab')$_2$ or control for 1 hr. The cells were then washed with PBS and digested with 1N NaOH (30 min). Activity from cell digests was measured using a calibrated γ-counter (Perkin Elmer, Waltham, MA).

In Vivo Biodistribution Studies

Tumor-bearing mice were injected intravenously (i.v.) with 50 µg, 50 µCi dose of ^{125}I-1N11 F(ab')$_2$. Animals were sacrificed at 24, 48 and 72 hr post-injection and tumors, blood, and other organs of interest were collected, weighed, and measured for activity using a γ-counter. ^{125}I-1N11 F(ab')$_2$ uptake in each organ was expressed as percentage injected dose per gram (%ID/g) and percentage injected dose per organ (%ID/organ) and represent the mean +/- SD of n = 3.

In Vivo Stability Test.

Non-tumor bearing mice were injected intravenously with either 50 µg, 50 µCi or 50 µg, 100 µCi doses of ^{124}I-1N11 F(ab')$_2$. Mice injected with 50 µCi were sacrificed at 1 hr and 24 hr post-injection (p.i.) and mice injected with 100 µCi were sacrificed at 48 hr p.i. Blood from the mice was collected, the erythrocytes were removed by centrifugation, and the serum was analyzed by high performance liquid chromatography (HPLC). HPLC analysis was performed using a Waters Biosuite 125 SEC column (300 x 7.8mm, 10 µm) and a Waters

600 Mulitsolvent Delivery System equipped with a Waters 2996 Photodiode Array (PDA) detector and in-line Shell Jr. 2000 radiodetector (Fredericksburg, VA). The mobile phase was PBS (pH = 7.2) at 1.0 ml/min flow rate.

Localization of 1N11 F(ab')$_2$ in Tumors

1N11 F(ab')$_2$ can bind PS in the outer or inner leaflet of cell membranes if directly applied to frozen tissue sections. To detect exposed PS on the surface of endothelial cells, 100 µg 1N11 F(ab')$_2$ was injected intravenously into tumor-bearing mice. Aurexis F(ab')$_2$ was used as a negative control. Sixty min. later, mice were sacrificed and perfused with heparinized saline as described previously.[233] To detect the exposed PS on cancer cells, the antibody was allowed to circulate for 4 hr to give it time to permeate into tumor masses. The tumor and major organs were removed, snap-frozen and cut into 10 µm cryosections. Sections were incubated overnight with rat antimouse CD31 antibody (1:200 in 1%BSA). Goat antirat Cy3 was used to detect the CD31 antibody. 1N11 F(ab')$_2$ was detected with goat antihuman Cy2. Cell nuclei were counterstained with DAPI.

PET Imaging of Tumors with ^{124}I-1N11 F(ab')$_2$

Tumor-bearing mice were imaged with a Siemens Inveon PET-CT Multimodality System (Siemens Medical Solutions Inc., Knoxville, TN). Thyroid

uptake of ^{124}I was blocked by adding 10 drops saturated KI per 100 ml of drinking water 24 hr prior to injection of ^{124}I-1N11 F(ab')$_2$. Stomach uptake was blocked by gastric lavage with 1.5 ml potassium perchlorate in 200 µl PBS 30 min before injection. The mice were injected via a tail vein with 50 µCi (1.8 MBq), 50 µg dose of ^{124}I-1N11 F(ab')$_2$ in 150 µl PBS. Mice bearing orthotopic tumors were injected intraperitoneally (i.p.) with 10 mg/kg furosemide and given 200 µl water by gastric lavage 1 hr prior to imaging to clear residual activity from the bladder. The mice were first anesthetized with 3% isoflurane until stable vital signs were established then placed on the imaging bed and imaged under 2% isoflurane anesthesia for the duration of the procedure. CT images were acquired at 80 kV and 500 µA and with a total scan time of approximately 6 min. CT images were reconstructed using COBRA Reconstruction Software. PET imaging was performed directly after acquisition of CT data. The scan time for PET images were between 10 and 20 min and the data was reconstructed using a Fourier Rebinning and Ordered Subsets Expectation Maximization 3D (OSEM3D) algorithm. Reconstructed CT and PET images were superimposed and analyzed using the Siemens Inveon Research Workplace (IRW) software. For quantification, tumor-margins were determined by CT morphology and regions of interest (ROIs) were defined manually.

CHAPTER 4 MATERIALS AND METHODS

Materials

Duramycin from *Streptoverticillium cinnamoneus*, bovine serum albumin (BSA), *o*-phenylenediamine dihydrochloride (ODP) and vascular endothelial growth factor (VEGF) were purchased from Sigma (St. Louis, MO). Sulfo-NHC-LC Biotin was obtained from Pierce (Rockford, IL). IRDye 800CW NHS Ester was obtained from LI-COR Biosciences (Lincoln, NE). Dulbecco's modified Eagle's (DMEM) tissue culture medium, Dulbecco phosphate buffered saline (PBS) containing Ca^{2+} and Mg^{2+}, glutamine and fetal bovine serum (FBS) were obtained from HyClone (Thermo Scientific, Logan, UT). Alexa Fluor 488-conjugated streptavidin, Alexa Fluor 350-conjugated streptavidin and Prolong Gold mounting media with DAPI were obtained from Molecular Probes (Invitrogen, Carlsbad, CA). Horseradish peroxidase-conjugated streptavidin and Cy3-conjugated streptavidin were purchased from Jackson ImmunoResearch Labs (West Grove, PA). Immulon 1B 96-well microtiter plates were obtained from Thermo LabSystems (Franklin, MA). LUMITRAC 96-well microtiter plates were obtained from Greiner Bio-One (Monroe, NC). Phosphatidylethanolamine (PE), phosphatidylcholine (PC), phosphatidylserine (PS), sphingomyelin (SM), phosphoinositol (PI), phosphatidic acid (PA) and phosphatidylglycerol (PG) were obtained from Avanti Polar Lipids (Alabaster, AL).

Antibodies

The anti-PS antibody bavituximab is produced under serum-free conditions by Peregrine Pharmaceuticals, Inc. (Tustin, CA). Bavituximab requires 1:1 addition of human β2 glycoprotein to bind PS. Rituxan is a human monoclonal antibody that binds human CD20 and was obtained from the UT Southwestern pharmacy. Rat anti-mouse CD31 antibody was purchased from BD Biosciences (San Jose, CA). Goat anti-human IgG conjugated to Cy2, goat anti-rat IgG conjugated to Cy3, and biotinylated goat anti-rat IgG secondary antibodies were obtained from Jackson Immunoresearch Labs (West Grove, PA).

Synthesis of duramycin conjugates and control peptides

Duramycin was reacted through its free amino groups with an N-hydroxysuccinimide (NHS) ester of a long chain (adipic) derivative of L-biotin at molar ratio of 1 : 1.1. Briefly, NHS-biotin in DMSO was rapidly mixed with duramycin in PBS. The reaction was allowed to proceed for 2 h. Unreacted biotin was removed by dialysis. The product corresponding to one molecule of duramycin linked to one molecule of biotin was purified by HPLC. Mass spectrometry confirmed a molecular mass of 2352 Da (Fig. 1A). The duramycin-L-biotin conjugate (DLB) was supplemented with an equal weight of unlabeled duramycin for all assays, as its addition strengthened PE binding. The control peptide linear duramycin (linDUR) was synthesized by Biosynthesis Inc.

(Lewisville, TX) and has the same sequence as duramycin except that thioether-linked amino acids were substituted with alanines. LinDUR was biotinylated to produce the control peptide linear-duramycin-L-biotin (linDLB). LinDLB was also supplemented with an equal weight of unlabeled duramycin for all assays.

Duramycin was reacted with the NHS ester of IRDye 800CW at a 1:1 molar ratio as described above. The product consisting of one molecule of duramycin linked to one molecule of 800CW was purified by HPLC. Mass spectrometry confirmed a molecular mass of 2998 Da (Fig. 1B). LinDUR reacted with IRDye 800CW produced the control peptide referred to as 800CW-linDUR. Both 800CW-DUR and 800CW-linDUR were supplemented with an equal weight of unlabeled duramycin for all assays.

Cells

Adult bovine aortic endothelial (ABAE) cells were obtained form Clonetics (Walkerville, MD). RM-1 mouse prostate carcinoma, RM-9 mouse prostate carcinoma, 4T1 mouse breast carcinoma, B16 mouse melanoma, and A549 human lung carcinoma cells were obtained from American Type Cell Collection (Rockville, MD). MDA-MB-231 human breast carcinoma cells were provided by Dr. Robert Kerbel (Sunnybrook Health Sciences Center, Toronto, Ontario, Canada). All cells were maintained in DMEM supplemented with 10%

FBS and 2 mM L-glutamine. Cells were trypsinized with 0.25% trypsin and 2.1 mM EDTA (Mediatech Inc., Manassus, VA).

Growth of s.c. implanted tumors

For localization studies, 10^6 RM-1, RM-9 or B16 cells were injected into the right hind flank of male C57BL/6 mice (UTSW breeding core). A549 cells (5 x 10^6 cells) were injected into the right hind flank of female athymic *nu/nu* mice (Charles River, Fredrick, MD). Tumors were allowed to grow to a volume of 0.7-1.0 cm^3.

Orthotopic MDA-MB-231 and 4T1 breast carcinoma models

Female *nu/nu* or SCID mice were purchased from Charles River. MDA-MB-231 or 4T1 cells (5 x 10^6) suspended in 0.1 ml were implanted into the mammary fat pad as described previously [234]. Briefly, mice were anesthetized and a 5 mm incision was made in the skin over the lateral thorax. The mammary fat pad was exposed to ensure the correct site of implantation and tumor cells were injected with a 25 gauge needle. The incision was closed with a wound clip that was removed 5-7 days later.

MMTV-PyMT transgenic mice

Mouse Mammary Tumor Virus (MMTV) promoter driven expression of polyoma middle T antigen (PyMT) results in mammary gland-specific adenocarcinoma formation [235]. Female MMTV-PyMT mice were obtained from the laboratory of Dr. Rolf Brekken at UT Southwestern Medical Center (Dallas, TX).

Radiation Treatment

Tumor-bearing mice were treated with a single dose of 5 Gy focal irradiation using a small animal irradiator (XRAD320, Precision X-ray, Inc. North Branford, CT). The irradiator was fitted with a variable collimator to generate a single adjustable collimated iso-dose beam of X-rays at a dose rate of 10 Gy/min.

Androgen Deprivation Therapy (ADT)

Androgen deprivation was achieved via castration. Briefly, tumor-bearing mice were anesthetized and an incision was made in the scrotum. A second incision was made in the tunica of the first testicle and the testis, vas deferens, and testicular fat pad was exposed. The testis was severed from the vas deferens and fat pad and the blood vessels supplying the testis were cauterized. The procedure was repeated for the testicle on the contralateral side and the scrotum incision was closed using wound clips.

Anti-phospholipid ELISAs

To test the binding of DLB and 800CW-DUR, phospholipids were dissolved in *n*-hexane (10 µg/ml) and 50 µl of this solution was added to wells of Immulon 1B or LUMITRAC 96-well plates. The solvent was evaporated at room temperature (RT) and the plates were blocked for 1 h with 5% FBS dissolved in PBS. DLB and 800CW-DUR were diluted in blocking buffer at an initial concentrations of 1 µg/ml and 10 µg/ml respectively and 2-fold dilutions were performed in a separate 96-well plates (100 µl per well). Phospholipid-coated plates were washed with PBS and DLB and 800CW-DUR were transferred from dilution plates to Immulon 1B and LUMITRAC plates respectively. The plates were incubated for 1 h at RT and then washed. Bound 800CW-DUR was detected using an Odyssey imaging system (LI-COR Biosciences, Lincoln, NE). Bound DLB was detected using HRP-conjugated streptavidin (1:2000 in blocking buffer) and ODP substrate. Optical density of ODP was read at 490 nm using a microplate reader (BioTek Instruments, Winooski, VT).

Hemolysis assay

Fresh mouse blood was treated with heparin (15 IU/ml) and centrifuges (300 x G, 5min) to sediment the red cells. After 3 washes, the red cells were resuspended in 10 x the original volume of blood. Duramycin or DLB were serially 2-fold-diluted in PBS in 100 µl volumes in 96-well round-bottomed

microplates. The red cell suspension (100 µl/well) was added. The plates were kept at room temperature for 1 h. Supernatants were removed and their absorbance was measured at 575 nm in an ELISA reader.

Immunohistochemical detection of exposed PE on the surface of cultured endothelial cells

ABAE cells were cultured in 8-well chamber slides (BD Falcon, Bedford, MA) until approximately 80% confluent. To induce PE exposure, cells were irradiated with 5 Gy 24 h prior to staining. Untreated cells were used as a control. Cells were incubated with DLB (0.5 µg/ml) dissolved in culture media. linDLB (0.5 µg/ml) was used as a negative control. Bavituximab (1 µg/ml) was used as a positive control for detection of PS. The cells were then washed with PBS and fixed with 4% paraformaldehyde for 10 min. Excess aldehyde groups were quenched with 50 mM ammonium chloride for 5 min. Biotinylated peptides were detected by incubating Alexa Fluor 488- or Cy3-conjugated streptavidin (1:1000 in 1% BSA) for 30 min. Cell membranes were permeablized with 0.5% TritonX-100 (5 min) and cytoskeletons were stained with Texas Red labeled phalloidin (1:200 in 1%BSA) (30 min). Cell nuclei were counterstained with DAPI.

Effect of ROS, hypoxia, pH and VEGF on PE exposure in cultured EC

For all treatments, ABAE cells were cultured in 75 cm^2 flasks (Corning Inc., Lowell, MA) until approximately 80% confluent. To mimic ROS in tumors, cells were treated with 10 µM H_2O_2 in serum free media for 1 h. To study the effect of hypoxia, flasks of cells were placed in a humidified normoxic atmosphere (21% O_2, 5% CO_2) for 48 h before being transferred to a humidified hypoxic atmosphere (1% O_2, 5% CO_2, 94% N_2) in a sealed chamber (Biospherix, Lacona, NY). The cells were incubated in the hypoxic chamber at 37°C for 24 h and were then returned to a normoxic environment for 4 h at 37°C. To study the effect of acidity, cells were incubated for 24 h in bicarbonate-free media adjusted to pH 5.8 with HCl at 37°C and in the absence of CO_2. Untreated cells from an identical passage were used as controls. After all treatments, cells were trypsinized for 1 min, washed and resuspended in ice cold FACS buffer (DPBS with 10% FBS and 0.02% NaN_3). To detect externalized PE, cells were incubated with DLB (0.5µg/ml) for 1 hour. linDLB (0.5 µg/ml each) was used as a negative control. Bavituximab (20 µg/ml) was used to detect exposed PS and rituxan (20 µg/ml) was used as a non-binding control for bavituximab. Cells were washed and bound peptides were detected with Alexa Fluor 488 conjugated-streptavidin (1:3000 in FACS buffer) and bound antibodies were detected with goat anti-human IgG-Cy2 (1:3000). Apoptotic cells were identified with

propidium iodide. The cells were analyzed with a FACScan flow cytometer (BD Biosciences).

Localization of duramycin peptides in tumor-bearing mice in vivo

To detect PE on the surface of EC, DLB (100 µg) was injected intravenously into tumor-bearing mice. Bavituximab (150 µg) and linDLB (100 µg) were used as positive and negative controls, respectively. The mice were killed after 60 min and perfused with heparinized saline as described previously.[233] The tumor and major organs were removed, snap-frozen and 10 µm cryosections were cut. Sections were incubated overnight with rat anti-mouse CD31 antibody (1:200 in 1% BSA). Goat anti-rat IgG-Cy3 was used to detect the CD31 antibody. DLB was detected with Alexa Fluor 488 conjugated-streptavidin. Bavituximab was detected with goat anti-human IgG-Cy2. Cell nuclei were counterstained with DAPI. PE-positive vessels were classified as DLB+, CD31+ co-stained structures having vascular endothelial cell morphology.

Detection of hypoxia in PE-positive tumors

100 µg DLB was injected intravenously into male C57Bl/6 mice bearing RM-9 tumors. Immediately afterward, 2 mg pimonidazole HCl (Hypoxyprobe-1 kit) was injected intraperitoneally. After 1 h, tumors were harvested and sections were prepared as described previously [233]. Sections were incubated overnight

with rat anti-mouse CD31 IgG antibody (1:200) and FITC-labeled antibody against the pimonidazole adduct (Hypoxyprobe kit) (1:50) in 1% BSA. The following day, sections were stained with saturating amounts of Cy3-conjugated streptavidin (1:500) to detect DLB. After washing, the sections were incubated with biotinylated goat anti-rat IgG (1:500) followed with Alexa Fluor 350-conjugated streptavidin (1:500) to detect the CD31 antibody. Immunohistochemical staining for pimonidazole adduct formation was also used to compare levels of hypoxia in similar-sized (1 cm diameter) RM-9 tumors and 4T1 tumors. For each tumor type, multiple fluorescent images were captured at low magnification (100X) and hypoxia staining was quantified using ImageJ software.

Imaging of tumors with 800CW-DUR

In vivo near-infrared fluorescence imaging was performed using a Xenogen IVIS Lumina imaging system (Xenogen, Alameda, CA). 800CW-DUR (50 µg) was injected into a tail vein in male mice bearing RM-9 tumors. 800CW-linDUR (50 µg) was used as a control. 24 h after injection, mice were anesthetized with 2% isoflurane (Halocarbon, North Augusta, SC) and images were obtained. Fluorescence (photons/s/cm^2/sr) was detected using the NIR filter set (excitation between 605-780 nm and emission between 810-885 nm).

REFERENCES

[1] Gorter E, and Grendel, F. (1924). On Biomolecular Layer of Lipoids on the Chromocytes of Blood. *Journal of Experimental Medicine* **41**, 439-443.

[2] Langmuir I (1917). THE CONSTITUTION AND FUNDAMENTAL PROPERTIES OF SOLIDS AND LIQUIDS. II. LIQUIDS. *Journal of the American Chemical Society* **39**, 1848-1906.

[3] Alberts B, Johnson, A., Lewis, J., Raff, M., Roberts, K. and Walter, P. (2002). Molecular Biology of the Cell. *Garland Science* **New York, NY**.

[4] Daleke DL (2003). Regulation of transbilayer plasma membrane phospholipid asymmetry. *J Lipid Res* **44**, 233-242.

[5] Gascard P, Tran D, Sauvage M, Sulpice JC, Fukami K, Takenawa T, Claret M, and Giraud F (1991). Asymmetric distribution of phosphoinositides and phosphatidic acid in the human erythrocyte membrane. *Biochimica et biophysica acta* **1069**, 27-36.

[6] Butikofer P, Lin ZW, Chiu DT, Lubin B, and Kuypers FA (1990). Transbilayer distribution and mobility of phosphatidylinositol in human red blood cells. *The Journal of biological chemistry* **265**, 16035-16038.

[7] Kornberg RD, and McConnell HM (1971). Inside-outside transitions of phospholipids in vesicle membranes. *Biochemistry* **10**, 1111-1120.

[8] Devaux PF (1992). Protein involvement in transmembrane lipid asymmetry. *Annual review of biophysics and biomolecular structure* **21**, 417-439.

[9] Bitbol M, Fellmann P, Zachowski A, and Devaux PF (1987). Ion regulation of phosphatidylserine and phosphatidylethanolamine outside-inside translocation in human erythrocytes. *Biochimica et biophysica acta* **904**, 268-282.

[10] Mombers C, Verkleij AJ, de Gier J, and van Deenen LL (1979). The interaction of spectrin-actin and synthetic phospholipids. II. The interaction with phosphatidylserine. *Biochimica et biophysica acta* **551**, 271-281.

[11] Cohen AM, Liu SC, Lawler J, Derick L, and Palek J (1988). Identification of the protein 4.1 binding site to phosphatidylserine vesicles. *Biochemistry* **27**, 614-619.

[12] Thorpe PE (2010). Targeting anionic phospholipids on tumor blood vessels and tumor cells. *Thromb Res* **125 Suppl 2**, S134-137.

[13] Miyanishi M, Tada K, Koike M, Uchiyama Y, Kitamura T, and Nagata S (2007). Identification of Tim4 as a phosphatidylserine receptor. *Nature* **450**, 435-439.

[14] Calderon C, Huang ZH, Gage DA, Sotomayor EM, and Lopez DM (1994). Isolation of a nitric oxide inhibitor from mammary tumor cells and its characterization as phosphatidyl serine. *J Exp Med* **180**, 945-958.

[15] Kim R, Emi M, Tanabe K, and Arihiro K (2006). Tumor-driven evolution of immunosuppressive networks during malignant progression. *Cancer research* **66**, 5527-5536.

[16] Zwaal RF, Comfurius P, and Bevers EM (2005). Surface exposure of phosphatidylserine in pathological cells. *Cell Mol Life Sci* **62**, 971-988.

[17] Bitbol M, and Devaux PF (1988). Measurement of outward translocation of phospholipids across human erythrocyte membrane. *Proceedings of the National Academy of Sciences of the United States of America* **85**, 6783-6787.

[18] Hamon Y, Broccardo C, Chambenoit O, Luciani MF, Toti F, Chaslin S, Freyssinet JM, Devaux PF, McNeish J, Marguet D*, et al.* (2000). ABC1 promotes engulfment of apoptotic cells and transbilayer redistribution of phosphatidylserine. *Nat Cell Biol* **2**, 399-406.

[19] Hamon Y, Luciani MF, Becq F, Verrier B, Rubartelli A, and Chimini G (1997). Interleukin-1beta secretion is impaired by inhibitors of the Atp binding cassette transporter, ABC1. *Blood* **90**, 2911-2915.

[20] Bevers EM, and Williamson PL (2010). Phospholipid scramblase: an update. *FEBS Lett* **584**, 2724-2730.

[21] Ran S, Downes A, and Thorpe PE (2002). Increased exposure of anionic phospholipids on the surface of tumor blood vessels. *Cancer research* **62**, 6132-6140.

[22] Ran S, He J, Huang X, Soares M, Scothorn D, and Thorpe PE (2005). Antitumor effects of a monoclonal antibody that binds anionic phospholipids on the surface of tumor blood vessels in mice. *Clin Cancer Res* **11**, 1551-1562.

[23] He J, Luster TA, and Thorpe PE (2007). Radiation-enhanced vascular targeting of human lung cancers in mice with a monoclonal antibody that binds anionic phospholipids. *Clin Cancer Res* **13**, 5211-5218.

[24] He J, Yin Y, Luster TA, Watkins L, and Thorpe PE (2009). Antiphosphatidylserine antibody combined with irradiation damages tumor blood vessels and induces tumor immunity in a rat model of glioblastoma. *Clin Cancer Res* **15**, 6871-6880.

[25] Huang X, Bennett M, and Thorpe PE (2005). A monoclonal antibody that binds anionic phospholipids on tumor blood vessels enhances the antitumor effect of docetaxel on human breast tumors in mice. *Cancer research* **65**, 4408-4416.

[26] Jennewein M, Lewis MA, Zhao D, Tsyganov E, Slavine N, He J, Watkins L, Kodibagkar VD, O'Kelly S, Kulkarni P*, et al.* (2008). Vascular

imaging of solid tumors in rats with a radioactive arsenic-labeled antibody that binds exposed phosphatidylserine. *Clin Cancer Res* **14**, 1377-1385.

[27] Stafford JH, and Thorpe PE (2011). Increased exposure of phosphatidylethanolamine on the surface of tumor vascular endothelium. *Neoplasia (New York, N.Y* **13**, 299-308.

[28] Jain RK (2005). Normalization of tumor vasculature: an emerging concept in antiangiogenic therapy. *Science* **307**, 58-62.

[29] Lopez-Lazaro M (2008). The warburg effect: why and how do cancer cells activate glycolysis in the presence of oxygen? *Anticancer Agents Med Chem* **8**, 305-312.

[30] Bae YS, Kang SW, Seo MS, Baines IC, Tekle E, Chock PB, and Rhee SG (1997). Epidermal growth factor (EGF)-induced generation of hydrogen peroxide. Role in EGF receptor-mediated tyrosine phosphorylation. *J Biol Chem* **272**, 217-221.

[31] Zulueta JJ, Yu FS, Hertig IA, Thannickal VJ, and Hassoun PM (1995). Release of hydrogen peroxide in response to hypoxia-reoxygenation: role of an NAD(P)H oxidase-like enzyme in endothelial cell plasma membrane. *American journal of respiratory cell and molecular biology* **12**, 41-49.

[32] Szatrowski TP, and Nathan CF (1991). Production of large amounts of hydrogen peroxide by human tumor cells. *Cancer research* **51**, 794-798.

[33] Storz P (2005). Reactive oxygen species in tumor progression. *Front Biosci* **10**, 1881-1896.

[34] Emonds KM, Swinnen JV, Mortelmans L, and Mottaghy FM (2009). Molecular imaging of prostate cancer. *Methods* **48**, 193-199.

[35] Kolesnick RN, and Kronke M (1998). Regulation of ceramide production and apoptosis. *Annu Rev Physiol* **60**, 643-665.

[36] Mathias S, Pena LA, and Kolesnick RN (1998). Signal transduction of stress via ceramide. *Biochem J* **335 (Pt 3)**, 465-480.

[37] Taniguchi Y, Ohba T, Miyata H, and Ohki K (2006). Rapid phase change of lipid microdomains in giant vesicles induced by conversion of sphingomyelin to ceramide. *Biochim Biophys Acta* **1758**, 145-153.

[38] Marathe S, Schissel SL, Yellin MJ, Beatini N, Mintzer R, Williams KJ, and Tabas I (1998). Human vascular endothelial cells are a rich and regulatable source of secretory sphingomyelinase. Implications for early atherogenesis and ceramide-mediated cell signaling. *The Journal of biological chemistry* **273**, 4081-4088.

[39] Utsugi T, Schroit AJ, Connor J, Bucana CD, and Fidler IJ (1991). Elevated expression of phosphatidylserine in the outer membrane leaflet of human tumor cells and recognition by activated human blood monocytes. *Cancer research* **51**, 3062-3066.

[40] Rao LV, Tait JF, and Hoang AD (1992). Binding of annexin V to a human ovarian carcinoma cell line (OC-2008). Contrasting effects on cell surface factor VIIa/tissue factor activity and prothrombinase activity. *Thromb Res* **67**, 517-531.

[41] Woehlecke H, Pohl A, Alder-Baerens N, Lage H, and Herrmann A (2003). Enhanced exposure of phosphatidylserine in human gastric carcinoma cells overexpressing the half-size ABC transporter BCRP (ABCG2). *Biochem J* **376**, 489-495.

[42] Kirszberg C, Lima LG, Da Silva de Oliveira A, Pickering W, Gray E, Barrowcliffe TW, Rumjanek VM, and Monteiro RQ (2009). Simultaneous tissue factor expression and phosphatidylserine exposure account for the highly procoagulant pattern of melanoma cell lines. *Melanoma Res* **19**, 301-308.

[43] Connor J, Bucana C, Fidler IJ, and Schroit AJ (1989). Differentiation-dependent expression of phosphatidylserine in mammalian plasma membranes: quantitative assessment of outer-leaflet lipid by prothrombinase complex formation. *Proceedings of the National Academy of Sciences of the United States of America* **86**, 3184-3188.

[44] Riedl S, Zweytick D, and Lohner K (2011). Membrane-active host defense peptides - Challenges and perspectives for the development of novel anticancer drugs. *Chem Phys Lipids*.

[45] Riedl S, Rinner B, Asslaber M, Schaider H, Walzer S, Novak A, Lohner K, and Zweytick D (2011). In search of a novel target - phosphatidylserine exposed by non-apoptotic tumor cells and metastases of malignancies with poor treatment efficacy. *Biochimica et biophysica acta* **1808**, 2638-2645.

[46] Simpson RJ, Lim JW, Moritz RL, and Mathivanan S (2009). Exosomes: proteomic insights and diagnostic potential. *Expert Rev Proteomics* **6**, 267-283.

[47] Cheng X, and Lopez DM (1998). CD4+, but not CD8+, T cells from mammary tumor-bearing mice have a down-regulated production of IFN-gamma: role of phosphatidyl serine. *J Immunol* **160**, 2735-2741.

[48] Papo N, Seger D, Makovitzki A, Kalchenko V, Eshhar Z, Degani H, and Shai Y (2006). Inhibition of tumor growth and elimination of multiple metastases in human prostate and breast xenografts by systemic inoculation of a host defense-like lytic peptide. *Cancer research* **66**, 5371-5378.

[49] Miller AB, Hoogstraten B, Staquet M, and Winkler A (1981). Reporting results of cancer treatment. *Cancer* **47**, 207-214.

[50] Vangestel C, Peeters M, Mees G, Oltenfreiter R, Boersma HH, Elsinga PH, Reutelingsperger C, Van Damme N, De Spiegeleer B, and Van de

Wiele C (2011). In Vivo Imaging of Apoptosis in Oncology: An Update. *Mol Imaging*.

[51] Cederholm A, and Frostegard J (2007). Annexin A5 as a novel player in prevention of atherothrombosis in SLE and in the general population. *Ann N Y Acad Sci* **1108**, 96-103.

[52] Blankenberg FG, Katsikis PD, Tait JF, Davis RE, Naumovski L, Ohtsuki K, Kopiwoda S, Abrams MJ, Darkes M, Robbins RC*, et al.* (1998). In vivo detection and imaging of phosphatidylserine expression during programmed cell death. *Proceedings of the National Academy of Sciences of the United States of America* **95**, 6349-6354.

[53] Blankenberg F (2002). To scan or not to scan, it is a question of timing: technetium-99m-annexin V radionuclide imaging assessment of treatment efficacy after one course of chemotherapy. *Clin Cancer Res* **8**, 2757-2758.

[54] Guo MF, Zhao Y, Tian R, Li L, Guo L, Xu F, Liu YM, He YB, Bai S, and Wang J (2009). In vivo99mTc-HYNIC-annexin V imaging of early tumor apoptosis in mice after single dose irradiation. *J Exp Clin Cancer Res* **28**, 136.

[55] Kemerink GJ, Liu X, Kieffer D, Ceyssens S, Mortelmans L, Verbruggen AM, Steinmetz ND, Vanderheyden JL, Green AM, and Verbeke K (2003). Safety, biodistribution, and dosimetry of 99mTc-HYNIC-annexin V, a novel human recombinant annexin V for human application. *J Nucl Med* **44**, 947-952.

[56] Vermeersch H, Loose D, Lahorte C, Mervillie K, Dierckx R, Steinmetz N, Vanderheyden JL, Cuvelier C, Slegers G, and Van de Wiele C (2004). 99mTc-HYNIC Annexin-V imaging of primary head and neck carcinoma. *Nucl Med Commun* **25**, 259-263.

[57] Kartachova M, van Zandwijk N, Burgers S, van Tinteren H, Verheij M, and Valdes Olmos RA (2007). Prognostic significance of 99mTc Hynic-rh-annexin V scintigraphy during platinum-based chemotherapy in advanced lung cancer. *J Clin Oncol* **25**, 2534-2539.

[58] Kartachova M, Haas RL, Olmos RA, Hoebers FJ, van Zandwijk N, and Verheij M (2004). In vivo imaging of apoptosis by 99mTc-Annexin V scintigraphy: visual analysis in relation to treatment response. *Radiother Oncol* **72**, 333-339.

[59] Kartachova MS, Valdes Olmos RA, Haas RL, Hoebers FJ, van Herk M, and Verheij M (2008). 99mTc-HYNIC-rh-annexin-V scintigraphy: visual and quantitative evaluation of early treatment-induced apoptosis to predict treatment outcome. *Nucl Med Commun* **29**, 39-44.

[60] Vanderheyden JL, Liu G, He J, Patel B, Tait JF, and Hnatowich DJ (2006). Evaluation of 99mTc-MAG3-annexin V: influence of the chelate

on in vitro and in vivo properties in mice. *Nuclear medicine and biology* **33**, 135-144.

[61] Kurihara H, Yang DJ, Cristofanilli M, Erwin WD, Yu DF, Kohanim S, Mendez R, and Kim EE (2008). Imaging and dosimetry of 99mTc EC annexin V: preliminary clinical study targeting apoptosis in breast tumors. *Appl Radiat Isot* **66**, 1175-1182.

[62] Kemerink GJ, Boersma HH, Thimister PW, Hofstra L, Liem IH, Pakbiers MT, Janssen D, Reutelingsperger CP, and Heidendal GA (2001). Biodistribution and dosimetry of 99mTc-BTAP-annexin-V in humans. *Eur J Nucl Med* **28**, 1373-1378.

[63] Boersma HH, Liem IH, Kemerink GJ, Thimister PW, Hofstra L, Stolk LM, van Heerde WL, Pakbiers MT, Janssen D, Beysens AJ*, et al.* (2003). Comparison between human pharmacokinetics and imaging properties of two conjugation methods for 99mTc-annexin A5. *Br J Radiol* **76**, 553-560.

[64] Belhocine T, Steinmetz N, Green A, and Rigo P (2003). In vivo imaging of chemotherapy-induced apoptosis in human cancers. *Ann N Y Acad Sci* **1010**, 525-529.

[65] Belhocine T, Steinmetz N, Hustinx R, Bartsch P, Jerusalem G, Seidel L, Rigo P, and Green A (2002). Increased uptake of the apoptosis-imaging agent (99m)Tc recombinant human Annexin V in human tumors after one course of chemotherapy as a predictor of tumor response and patient prognosis. *Clin Cancer Res* **8**, 2766-2774.

[66] Yagle KJ, Eary JF, Tait JF, Grierson JR, Link JM, Lewellen B, Gibson DF, and Krohn KA (2005). Evaluation of 18F-annexin V as a PET imaging agent in an animal model of apoptosis. *J Nucl Med* **46**, 658-666.

[67] Toretsky J, Levenson A, Weinberg IN, Tait JF, Uren A, and Mease RC (2004). Preparation of F-18 labeled annexin V: a potential PET radiopharmaceutical for imaging cell death. *Nuclear medicine and biology* **31**, 747-752.

[68] Cauchon N, Langlois R, Rousseau JA, Tessier G, Cadorette J, Lecomte R, Hunting DJ, Pavan RA, Zeisler SK, and van Lier JE (2007). PET imaging of apoptosis with (64)Cu-labeled streptavidin following pretargeting of phosphatidylserine with biotinylated annexin-V. *European journal of nuclear medicine and molecular imaging* **34**, 247-258.

[69] Glaser M, Collingridge DR, Aboagye EO, Bouchier-Hayes L, Hutchinson OC, Martin SJ, Price P, Brady F, and Luthra SK (2003). Iodine-124 labelled annexin-V as a potential radiotracer to study apoptosis using positron emission tomography. *Appl Radiat Isot* **58**, 55-62.

[70] Collingridge DR, Glaser M, Osman S, Barthel H, Hutchinson OC, Luthra SK, Brady F, Bouchier-Hayes L, Martin SJ, Workman P*, et al.* (2003). In

vitro selectivity, in vivo biodistribution and tumour uptake of annexin V radiolabelled with a positron emitting radioisotope. *Br J Cancer* **89**, 1327-1333.

[71] Dekker B, Keen H, Lyons S, Disley L, Hastings D, Reader A, Ottewell P, Watson A, and Zweit J (2005). MBP-annexin V radiolabeled directly with iodine-124 can be used to image apoptosis in vivo using PET. *Nuclear medicine and biology* **32**, 241-252.

[72] Petrovsky A, Schellenberger E, Josephson L, Weissleder R, and Bogdanov A, Jr. (2003). Near-infrared fluorescent imaging of tumor apoptosis. *Cancer research* **63**, 1936-1942.

[73] Schellenberger EA, Bogdanov A, Jr., Petrovsky A, Ntziachristos V, Weissleder R, and Josephson L (2003). Optical imaging of apoptosis as a biomarker of tumor response to chemotherapy. *Neoplasia* **5**, 187-192.

[74] Ntziachristos V, Schellenberger EA, Ripoll J, Yessayan D, Graves E, Bogdanov A, Jr., Josephson L, and Weissleder R (2004). Visualization of antitumor treatment by means of fluorescence molecular tomography with an annexin V-Cy5.5 conjugate. *Proceedings of the National Academy of Sciences of the United States of America* **101**, 12294-12299.

[75] Schellenberger EA, Bogdanov A, Jr., Hogemann D, Tait J, Weissleder R, and Josephson L (2002). Annexin V-CLIO: a nanoparticle for detecting apoptosis by MRI. *Mol Imaging* **1**, 102-107.

[76] Sosnovik DE, Schellenberger EA, Nahrendorf M, Novikov MS, Matsui T, Dai G, Reynolds F, Grazette L, Rosenzweig A, Weissleder R*, et al.* (2005). Magnetic resonance imaging of cardiomyocyte apoptosis with a novel magneto-optical nanoparticle. *Magn Reson Med* **54**, 718-724.

[77] Zhao M, Beauregard DA, Loizou L, Davletov B, and Brindle KM (2001). Non-invasive detection of apoptosis using magnetic resonance imaging and a targeted contrast agent. *Nat Med* **7**, 1241-1244.

[78] Krishnan AS, Neves AA, de Backer MM, Hu DE, Davletov B, Kettunen MI, and Brindle KM (2008). Detection of cell death in tumors by using MR imaging and a gadolinium-based targeted contrast agent. *Radiology* **246**, 854-862.

[79] Wang F, Fang W, Zhao M, Wang Z, Ji S, Li Y, and Zheng Y (2008). Imaging paclitaxel (chemotherapy)-induced tumor apoptosis with 99mTc C2A, a domain of synaptotagmin I: a preliminary study. *Nuclear medicine and biology* **35**, 359-364.

[80] Wang F, Fang W, Zhang MR, Zhao M, Liu B, Wang Z, Hua Z, Yang M, Kumata K, Hatori A*, et al.* (2011). Evaluation of Chemotherapy Response in VX2 Rabbit Lung Cancer with 18F-Labeled C2A Domain of Synaptotagmin I. *J Nucl Med* **52**, 592-599.

[81] Andersen MH, Graversen H, Fedosov SN, Petersen TE, and Rasmussen JT (2000). Functional analyses of two cellular binding domains of bovine lactadherin. *Biochemistry* **39**, 6200-6206.

[82] Falborg L, Waehrens LN, Alsner J, Bluhme H, Frokiaer J, Heegaard CW, Horsman MR, Rasmussen JT, and Rehling M (2010). Biodistribution of 99mTc-HYNIC-lactadherin in mice--a potential tracer for visualizing apoptosis in vivo. *Scand J Clin Lab Invest* **70**, 209-216.

[83] Thapa N, Kim S, So IS, Lee BH, Kwon IC, Choi K, and Kim IS (2008). Discovery of a phosphatidylserine-recognizing peptide and its utility in molecular imaging of tumour apoptosis. *J Cell Mol Med* **12**, 1649-1660.

[84] Xiong C, Brewer K, Song S, Zhang R, Lu W, Wen X, and Li C (2011). Peptide-based imaging agents targeting phosphatidylserine for the detection of apoptosis. *J Med Chem* **54**, 1825-1835.

[85] Grimberg H, Levin G, Shirvan A, Cohen A, Yogev-Falach M, Reshef A, and Ziv I (2009). Monitoring of tumor response to chemotherapy in vivo by a novel small-molecule detector of apoptosis. *Apoptosis* **14**, 257-267.

[86] Reshef A, Shirvan A, Akselrod-Ballin A, Wall A, and Ziv I (2010). Small-molecule biomarkers for clinical PET imaging of apoptosis. *J Nucl Med* **51**, 837-840.

[87] Smith BA, Akers WJ, Leevy WM, Lampkins AJ, Xiao S, Wolter W, Suckow MA, Achilefu S, and Smith BD (2010). Optical imaging of mammary and prostate tumors in living animals using a synthetic near infrared zinc(II)-dipicolylamine probe for anionic cell surfaces. *J Am Chem Soc* **132**, 67-69.

[88] Luster TA, He J, Huang X, Maiti SN, Schroit AJ, de Groot PG, and Thorpe PE (2006). Plasma protein beta-2-glycoprotein 1 mediates interaction between the anti-tumor monoclonal antibody 3G4 and anionic phospholipids on endothelial cells. *The Journal of biological chemistry* **281**, 29863-29871.

[89] Steinkasserer A, Estaller C, Weiss EH, Sim RB, and Day AJ (1991). Complete nucleotide and deduced amino acid sequence of human beta 2-glycoprotein I. *Biochem J* **277 (Pt 2)**, 387-391.

[90] Yin Y, Kavlie K, and Thorpe PE (2009) in *100th AACR* (Proc. Am. Assoc. Cancer Res., Denver, CO), p. 5463.

[91] Hanshaw RG, and Smith BD (2005). New reagents for phosphatidylserine recognition and detection of apoptosis. *Bioorg Med Chem* **13**, 5035-5042.

[92] Schutters K, and Reutelingsperger C (2010). Phosphatidylserine targeting for diagnosis and treatment of human diseases. *Apoptosis* **15**, 1072-1082.

[93] Agar C, van Os GM, Morgelin M, Sprenger RR, Marquart JA, Urbanus RT, Derksen RH, Meijers JC, and de Groot PG (2010). Beta2-glycoprotein

I can exist in 2 conformations: implications for our understanding of the antiphospholipid syndrome. *Blood* **116**, 1336-1343.

[94] Brambell FW, Halliday R, and Morris IG (1958). Interference by human and bovine serum and serum protein fractions with the absorption of antibodies by suckling rats and mice. *Proc R Soc Lond B Biol Sci* **149**, 1-11.

[95] Junghans RP, and Anderson CL (1996). The protection receptor for IgG catabolism is the beta2-microglobulin-containing neonatal intestinal transport receptor. *Proceedings of the National Academy of Sciences of the United States of America* **93**, 5512-5516.

[96] Israel EJ, Wilsker DF, Hayes KC, Schoenfeld D, and Simister NE (1996). Increased clearance of IgG in mice that lack beta 2-microglobulin: possible protective role of FcRn. *Immunology* **89**, 573-578.

[97] Wahl RL, Parker CW, and Philpott GW (1983). Improved radioimaging and tumor localization with monoclonal F(ab')2. *J Nucl Med* **24**, 316-325.

[98] Covell DG, Barbet J, Holton OD, Black CD, Parker RJ, and Weinstein JN (1986). Pharmacokinetics of monoclonal immunoglobulin G1, F(ab')2, and Fab' in mice. *Cancer research* **46**, 3969-3978.

[99] Emoto K, Toyama-Sorimachi N, Karasuyama H, Inoue K, and Umeda M (1997). Exposure of phosphatidylethanolamine on the surface of apoptotic cells. *Exp Cell Res* **232**, 430-434.

[100] Marconescu A, and Thorpe PE (2008). Coincident exposure of phosphatidylethanolamine and anionic phospholipids on the surface of irradiated cells. *Biochimica et biophysica acta* **1778**, 2217-2224.

[101] Iwamoto K, Hayakawa T, Murate M, Makino A, Ito K, Fujisawa T, and Kobayashi T (2007). Curvature-dependent recognition of ethanolamine phospholipids by duramycin and cinnamycin. *Biophys J* **93**, 1608-1619.

[102] Wakamatsu K, Choung SY, Kobayashi T, Inoue K, Higashijima T, and Miyazawa T (1990). Complex formation of peptide antibiotic Ro09-0198 with lysophosphatidylethanolamine: 1H NMR analyses in dimethyl sulfoxide solution. *Biochemistry* **29**, 113-118.

[103] Zhao M (2009). Lantibiotics as probes for phosphatidylethanolamine. *Amino Acids*.

[104] Zimmermann N, Freund S, Fredenhagen A, and Jung G (1993). Solution structures of the lantibiotics duramycin B and C. *European journal of biochemistry / FEBS* **216**, 419-428.

[105] Navarro J, Chabot J, Sherrill K, Aneja R, Zahler SA, and Racker E (1985). Interaction of duramycin with artificial and natural membranes. *Biochemistry* **24**, 4645-4650.

[106] Zhao M, Li Z, and Bugenhagen S (2008). 99mTc-labeled duramycin as a novel phosphatidylethanolamine-binding molecular probe. *J Nucl Med* **49**, 1345-1352.

[107] McNulty MJ, Hutabarat RH, Findlay JW, Devereux K, Knick VC, Harvey RJ, and Molina L (2003). Pharmacokinetics and tissue distribution of the nonadecapeptide Moli1901 in rats and mice. *Xenobiotica; the fate of foreign compounds in biological systems* **33**, 197-210.

[108] Klaassen CD, and Aleksunes LM (2010). Xenobiotic, bile acid, and cholesterol transporters: function and regulation. *Pharmacol Rev* **62**, 1-96.

[109] Cloutier MM, Guernsey L, Mattes P, and Koeppen B (1990). Duramycin enhances chloride secretion in airway epithelium. *Am J Physiol* **259**, C450-454.

[110] Sheth TR, Henderson RM, Hladky SB, and Cuthbert AW (1992). Ion channel formation by duramycin. *Biochimica et biophysica acta* **1107**, 179-185.

[111] Zeitlin PL, Boyle MP, Guggino WB, and Molina L (2004). A phase I trial of intranasal Moli1901 for cystic fibrosis. *Chest* **125**, 143-149.

[112] Willmann JK, van Bruggen N, Dinkelborg LM, and Gambhir SS (2008). Molecular imaging in drug development. *Nat Rev Drug Discov* **7**, 591-607.

[113] Achilefu S (2004). Lighting up tumors with receptor-specific optical molecular probes. *Technol Cancer Res Treat* **3**, 393-409.

[114] Hadjipanayis CG, Jiang H, Roberts DW, and Yang L (2011). Current and future clinical applications for optical imaging of cancer: from intraoperative surgical guidance to cancer screening. *Semin Oncol* **38**, 109-118.

[115] Intes X, Ripoll J, Chen Y, Nioka S, Yodh AG, and Chance B (2003). In vivo continuous-wave optical breast imaging enhanced with Indocyanine Green. *Med Phys* **30**, 1039-1047.

[116] Alacam B, Yazici B, Intes X, Nioka S, and Chance B (2008). Pharmacokinetic-rate images of indocyanine green for breast tumors using near-infrared optical methods. *Phys Med Biol* **53**, 837-859.

[117] Gurfinkel M, Thompson AB, Ralston W, Troy TL, Moore AL, Moore TA, Gust JD, Tatman D, Reynolds JS, Muggenburg B*, et al.* (2000). Pharmacokinetics of ICG and HPPH-car for the detection of normal and tumor tissue using fluorescence, near-infrared reflectance imaging: a case study. *Photochem Photobiol* **72**, 94-102.

[118] Cheng Z, Wu Y, Xiong Z, Gambhir SS, and Chen X (2005). Near-infrared fluorescent RGD peptides for optical imaging of integrin alphavbeta3 expression in living mice. *Bioconjugate chemistry* **16**, 1433-1441.

[119] Adams KE, Ke S, Kwon S, Liang F, Fan Z, Lu Y, Hirschi K, Mawad ME, Barry MA, and Sevick-Muraca EM (2007). Comparison of visible and near-infrared wavelength-excitable fluorescent dyes for molecular imaging of cancer. *J Biomed Opt* **12**, 024017.

[120] Becker A, Hessenius C, Licha K, Ebert B, Sukowski U, Semmler W, Wiedenmann B, and Grotzinger C (2001). Receptor-targeted optical imaging of tumors with near-infrared fluorescent ligands. *Nat Biotechnol* **19**, 327-331.

[121] Ke S, Wen X, Gurfinkel M, Charnsangavej C, Wallace S, Sevick-Muraca EM, and Li C (2003). Near-infrared optical imaging of epidermal growth factor receptor in breast cancer xenografts. *Cancer research* **63**, 7870-7875.

[122] Lee SB, Hassan M, Fisher R, Chertov O, Chernomordik V, Kramer-Marek G, Gandjbakhche A, and Capala J (2008). Affibody molecules for in vivo characterization of HER2-positive tumors by near-infrared imaging. *Clin Cancer Res* **14**, 3840-3849.

[123] Wang W, Ke S, Wu Q, Charnsangavej C, Gurfinkel M, Gelovani JG, Abbruzzese JL, Sevick-Muraca EM, and Li C (2004). Near-infrared optical imaging of integrin alphavbeta3 in human tumor xenografts. *Mol Imaging* **3**, 343-351.

[124] Jin ZH, Josserand V, Foillard S, Boturyn D, Dumy P, Favrot MC, and Coll JL (2007). In vivo optical imaging of integrin alphaV-beta3 in mice using multivalent or monovalent cRGD targeting vectors. *Mol Cancer* **6**, 41.

[125] Liu Z, Liu S, Niu G, Wang F, and Chen X (2010). Optical imaging of integrin alphavbeta3 expression with near-infrared fluorescent RGD dimer with tetra(ethylene glycol) linkers. *Mol Imaging* **9**, 21-29.

[126] Moon WK, Lin Y, O'Loughlin T, Tang Y, Kim DE, Weissleder R, and Tung CH (2003). Enhanced tumor detection using a folate receptor-targeted near-infrared fluorochrome conjugate. *Bioconjugate chemistry* **14**, 539-545.

[127] Lisy MR, Goermar A, Thomas C, Pauli J, Resch-Genger U, Kaiser WA, and Hilger I (2008). In vivo near-infrared fluorescence imaging of carcinoembryonic antigen-expressing tumor cells in mice. *Radiology* **247**, 779-787.

[128] Moore A, Medarova Z, Potthast A, and Dai G (2004). In vivo targeting of underglycosylated MUC-1 tumor antigen using a multimodal imaging probe. *Cancer research* **64**, 1821-1827.

[129] Phelps M (2006) (Springer, New York), pp. 8-10.

[130] Gambhir SS, Czernin J, Schwimmer J, Silverman DH, Coleman RE, and Phelps ME (2001). A tabulated summary of the FDG PET literature. *J Nucl Med* **42**, 1S-93S.

[131] Gambhir SS (2002). Molecular imaging of cancer with positron emission tomography. *Nature reviews* **2**, 683-693.

[132] Van den Abbeele AD, and Badawi RD (2002). Use of positron emission tomography in oncology and its potential role to assess response to imatinib mesylate therapy in gastrointestinal stromal tumors (GISTs). *Eur J Cancer* **38 Suppl 5**, S60-65.

[133] Hofer C, Laubenbacher C, Block T, Breul J, Hartung R, and Schwaiger M (1999). Fluorine-18-fluorodeoxyglucose positron emission tomography is useless for the detection of local recurrence after radical prostatectomy. *Eur Urol* **36**, 31-35.

[134] Dehdashti F, Picus J, Michalski JM, Dence CS, Siegel BA, Katzenellenbogen JA, and Welch MJ (2005). Positron tomographic assessment of androgen receptors in prostatic carcinoma. *European journal of nuclear medicine and molecular imaging* **32**, 344-350.

[135] Ross JS, Sheehan CE, Fisher HA, Kaufman RP, Jr., Kaur P, Gray K, Webb I, Gray GS, Mosher R, and Kallakury BV (2003). Correlation of primary tumor prostate-specific membrane antigen expression with disease recurrence in prostate cancer. *Clin Cancer Res* **9**, 6357-6362.

[136] Evans MJ, Smith-Jones PM, Wongvipat J, Navarro V, Kim S, Bander NH, Larson SM, and Sawyers CL (2011). Noninvasive measurement of androgen receptor signaling with a positron-emitting radiopharmaceutical that targets prostate-specific membrane antigen. *Proceedings of the National Academy of Sciences of the United States of America* **108**, 9578-9582.

[137] Holland JP, Divilov V, Bander NH, Smith-Jones PM, Larson SM, and Lewis JS (2010). 89Zr-DFO-J591 for immunoPET of prostate-specific membrane antigen expression in vivo. *J Nucl Med* **51**, 1293-1300.

[138] Lepin EJ, Leyton JV, Zhou Y, Olafsen T, Salazar FB, McCabe KE, Hahm S, Marks JD, Reiter RE, and Wu AM (2010). An affinity matured minibody for PET imaging of prostate stem cell antigen (PSCA)-expressing tumors. *European journal of nuclear medicine and molecular imaging* **37**, 1529-1538.

[139] Ponde DE, Dence CS, Oyama N, Kim J, Tai YC, Laforest R, Siegel BA, and Welch MJ (2007). 18F-fluoroacetate: a potential acetate analog for prostate tumor imaging--in vivo evaluation of 18F-fluoroacetate versus 11C-acetate. *J Nucl Med* **48**, 420-428.

[140] Sutinen E, Nurmi M, Roivainen A, Varpula M, Tolvanen T, Lehikoinen P, and Minn H (2004). Kinetics of [(11)C]choline uptake in prostate

cancer: a PET study. *European journal of nuclear medicine and molecular imaging* **31**, 317-324.

[141] DeGrado TR, Baldwin SW, Wang S, Orr MD, Liao RP, Friedman HS, Reiman R, Price DT, and Coleman RE (2001). Synthesis and evaluation of (18)F-labeled choline analogs as oncologic PET tracers. *J Nucl Med* **42**, 1805-1814.

[142] Hara T, Bansal A, and DeGrado TR (2006). Effect of hypoxia on the uptake of [methyl-3H]choline, [1-14C] acetate and [18F]FDG in cultured prostate cancer cells. *Nuclear medicine and biology* **33**, 977-984.

[143] Toth G, Lengyel Z, Balkay L, Salah MA, Tron L, and Toth C (2005). Detection of prostate cancer with 11C-methionine positron emission tomography. *J Urol* **173**, 66-69; discussion 69.

[144] Schuster DM, Votaw JR, Nieh PT, Yu W, Nye JA, Master V, Bowman FD, Issa MM, and Goodman MM (2007). Initial experience with the radiotracer anti-1-amino-3-18F-fluorocyclobutane-1-carboxylic acid with PET/CT in prostate carcinoma. *J Nucl Med* **48**, 56-63.

[145] Heinlein CA, and Chang C (2004). Androgen receptor in prostate cancer. *Endocr Rev* **25**, 276-308.

[146] Larson SM, Morris M, Gunther I, Beattie B, Humm JL, Akhurst TA, Finn RD, Erdi Y, Pentlow K, Dyke J*, et al.* (2004). Tumor localization of 16beta-18F-fluoro-5alpha-dihydrotestosterone versus 18F-FDG in patients with progressive, metastatic prostate cancer. *J Nucl Med* **45**, 366-373.

[147] Honer M, Mu L, Stellfeld T, Graham K, Martic M, Fischer CR, Lehmann L, Schubiger PA, Ametamey SM, Dinkelborg L*, et al.* (2011). 18F-labeled bombesin analog for specific and effective targeting of prostate tumors expressing gastrin-releasing peptide receptors. *J Nucl Med* **52**, 270-278.

[148] Yang YS, Zhang X, Xiong Z, and Chen X (2006). Comparative in vitro and in vivo evaluation of two 64Cu-labeled bombesin analogs in a mouse model of human prostate adenocarcinoma. *Nuclear medicine and biology* **33**, 371-380.

[149] Zhang X, Cai W, Cao F, Schreibmann E, Wu Y, Wu JC, Xing L, and Chen X (2006). 18F-labeled bombesin analogs for targeting GRP receptor-expressing prostate cancer. *J Nucl Med* **47**, 492-501.

[150] Wu AM (2009). Antibodies and antimatter: the resurgence of immuno-PET. *J Nucl Med* **50**, 2-5.

[151] Holland JP, Williamson MJ, and Lewis JS (2010). Unconventional nuclides for radiopharmaceuticals. *Mol Imaging* **9**, 1-20.

[152] Koehler L, Gagnon K, McQuarrie S, and Wuest F (2010). Iodine-124: a promising positron emitter for organic PET chemistry. *Molecules* **15**, 2686-2718.

[153] Belov VV, Bonab AA, Fischman AJ, Heartlein M, Calias P, and Papisov MI (2011). Iodine-124 as a Label for Pharmacological PET Imaging. *Mol Pharm* **8**, 736-747.

[154] Tuszynski GP, Knight LC, Kornecki E, and Srivastava S (1983). Labeling of platelet surface proteins with 125I by the iodogen method. *Anal Biochem* **130**, 166-170.

[155] Gonyea-Stewart L (1981). Iodination of antiferritin by the method of Bolton and Hunter. *Clin Chem* **27**, 643.

[156] Robinson MK, Doss M, Shaller C, Narayanan D, Marks JD, Adler LP, Gonzalez Trotter DE, and Adams GP (2005). Quantitative immuno-positron emission tomography imaging of HER2-positive tumor xenografts with an iodine-124 labeled anti-HER2 diabody. *Cancer research* **65**, 1471-1478.

[157] Collingridge DR, Carroll VA, Glaser M, Aboagye EO, Osman S, Hutchinson OC, Barthel H, Luthra SK, Brady F, Bicknell R*, et al.* (2002). The development of [(124)I]iodinated-VG76e: a novel tracer for imaging vascular endothelial growth factor in vivo using positron emission tomography. *Cancer research* **62**, 5912-5919.

[158] Bakir MA, Eccles S, Babich JW, Aftab N, Styles J, Dean CJ, Lambrecht RM, and Ott RJ (1992). c-erbB2 protein overexpression in breast cancer as a target for PET using iodine-124-labeled monoclonal antibodies. *J Nucl Med* **33**, 2154-2160.

[159] Sundaresan G, Yazaki PJ, Shively JE, Finn RD, Larson SM, Raubitschek AA, Williams LE, Chatziioannou AF, Gambhir SS, and Wu AM (2003). 124I-labeled engineered anti-CEA minibodies and diabodies allow high-contrast, antigen-specific small-animal PET imaging of xenografts in athymic mice. *J Nucl Med* **44**, 1962-1969.

[160] Orlova A, Wallberg H, Stone-Elander S, and Tolmachev V (2009). On the selection of a tracer for PET imaging of HER2-expressing tumors: direct comparison of a 124I-labeled affibody molecule and trastuzumab in a murine xenograft model. *J Nucl Med* **50**, 417-425.

[161] Chaturvedi R, Heimburg J, Yan J, Koury S, Sajjad M, Abdel-Nabi HH, and Rittenhouse-Olson K (2008). Tumor immunolocalization using 124 I-iodine-labeled JAA-F11 antibody to Thomsen-Friedenreich alpha-linked antigen. *Appl Radiat Isot* **66**, 278-287.

[162] Tijink BM, Perk LR, Budde M, Stigter-van Walsum M, Visser GW, Kloet RW, Dinkelborg LM, Leemans CR, Neri D, and van Dongen GA (2009). (124)I-L19-SIP for immuno-PET imaging of tumour vasculature and guidance of (131)I-L19-SIP radioimmunotherapy. *European journal of nuclear medicine and molecular imaging* **36**, 1235-1244.

[163] Divgi CR, Pandit-Taskar N, Jungbluth AA, Reuter VE, Gonen M, Ruan S, Pierre C, Nagel A, Pryma DA, Humm J*, et al.* (2007). Preoperative characterisation of clear-cell renal carcinoma using iodine-124-labelled antibody chimeric G250 (124I-cG250) and PET in patients with renal masses: a phase I trial. *Lancet Oncol* **8**, 304-310.

[164] Pentlow KS, Graham MC, Lambrecht RM, Daghighian F, Bacharach SL, Bendriem B, Finn RD, Jordan K, Kalaigian H, Karp JS*, et al.* (1996). Quantitative imaging of iodine-124 with PET. *J Nucl Med* **37**, 1557-1562.

[165] Weissleder R, and Pittet MJ (2008). Imaging in the era of molecular oncology. *Nature* **452**, 580-589.

[166] Blasberg RG (2007). Imaging update: new windows, new views. *Clin Cancer Res* **13**, 3444-3448.

[167] Bombeli T, Karsan A, Tait JF, and Harlan JM (1997). Apoptotic vascular endothelial cells become procoagulant. *Blood* **89**, 2429-2442.

[168] Boyle EM, Jr., Pohlman TH, Cornejo CJ, and Verrier ED (1996). Endothelial cell injury in cardiovascular surgery: ischemia-reperfusion. *Ann Thorac Surg* **62**, 1868-1875.

[169] Tait JF (2008). Imaging of apoptosis. *J Nucl Med* **49**, 1573-1576.

[170] Blankenberg FG (2008). In vivo detection of apoptosis. *J Nucl Med* **49 Suppl 2**, 81S-95S.

[171] Ran S, and Thorpe PE (2002). Phosphatidylserine is a marker of tumor vasculature and a potential target for cancer imaging and therapy. *Int J Radiat Oncol Biol Phys* **54**, 1479-1484.

[172] Thorpe PE Targeting anionic phospholipids on tumor blood vessels and tumor cells. *Thromb Res* **125 Suppl 2**, S134-137.

[173] Tomillero A, and Moral MA (2009). Gateways to clinical trials. *Methods Find Exp Clin Pharmacol* **31**, 661-700.

[174] Hsu AR, Cai W, Veeravagu A, Mohamedali KA, Chen K, Kim S, Vogel H, Hou LC, Tse V, Rosenblum MG*, et al.* (2007). Multimodality molecular imaging of glioblastoma growth inhibition with vasculature-targeting fusion toxin VEGF121/rGel. *J Nucl Med* **48**, 445-454.

[175] Zhou H, Luby-Phelps K, Mickey BE, Habib AA, Mason RP, and Zhao D (2009). Dynamic near-infrared optical imaging of 2-deoxyglucose uptake by intracranial glioma of athymic mice. *PLoS One* **4**, e8051.

[176] McCann CM, Waterman P, Figueiredo JL, Aikawa E, Weissleder R, and Chen JW (2009). Combined magnetic resonance and fluorescence imaging of the living mouse brain reveals glioma response to chemotherapy. *Neuroimage* **45**, 360-369.

[177] Rehemtulla A, Stegman LD, Cardozo SJ, Gupta S, Hall DE, Contag CH, and Ross BD (2000). Rapid and quantitative assessment of cancer

treatment response using in vivo bioluminescence imaging. *Neoplasia* **2**, 491-495.

[178] Ke S, Wen X, Wu QP, Wallace S, Charnsangavej C, Stachowiak AM, Stephens CL, Abbruzzese JL, Podoloff DA, and Li C (2004). Imaging taxane-induced tumor apoptosis using PEGylated, 111In-labeled annexin V. *J Nucl Med* **45**, 108-115.

[179] Kim YE, Chen J, Chan JR, and Langen R Engineering a polarity-sensitive biosensor for time-lapse imaging of apoptotic processes and degeneration. *Nat Methods* **7**, 67-73.

[180] Rottey S, Slegers G, Van Belle S, Goethals I, and Van de Wiele C (2006). Sequential 99mTc-hydrazinonicotinamide-annexin V imaging for predicting response to chemotherapy. *J Nucl Med* **47**, 1813-1818.

[181] Hammill AK, Uhr JW, and Scheuermann RH (1999). Annexin V staining due to loss of membrane asymmetry can be reversible and precede commitment to apoptotic death. *Exp Cell Res* **251**, 16-21.

[182] Andree HA, Reutelingsperger CP, Hauptmann R, Hemker HC, Hermens WT, and Willems GM (1990). Binding of vascular anticoagulant alpha (VAC alpha) to planar phospholipid bilayers. *J Biol Chem* **265**, 4923-4928.

[183] Schlaepfer DD, Mehlman T, Burgess WH, and Haigler HT (1987). Structural and functional characterization of endonexin II, a calcium- and phospholipid-binding protein. *Proc Natl Acad Sci U S A* **84**, 6078-6082.

[184] Giepmans BN, Adams SR, Ellisman MH, and Tsien RY (2006). The fluorescent toolbox for assessing protein location and function. *Science* **312**, 217-224.

[185] Hoffman RM (2005). The multiple uses of fluorescent proteins to visualize cancer in vivo. *Nat Rev Cancer* **5**, 796-806.

[186] Hama Y, Urano Y, Koyama Y, Choyke PL, and Kobayashi H (2007). Activatable fluorescent molecular imaging of peritoneal metastases following pretargeting with a biotinylated monoclonal antibody. *Cancer Res* **67**, 3809-3817.

[187] Stummer W, Pichlmeier U, Meinel T, Wiestler OD, Zanella F, and Reulen HJ (2006). Fluorescence-guided surgery with 5-aminolevulinic acid for resection of malignant glioma: a randomised controlled multicentre phase III trial. *Lancet Oncol* **7**, 392-401.

[188] Sevick-Muraca EM, Sharma R, Rasmussen JC, Marshall MV, Wendt JA, Pham HQ, Bonefas E, Houston JP, Sampath L, Adams KE*, et al.* (2008). Imaging of lymph flow in breast cancer patients after microdose administration of a near-infrared fluorophore: feasibility study. *Radiology* **246**, 734-741.

[189] Williamson P, and Schlegel RA (1994). Back and forth: the regulation and function of transbilayer phospholipid movement in eukaryotic cells. *Molecular membrane biology* **11**, 199-216.

[190] Fadok VA, Voelker DR, Campbell PA, Cohen JJ, Bratton DL, and Henson PM (1992). Exposure of phosphatidylserine on the surface of apoptotic lymphocytes triggers specific recognition and removal by macrophages. *J Immunol* **148**, 2207-2216.

[191] Fadok VA, Bratton DL, and Henson PM (2001). Phagocyte receptors for apoptotic cells: recognition, uptake, and consequences. *J Clin Invest* **108**, 957-962.

[192] Hannun YA, Luberto C, and Argraves KM (2001). Enzymes of sphingolipid metabolism: from modular to integrative signaling. *Biochemistry* **40**, 4893-4903.

[193] Bauwens M, De Saint-Hubert M, Devos E, Deckers N, Reutelingsperger C, Mortelmans L, Himmelreich U, Mottaghy FM, and Verbruggen A (2011). Site-specific (68)Ga-labeled Annexin A5 as a PET imaging agent for apoptosis. *Nuclear medicine and biology* **38**, 381-392.

[194] Loose D, Vermeersch H, De Vos F, Deron P, Slegers G, and Van de Wiele C (2008). Prognostic value of 99mTc-HYNIC annexin-V imaging in squamous cell carcinoma of the head and neck. *European journal of nuclear medicine and molecular imaging* **35**, 47-52.

[195] Reddy S, and Robinson MK (2010). Immuno-positron emission tomography in cancer models. *Semin Nucl Med* **40**, 182-189.

[196] Hoebers FJ, Kartachova M, de Bois J, van den Brekel MW, van Tinteren H, van Herk M, Rasch CR, Valdes Olmos RA, and Verheij M (2008). 99mTc Hynic-rh-Annexin V scintigraphy for in vivo imaging of apoptosis in patients with head and neck cancer treated with chemoradiotherapy. *European journal of nuclear medicine and molecular imaging* **35**, 509-518.

[197] Dekker B, Keen H, Shaw D, Disley L, Hastings D, Hadfield J, Reader A, Allan D, Julyan P, Watson A*, et al.* (2005). Functional comparison of annexin V analogues labeled indirectly and directly with iodine-124. *Nuclear medicine and biology* **32**, 403-413.

[198] Galli M, Comfurius P, Maassen C, Hemker HC, de Baets MH, van Breda-Vriesman PJ, Barbui T, Zwaal RF, and Bevers EM (1990). Anticardiolipin antibodies (ACA) directed not to cardiolipin but to a plasma protein cofactor. *Lancet* **335**, 1544-1547.

[199] McNeil HP, Simpson RJ, Chesterman CN, and Krilis SA (1990). Anti-phospholipid antibodies are directed against a complex antigen that includes a lipid-binding inhibitor of coagulation: beta 2-glycoprotein I

(apolipoprotein H). *Proceedings of the National Academy of Sciences of the United States of America* **87**, 4120-4124.

[200] Matsuura E, Igarashi Y, Fujimoto M, Ichikawa K, and Koike T (1990). Anticardiolipin cofactor(s) and differential diagnosis of autoimmune disease. *Lancet* **336**, 177-178.

[201] Anjos DA, Etchebehere EC, Ramos CD, Santos AO, Albertotti C, and Camargo EE (2007). 18F-FDG PET/CT delayed images after diuretic for restaging invasive bladder cancer. *J Nucl Med* **48**, 764-770.

[202] Kamel EM, Jichlinski P, Prior JO, Meuwly JY, Delaloye JF, Vaucher L, Malterre J, Castaldo S, Leisinger HJ, and Delaloye AB (2006). Forced diuresis improves the diagnostic accuracy of 18F-FDG PET in abdominopelvic malignancies. *J Nucl Med* **47**, 1803-1807.

[203] Carrasquillo JA, Pandit-Taskar N, O'Donoghue JA, Humm JL, Zanzonico P, Smith-Jones PM, Divgi CR, Pryma DA, Ruan S, Kemeny NE*, et al.* (2011). (124)I-huA33 antibody PET of colorectal cancer. *J Nucl Med* **52**, 1173-1180.

[204] Zhou Q, Zhao J, Stout JG, Luhm RA, Wiedmer T, and Sims PJ (1997). Molecular cloning of human plasma membrane phospholipid scramblase. A protein mediating transbilayer movement of plasma membrane phospholipids. *The Journal of biological chemistry* **272**, 18240-18244.

[205] Soares FA, Shaughnessy SG, MacLarkey WR, and Orr FW (1994). Quantification and morphologic demonstration of reactive oxygen species produced by Walker 256 tumor cells in vitro and during metastasis in vivo. *Laboratory investigation; a journal of technical methods and pathology* **71**, 480-489.

[206] Shaughnessy SG, Buchanan MR, Turple S, Richardson M, and Orr FW (1989). Walker carcinosarcoma cells damage endothelial cells by the generation of reactive oxygen species. *The American journal of pathology* **134**, 787-796.

[207] Hayashi F, Nagashima K, Terui Y, Kawamura Y, Matsumoto K, and Itazaki H (1990). The structure of PA48009: the revised structure of duramycin. *The Journal of antibiotics* **43**, 1421-1430.

[208] Hagenbuch B (2010). Drug uptake systems in liver and kidney: a historic perspective. *Clin Pharmacol Ther* **87**, 39-47.

[209] van Montfoort JE, Hagenbuch B, Groothuis GM, Koepsell H, Meier PJ, and Meijer DK (2003). Drug uptake systems in liver and kidney. *Curr Drug Metab* **4**, 185-211.

[210] Hockel M, and Vaupel P (2001). Tumor hypoxia: definitions and current clinical, biologic, and molecular aspects. *J Natl Cancer Inst* **93**, 266-276.

[211] Vaupel P, Mayer A, and Hockel M (2004). Tumor hypoxia and malignant progression. *Methods Enzymol* **381**, 335-354.

[212] Choung SY, Kobayashi T, Takemoto K, Ishitsuka H, and Inoue K (1988). Interaction of a cyclic peptide, Ro09-0198, with phosphatidylethanolamine in liposomal membranes. *Biochimica et biophysica acta* **940**, 180-187.

[213] Emoto K, Kobayashi T, Yamaji A, Aizawa H, Yahara I, Inoue K, and Umeda M (1996). Redistribution of phosphatidylethanolamine at the cleavage furrow of dividing cells during cytokinesis. *Proceedings of the National Academy of Sciences of the United States of America* **93**, 12867-12872.

[214] Li Z, Wells CW, Esmon CT, and Zhao M (2009). Phosphatidylethanolamine at the endothelial surface of aortic flow dividers. *J Thromb Haemost* **7**, 227-229.

[215] Fantone JC, and Ward PA (1982). Role of oxygen-derived free radicals and metabolites in leukocyte-dependent inflammatory reactions. *Am J Pathol* **107**, 395-418.

[216] Zachowski A, Favre E, Cribier S, Herve P, and Devaux PF (1986). Outside-inside translocation of aminophospholipids in the human erythrocyte membrane is mediated by a specific enzyme. *Biochemistry* **25**, 2585-2590.

[217] Sokolove PM, Westphal PA, Kester MB, Wierwille R, and Sikora-VanMeter K (1989). Duramycin effects on the structure and function of heart mitochondria. I. Structural alterations and changes in membrane permeability. *Biochimica et biophysica acta* **983**, 15-22.

[218] Makino A, Baba T, Fujimoto K, Iwamoto K, Yano Y, Terada N, Ohno S, Sato SB, Ohta A, Umeda M*, et al.* (2003). Cinnamycin (Ro 09-0198) promotes cell binding and toxicity by inducing transbilayer lipid movement. *The Journal of biological chemistry* **278**, 3204-3209.

[219] Boswell CA, Sun X, Niu W, Weisman GR, Wong EH, Rheingold AL, and Anderson CJ (2004). Comparative in vivo stability of copper-64-labeled cross-bridged and conventional tetraazamacrocyclic complexes. *J Med Chem* **47**, 1465-1474.

[220] Nahrendorf M, Keliher E, Marinelli B, Waterman P, Feruglio PF, Fexon L, Pivovarov M, Swirski FK, Pittet MJ, Vinegoni C*, et al.* (2010). Hybrid PET-optical imaging using targeted probes. *Proceedings of the National Academy of Sciences of the United States of America* **107**, 7910-7915.

[221] Aide N, Cappele O, Bottet P, Bensadoun H, Regeasse A, Comoz F, Sobrio F, Bouvard G, and Agostini D (2003). Efficiency of [(18)F]FDG PET in characterising renal cancer and detecting distant metastases: a

comparison with CT. *European journal of nuclear medicine and molecular imaging* **30**, 1236-1245.

[222] Sacco E, Pinto F, Totaro A, D'Addessi A, Racioppi M, Gulino G, Volpe A, Marangi F, D'Agostino D, and Bassi P (2011). Imaging of renal cell carcinoma: state of the art and recent advances. *Urol Int* **86**, 125-139.

[223] Sprague JE, Peng Y, Sun X, Weisman GR, Wong EH, Achilefu S, and Anderson CJ (2004). Preparation and biological evaluation of copper-64-labeled tyr3-octreotate using a cross-bridged macrocyclic chelator. *Clin Cancer Res* **10**, 8674-8682.

[224] Smith CJ, Volkert WA, and Hoffman TJ (2005). Radiolabeled peptide conjugates for targeting of the bombesin receptor superfamily subtypes. *Nuclear medicine and biology* **32**, 733-740.

[225] Hilgenbrink AR, and Low PS (2005). Folate receptor-mediated drug targeting: from therapeutics to diagnostics. *J Pharm Sci* **94**, 2135-2146.

[226] Teunissen JJ, Kwekkeboom DJ, and Krenning EP (2006). Staging and treatment of differentiated thyroid carcinoma with radiolabeled somatostatin analogs. *Trends Endocrinol Metab* **17**, 19-25.

[227] Linden HM, Kurland BF, Peterson LM, Schubert EK, Gralow JR, Specht JM, Ellis GK, Lawton TJ, Livingston RB, Petra PH*, et al.* (2011). Fluoroestradiol positron emission tomography reveals differences in pharmacodynamics of aromatase inhibitors, tamoxifen, and fulvestrant in patients with metastatic breast cancer. *Clin Cancer Res* **17**, 4799-4805.

[228] Van Den Bossche B, and Van de Wiele C (2004). Receptor imaging in oncology by means of nuclear medicine: current status. *J Clin Oncol* **22**, 3593-3607.

[229] Sipkins DA, Cheresh DA, Kazemi MR, Nevin LM, Bednarski MD, and Li KC (1998). Detection of tumor angiogenesis in vivo by alphaVbeta3-targeted magnetic resonance imaging. *Nat Med* **4**, 623-626.

[230] Neves AA, and Brindle KM (2006). Assessing responses to cancer therapy using molecular imaging. *Biochimica et biophysica acta* **1766**, 242-261.

[231] Paez JG, Janne PA, Lee JC, Tracy S, Greulich H, Gabriel S, Herman P, Kaye FJ, Lindeman N, Boggon TJ*, et al.* (2004). EGFR mutations in lung cancer: correlation with clinical response to gefitinib therapy. *Science* **304**, 1497-1500.

[232] West CM, Jones T, and Price P (2004). The potential of positron-emission tomography to study anticancer-drug resistance. *Nature reviews* **4**, 457-469.

[233] Burrows FJ, Watanabe Y, and Thorpe PE (1992). A murine model for antibody-directed targeting of vascular endothelial cells in solid tumors. *Cancer Res* **52**, 5954-5962.

[234] Price JE (1996). Metastasis from human breast cancer cell lines. *Breast Cancer Res Treat* **39**, 93-102.

[235] Guy CT, Cardiff RD, and Muller WJ (1992). Induction of mammary tumors by expression of polyomavirus middle T oncogene: a transgenic mouse model for metastatic disease. *Mol Cell Biol* **12**, 954-961.